



ALMA MATER STUDIORUM  
UNIVERSITÀ DI BOLOGNA

in cotutela con **Aix-Marseille Université**

DOTTORATO DI RICERCA IN  
  
BIOTECHNOLOGICAL, BIOCOMPUTATIONAL,  
PHARMACEUTICAL AND PHARMACOLOGICAL  
SCIENCES

Ciclo XXVI

Settore Concorsuale: 05/E3

Settore Scientifico Disciplinare: BIO12

BONE BIOMINERALIZATION IN OSTEOSARCOMA: A MULTIMODAL  
MULTISCALE IN/EX VIVO STUDY THROUGH SYNCHROTRON-  
BASED X-RAY AND NMR TECHNIQUES

**Presentata da: *Francesca Rossi***

**Coordinatore Dottorato**

**Prof.ssa Maria Laura Bolognesi**

**Supervisore**

**Prof. Emil Malucelli**

**David Bendahan**

Esame finale anno 2023



*“D’où que l’on vienne, on est chez soi à Marseille.*

*Dans le rues, on croise des visages familiers,  
des odeurs familières. Marseille est familière.*

*Dès le premier regard”*

Jean-Claude Izzo



# Abstract – en

Osteosarcoma (OS) is a rare and aggressive bone tumor mainly affecting adolescents and young adults. Recent studies suggested that dysfunctions in osteogenic differentiation may contribute to OS genesis and development, leading to a malignant environment that promotes cancer growth and migration. OS clinical diagnosis involves investigating persistent bone pain, swelling, and fractures through radiological imaging and biopsy. In addition, treatment typically involves a multimodal approach combining surgical resection of the tumor and chemotherapy before and after surgery. This thesis aims to provide new insights into osteosarcoma through a comprehensive multiscale characterization of the tumor, exploiting advanced synchrotron-based X-ray and magnetic resonance techniques.

SaOS-2 cells were induced to differentiate into osteoblasts and were studied during the early stages of biomineralization. Mineral matrix formation was monitored exploiting synchrotron-based X-ray techniques, suggesting a mechanism based on the interaction between mitochondria and vesicles.

OS is characterized by uncontrolled cells proliferation and consequent generation of an abnormal tissue microenvironment that promotes tumor growth and metastasis. Therefore, an extensive structural and morphological characterization of osteosarcoma tissue holds great potential for identifying new targets and therapeutic strategies. Synchrotron-based X-ray techniques were utilized to analyze resected human osteosarcoma tissues, revealing differences in morphology, mineral, and chemical composition compared to normal bone.

Currently, invasive biopsy remains the gold standard for identifying bone sarcomas and monitoring their pathological progression. Nuclear magnetic resonance (NMR) techniques at ultra-high field, particularly diffusion-weighted imaging and

magnetic resonance spectroscopy, showed promise in characterizing bone sarcomas cellularity and metabolism.

In conclusion, thanks to the combination of synchrotron-based and NMR techniques, this work tackles the challenge to bridge the gap between cellular and clinical aspects of osteosarcoma. Moreover, the multimodal approach provides new insights into bone sarcomas, paving the way for the development of improved therapeutic strategies and more precise diagnostic tools.

# Abstract – fr

L'ostéosarcome (OS) est une tumeur osseuse rare et agressive qui affecte principalement les adolescents et les jeunes adultes. Des études récentes ont suggéré que des dysfonctionnements dans la différenciation ostéogénique pourraient contribuer à la genèse et au développement de l'OS, conduisant à un environnement malin qui favoriserait la croissance et la migration du cancer. Le diagnostic clinique de l'OS repose sur l'investigation de douleurs osseuses persistantes, de gonflements et de fractures sur la base d'investigations radiologiques et de biopsies. De plus, le traitement implique généralement une approche multimodale combinant la résection chirurgicale de la tumeur et la chimiothérapie avant et après la chirurgie. Cette thèse vise à fournir de nouvelles perspectives sur l'ostéosarcome grâce à une caractérisation multi-échelle complète de la tumeur, en exploitant des techniques avancées de rayons X de synchrotron et de résonance magnétique.

Les cellules SaOS-2 ont été induites en vue d'une différenciation en ostéoblastes et ont été étudiées au cours des premiers stades de la biominéralisation. La formation de la matrice minérale a été suivie grâce aux techniques de rayons X de synchrotron et a suggéré l'existence d'un mécanisme basé sur l'interaction entre mitochondries et vésicules.

L'OS est caractérisé par une prolifération cellulaire non contrôlée et par la génération d'un microenvironnement anormal qui favorise la croissance tumorale et les métastases. Par conséquent, une caractérisation structurale et morphologique extensive des tissus de l'ostéosarcome offre un grand potentiel pour identifier de nouvelles stratégies thérapeutiques. Des techniques de rayons X de synchrotron ont été utilisées pour analyser les tissus d'ostéosarcome humain réséqués et ont révélé

des différences de morphologie, de composition minérale et chimique par rapport à l'os normal.

Actuellement, la biopsie invasive reste la norme de référence pour identifier les sarcomes osseux et surveiller leur progression pathologique. Les techniques de résonance magnétique nucléaire (RMN) à ultra-haut champ, en particulier l'imagerie de diffusion et la spectroscopie par résonance magnétique, se sont révélées prometteuses pour caractériser la cellularité et le métabolisme des sarcomes osseux.

En conclusion, grâce à la combinaison des techniques de rayons X de synchrotron et de RMN, ce travail a relevé le défi de combler le fossé entre les aspects cellulaires et cliniques de l'ostéosarcome. De plus, l'approche multimodale offre de nouvelles perspectives sur les sarcomes osseux, ouvrant la voie au développement de meilleures stratégies thérapeutiques et d'outils de diagnostic plus précis.



# Abstract – it

L'osteosarcoma (OS) è un tumore osseo raro e aggressivo che si presenta prevalentemente in età adolescenziale. Studi recenti hanno suggerito che alterazioni del differenziamento osteoblastico possono contribuire alla genesi e allo sviluppo dell'OS, producendo un ambiente maligno che favorisce la crescita e la migrazione del tumore. Da un punto di vista clinico, sintomi quali dolore osseo persistente, gonfiore e fratture vengono studiati combinando imaging radiologico e biopsia. L'OS viene trattato lizzando un approccio multimodale basato sulla resezione chirurgica e sulla chemioterapia somministrata prima e dopo l'intervento. Questa tesi si pone l'obiettivo di fornire nuove conoscenze sull'osteosarcoma attraverso una caratterizzazione completa e multiscala del tumore, sfruttando tecniche avanzate a raggi X di sincrotrone e di risonanza magnetica.

La linea cellulare SaOS-2 è stata indotta al differenziamento osteoblastico ed è stata studiata durante le prime fasi del processo di biomineralizzazione. La formazione della matrice minerale è stata monitorata con tecniche a raggi X di sincrotrone, evidenziando un meccanismo basato sull'interazione tra mitocondri e vescicole.

L'OS è caratterizzato da una proliferazione cellulare incontrollata e dalla conseguente generazione di un microambiente anomalo che favorisce la crescita del tumore e le metastasi. Di conseguenza, un'approfondita analisi strutturale e morfologica dei tessuti dell'osteosarcoma possiede un grande potenziale per l'identificazione di nuove strategie terapeutiche. Le tecniche a raggi X di sincrotrone sono state utilizzate per esaminare tessuti di osteosarcoma estratti da pazienti, rivelando differenze nella morfologia e nella composizione minerale e chimica rispetto all'osso normale.

Attualmente, la biopsia è l'esame diagnostico di riferimento per identificare i sarcomi ossei e seguire le loro alterazioni patologiche nel tempo. Le tecniche di risonanza magnetica nucleare (NMR) ad ultra-alto campo, in particolare l'imaging di diffusione e la spettroscopia di risonanza magnetica, hanno dimostrato un grande potenziale nel caratterizzare la cellularità e il metabolismo delle lesioni tumorali.

In conclusione, questo lavoro di tesi ha affrontato la sfida di ridurre il divario tra gli aspetti cellulari e clinici dell'osteosarcoma, grazie alla combinazione di tecniche di sincrotrone e NMR. Inoltre, l'approccio multimodale adottato fornisce nuove conoscenze sui sarcomi dell'osso, aprendo la strada al miglioramento delle terapie e allo sviluppo di strumenti diagnostici più precisi.

# Contents

Chapter 1: Introduction.....	1
1.1 Bone tissue.....	1
1.1.1 Bone cells, bone remodeling and regulation .....	2
1.1.2 Bone mineral matrix.....	4
1.2 Osteogenic differentiation.....	8
1.3 Bone mineralization .....	9
1.4 Bone sarcomas .....	11
1.5 Osteoblasts cell model in vitro research .....	14
1.5.1 Characteristics of SaOS-2 cell line .....	15
1.5.2 Calcium depositions genesis in SaOS-2 cells .....	16
1.6 Synchrotron-based techniques.....	17
1.6.1 X-ray Absorption Spectroscopy (XAS) .....	19
1.6.1.1 X-ray Fluorescence Microscopy (XRFM) .....	21
1.6.1.2 X-ray Absorption Fine-Structure Spectroscopy (XAFS).....	23
1.6.2 Synchrotron radiation-based imaging .....	29
1.6.2.1 Soft X-ray microscopy and cryo-Soft X-ray Tomography (cryo-SXT) .....	29
1.6.2.2 Phase-Contrast micro-Tomography (PhC micro-T).....	31
1.6.3 X-ray Diffraction (XRD) .....	34
1.7 Nuclear Magnetic Resonance .....	40
1.7.1 Principles of Nuclear Magnetic Resonance.....	40
1.7.1.1 Magnetic Resonance Imaging (MRI).....	42
1.7.1.2 Magnetic Resonance Spectroscopy (MRS) .....	43
1.7.1.3 Ultra-High Field nuclear magnetic resonance (UHF NMR) .....	44
1.7.2 Imaging of bone sarcoma .....	46
1.7.2.1 Proton Density (PD) and Proton Density Fat-Saturation (PDFS).....	48

1.7.2.2 Diffusion-Weighted Imaging (DWI) .....	50
1.7.2.3 Proton Magnetic Resonance Spectroscopy ( $^1\text{H}$ -MRS) .....	52
1.8 Aim of the work .....	55
Chapter 2: Biomineralization in Osteosarcoma cells .....	57
2.1 Materials and Methods.....	58
2.1.1 SaOS-2 cells culture and osteogenic induction.....	58
2.1.2 Alizarin Red staining .....	58
2.1.3 Alkaline Phosphatase activity assay.....	58
2.1.4 Gene expression analysis .....	59
2.1.5 X-ray absorption near-edge spectro-microscopy (XANES) and cryo-Soft X-ray tomography (cro-SXT) .....	60
2.1.6 Principal Components Analysis (PCA) on nano-XANES Ca <b>L3,2</b> –edge spectra 64	
2.1.7 Nano X-ray Fluorescence Microscopy (nano-XRFM).....	65
2.1.8 Micro X-rays Fluorescence Microscopy (micro-XRFM) and micro- XANES.	67
2.2 Results.....	68
2.2.1 Gene Expression Analysis and Functional Characterization of SaOS-2 Cells after Osteogenic Induction.....	68
2.2.2 Synchrotron-radiation X-ray techniques for SaOS-2 cells characterization....	69
2.2.2.1 4 days control .....	69
2.2.2.2 4 days treated.....	72
2.2.2.3 10 days control .....	75
2.2.2.4 10 days treated.....	78
2.2.2.5 PCA analysis on micro-XANES Ca-K edge spectra .....	81
2.3 Discussion and Future Perspectives.....	84
Chapter 3: Characterization of Osteosarcoma human tissue.....	91
3.1 Materials and Methods.....	93
3.1.1 Bone samples .....	93

3.1.2	Phase-Contrast micro-Tomography (PhC micro-T).....	93
3.1.3	X-ray Diffraction (XRD) .....	98
3.1.4	Micro X-ray Fluorescence Microscopy (micro-XRFM) and micro-X-ray Absorption Near Edge Spectroscopy (micro-XANES) .....	100
3.2	Results .....	101
3.2.1	Phase-Contrast micro-Tomography (PhC micro-T).....	101
3.2.2	X-ray Diffraction and micro-X-ray Absorption Near Edge Spectroscopy (micro-XANES).....	108
3.2.3	PCA analysis on micro-XANES Ca K-edge spectra s .....	119
3.3	Discussion and Future Perspectives .....	122
Chapter 4:	Multiparametric evaluation of bone sarcomas .....	127
4.1	Patients and Methods .....	128
4.1.1	Patients .....	128
4.1.2	Protocol .....	128
4.1.3	Diffusion-Weighted Imaging (DWI) .....	130
4.1.4	<sup>1</sup> H-Magnetic Resonance Spectroscopy ( <sup>1</sup> H-MRS).....	130
4.2	Results .....	131
4.2.1	Subject 0.....	131
4.2.2	Subject 1.....	134
4.2.3	Subject 2.....	135
4.2.4	Subject 3.....	136
4.2.5	Subject 4.....	137
4.3	Discussion and Future Perspectives .....	138
Chapter 5:	Conclusions.....	143
References.....		147

Acknowledgements.....165

# List of abbreviations

HA	hydroxyapatite
PTH	parathyroid hormone
ALP	alkaline phosphatase
BSP	bone sialoproteins
OPN	osteopontin
SPARC	osteonectin
OCN	osteocalcin
OS	osteosarcoma
MSC	mesenchymal stem cell
UPS	undifferentiated pleomorphic sarcoma
MRI	magnetic resonance imaging
EDX	energy dispersive X-ray analysis
CA	carbonic anhydrase
bMSC	bone mesenchymal stem cell
XAS	X-ray absorption spectroscopy
XRF	X-ray fluorescence
XAFS	X-ray absorption fine structure
XANES	X-ray absorption near-edge spectroscopy
EXAFS	extended X-ray absorption spectroscopy
SXT	Soft-X-ray tomography
FOV	field of view
PhC	micro-T phase-contrast micro-tomography
PBI	projection-based imaging

FBP filtered back-projection  
XRD X-ray diffraction  
NMR nuclear magnetic resonance  
PD proton density  
PDFS proton density fat-saturated  
MRS magnetic resonance spectroscopy  
FT Fourier transform  
UHF ultra-high field  
FDA food and drug administration  
SNR signal-to-noise ratio  
CNR contrast-to-noise ratio  
QSM quantitative susceptibility mapping  
RF radiofrequency  
CT computed tomography  
PET positron emission tomography  
MSK musculoskeletal  
DWI diffusion-weighted imaging  
ADC apparent diffusion coefficient  
MD mean diffusivity  
Cho choline  
Cr creatine  
FBS fetal bovine serum  
qPCR quantitative real-time PCR  
PCA principal component analysis  
ROI region of interest  
POI point of interest



ACC amorphous calcium carbonate

OXPPOS oxidative phosphorylation

TME tumor micro-environment

FWHM full-width at half maximum

DXA dual-energy X-ray absorptiometry

SAXS Small-Angle X-ray Scattering

WAXS Wide-Angle X-ray Scattering



# Chapter 1: Introduction

This thesis work is organized as follows: Chapter 1, lays the foundation for the entire study, offering a comprehensive overview of bone tissue, bone cells, bone sarcomas, and the application of innovative techniques in bone research. Synchrotron-based and nuclear magnetic resonance techniques are presented, emphasizing their principles with a focus on their potentialities in providing new knowledge on bone tissue. Chapter 2 delves into the experiments carried out on osteosarcoma cell cultures. Methodologies, experimental setups, and key observations are detailed to give a comprehensive understanding of the cellular mechanisms involved in biomineralization. Chapter 3 is devoted to the characterization of resected osteosarcoma tissues. Synchrotron-based techniques were exploited to provide new insights on the structural and molecular features of osteosarcoma ranging from the macroscopic to the nanoscopic level. Chapter 4 shifts the focus to the application of nuclear magnetic resonance techniques in the study of bone sarcomas *in vivo*. The methods employed and developed, the parameters measured, and the initial interpretations drawn from the acquired data are described. Chapter 5 consolidates the key findings of the research to make them accessible and valuable for the scientific community. Finally, potential impacts on clinical applications, experimental avenues for future research, and the implications of a multidisciplinary study in the field of bone oncology are disclosed.

## 1.1 Bone tissue

Healthy bone can be regarded as a hierarchically structured material with distinct morphological variations across different length scales [1] (Fig. 1.1). From a macroscopical

perspective, it is possible to differentiate between cortical (about 80%) and cancellous bone (20%) [2]. The cortical (compact) bone constitutes the outer shell of each bone and is formed by osteons, cylindrical units where lamellar structures encircle Haversian canals (200–250  $\mu\text{m}$  in diameter). The compact bone is enveloped externally by the periosteum and internally by endosteum. On the other hand, the cancellous (trabecular) bone consists of a network of trabeculae surrounded by connective tissue and bone marrow. The bone marrow, a hematopoietic organ, fills the space between trabeculae and contains pluripotent stem cells and mesenchymal stem cells that can differentiate into osteoblasts [3]. At the microscopic scale, lamellae are made of collagen fibers with mineral intercalations (3–7  $\mu\text{m}$  wide) [2]. Zooming further to the nanometer level, collagen fibers are composed of collagen molecules arranged in a staggered pattern with a periodicity ranging from 35 to 60 nm. Mineral particles, made of hydroxyapatite crystals, can be found within collagen gap zones and outside of the fibrils [1], [4], [5].

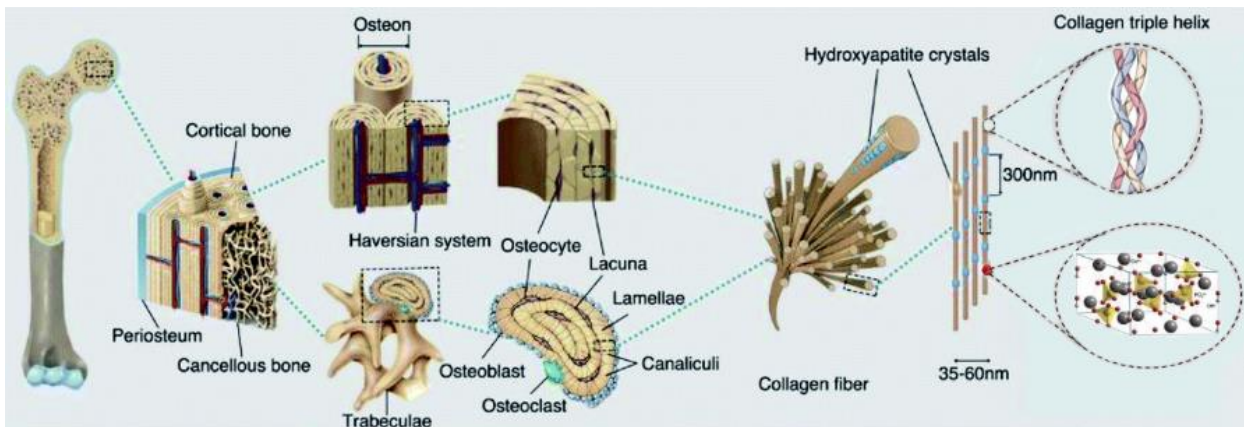


**Figure 1.1** Hierarchical structure of bone from the macro to the nanoscopic scale. (*Modified with permission from [6].*)

### 1.1.1 Bone cells, bone remodeling and regulation

Bone is a complex mineralized connective tissue responsible for locomotion, support and protection of soft organs, and calcium and phosphate storage [7]. From a chemical

---

point of view, mature bone is a composite material consisting of 45–60% (dry weight) inorganic minerals, 20–30% organic components, and 10–20% water. Most of the organic matrix of bone is composed of type I collagen while the inorganic part is mainly made of hydroxyapatite (HA) [2].

Being a living and highly dynamic tissue, bone undergoes a continuous remodeling orchestrated by specialized bone cells—osteoclasts, osteoblasts, and osteocytes [7]–[9]. Bone remodeling involves a cycle made of three key phases: initiation of bone resorption facilitated by osteoclasts, transition from resorption to the formation of new bone, and active bone formation conducted by osteoblasts [10], [11] (Fig. 1.2). Osteoblasts are generated by mesenchymal osteoprogenitor cells from periosteum and endosteum. They are responsible for bone formation by producing osteoid and generate alkaline phosphatase, a protein promoting mineralization. Once surrounded by osteoid matrix, osteoblasts transform into osteocytes and reside in lacunae [3]. Osteocytes play a fundamental role in orchestrating and coordinating the actions of bone cells, as an imbalance between bone resorption and formation can lead to bone diseases. These bone cells are interconnected and communicate through a network of channels, known as canaliculi (approximately 100 nm in diameter), enabling the transfer of molecules, nutrients, and hormones [12].

Bone tissue growth and maintenance is regulated by several hormones, such as calcitriol, parathyroid hormone (PTH), calcitonin, estrogens and androgens. Calcitriol is the most active metabolite for vitamin D and preserves bone development and health. PTH increases osteoclasts activity and calcium reabsorption, while calcitonin inhibits osteoclasts activity. Estrogens and androgens accelerate bone growth and skeletal maturation, particularly during adolescence [3].

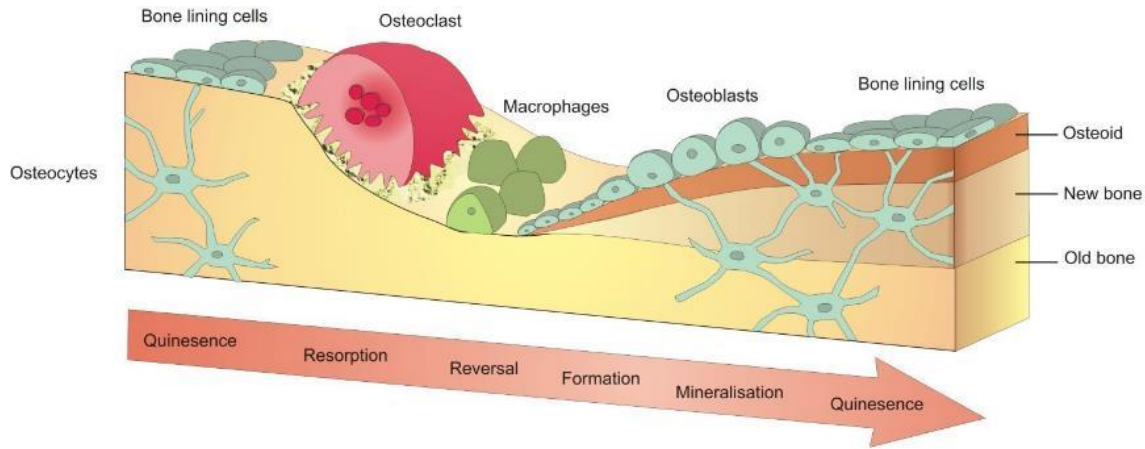


**Figure 1.2** Scheme of bone remodelling process: old bone is resorbed by osteoclasts and replaced with new osteoid secreted by osteoblasts. The process is coordinated by osteocytes. (*Adapted from <https://www.york.ac.uk/res/bonefromblood/background/boneremodelling.html>*)

### 1.1.2 Bone mineral matrix

The biological and mechanical functions of bone depend on its inorganic component which consists of a low-crystallinity carbonated HA, also referred to as bone apatite or biological apatite [13]. These biological apatites manifest as nano-sized plate-like crystals with a thickness of a few nanometers and a length in the range of a few tens of nanometers (Fig. 1.3) [14]. The crystalline structure of pure HA is described in the following as it is similar to the nanocrystals found in biological apatite. HA has a hexagonal structure fundamental for both structural robustness and mechanical functions of bone. The lattice parameters are  $a = b = 9.418 \text{ \AA}$ ,  $c = 6.884 \text{ \AA}$ , and  $\gamma = 120^\circ$  [13] (Fig. 1.4 A). The unit cell, highlighted in pink in Fig. 1.4, encompasses all the elements constituting the HA crystal. Within the unit cell, distinct sites can be identified, including calcium (Ca) sites named  $Ca1$  and  $Ca2$  types, phosphate sites ( $PO_4^{3-}$ ), and hydroxyl ( $OH^-$ ) anion sites. The  $Ca1$  sites, O, and  $PO_4^{3-}$  groups form a chain that rotates around the unit cell columns (Fig. 1.4 B,C,D). When projected down to the  $c$ -axis, each  $Ca1$  chain displays a hexagon in the  $a$ -

---

b plane, having Ca atoms as nodes (Fig. 1.4 E, with O atoms and  $PO_4$  groups in orange). The  $PO_4^{3-}$  groups link adjacent *Ca1* chains (Fig. 1.4 E). The *Ca2* atoms fill the helical *Ca1* chains around the column, and  $OH^-$  anions reside in the columns. (Fig. 1.4 F).

From a chemical point of view, bone mineral is a poorly crystalline calcium-deficient apatite, with a different Ca:P ratio with respect to pure HA (1.67). Biological apatites contain several ion substitutions; for example,  $Mg^{2+}$  may substitute  $Ca^{2+}$  ions,  $HPO_4^{2-}$  ions may replace phosphate ions, and  $Cl^-$  and  $F^-$  may substitute  $OH^-$ . Moreover, carbonate ions, the most abundant substitutions, can occupy either the  $OH^-$  (A type apatite) or  $PO_4^{3-}$  (B type apatite) sites in the crystal lattice. According to the substitution type, different lattice distortions can be appreciated [15]. The A type substitution results in a shrinkage of the c-axis and expansion of the a-axis, whereas in B type substitutions an expansion of the c-axis and a shrinkage of the a-axis is observed [1], [16]. Specifically, bone mineral is commonly found to exhibit mixed-type substitutions, with a higher prevalence of B type substitutions (A/B type ratio in the range of 0.7–0.9) [17]. Notably, in breast tissue, carbonate levels have been identified as a potential diagnostic indicator of malignancy in calcifications. In fact, benign lesions were observed to have higher carbonate levels compared to malignant ones [18], [19].

Furthermore, it is currently accepted that bone apatite nanocrystals organize in a platelet shape whose longer dimension is parallel to the c-axis of the minerals (Fig.1.5), which is in turn aligned along collagen fibres [20] (Fig.1.3). These plate-shaped bone apatite nanocrystals have average dimensions of 15 – 100 nm in width, and 0.5 – 4 nm in thickness. Despite being a crystalline hexagonal system, carbonated hydroxyapatite exhibits an amorphous fraction. This because the apatite crystals comprise two different environments, a non-apatitic hydrated domain and a more stable apatitic domain (Fig.1.5). In the interface between these domains, labile anions ( $PO_4^{3-}$ ,  $HPO_4^{2-}$ ,  $CO_3^{2-}$ ) and

cations ( $Ca^{2+}, Mg^{2+}$ ) are easily and reversibly exchangeable. During initial crystal formation, ionic exchange occurs, and ions are gradually incorporated into the interior unit cell. The maturation of the mineral is characterized by a reduction in the non-apatitic environment and an increase of the stable domains [15], [21], [22]. Furthermore, as bone minerals mature, structural defects decrease. Consequently, their composition becomes closer to stoichiometric hydroxyapatite (HA).

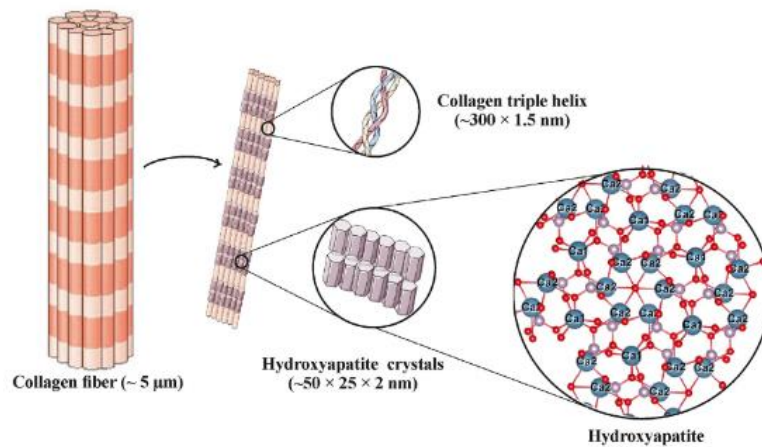


**Figure 1.3** The hierarchical structure of collagen and hydroxyapatite as main constituents of natural bone tissue. (*Adapted with permission from [14]*)



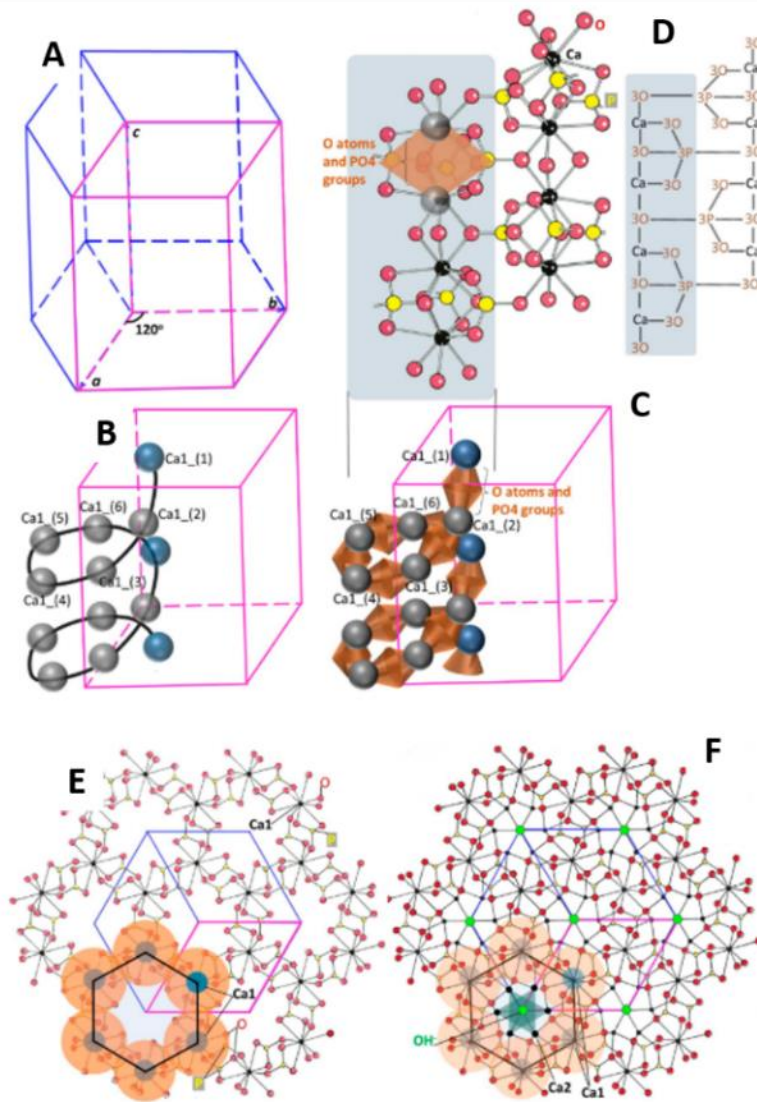


**Figure 1.4** A) Hexagonal lattice, the pink-colored frame represents the unit cell. B) Ca1 chains can be found along each column. C) and D) Each Ca1 chain is a Ca-O-P chain, with the Ca atoms connected by O atoms and  $PO_4^{3-}$  groups. D) The same  $PO_4^{3-}$  groups link neighbouring Ca1 chains. E) Projection down the c-axis, showing the hexagon formed by the Ca1 chain with Ca atoms as nodes. The O atoms and PO4 groups are represented by orange-coloured regions. Neighboring Ca1 chains link by the same  $PO_4^{3-}$  groups and share two Ca1 atoms. F) Projection down the c-axis, showing hydroxyapatite structure: Ca2 atoms fill into the helical Ca1 chains around the column and  $OH^-$  anions reside in the columns. (*Adapted with permission from [13]*)

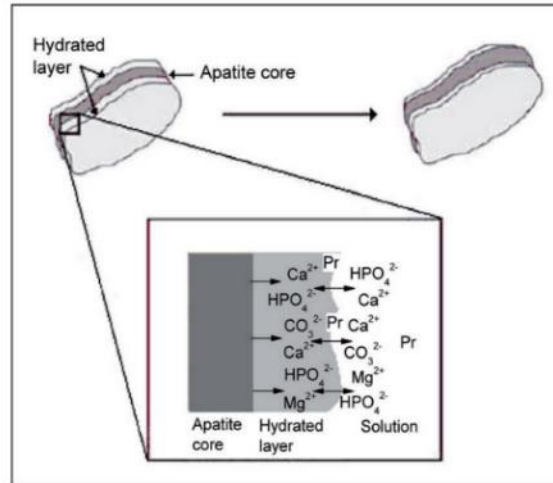


**Figure 1.5** Evolution of the apatite crystal and the surrounding hydrated layer. During maturation, the apatite domain increases and the hydrated layer decreases. (Adapted with permission from [15], [22])

## 1.2 Osteogenic differentiation

Multipotent mesenchymal stem cells can differentiate to osteoblasts through a process regulated by several transcription factors (briefly described in the following) [3]. Osteodifferentiation is initiated by Runx2 (runt-related transcription factor 2) [23] and then pursued to the immature osteoblast stage through a combination of Runx2 with osterix and  $\beta$ -catenin [24]. Osterix (Osx, Sp7) induces the expression of genes involved in immature and mature osteoblasts' mineralization, while  $\beta$ -catenin regulates osteoblastic differentiation and more generally bone formation.

Immature osteoblasts block their potential to differentiate into chondrocytic and adipocytic lineage by producing specific proteins, such as alkaline phosphatase, collagen type I, osteopontin and bone sialoproteins [24], [25]. Human alkaline phosphatase (ALP) is a membrane-bound enzyme and represents an early marker of immature osteoblast cells differentiation. ALP plays a key role in bone calcification as it hydrolyses pyrophosphate providing inorganic phosphate, fundamental for mineral formation [26]. Collagen type I

(Col1) is an early marker of osteodifferentiation and regulates cell adhesion, proliferation and differentiation in osteoblastic phenotype [27]. Bone sialoproteins (BSP) regulate calcium incorporation and nodules formation in the extracellular matrix [28]. Osteopontin (OPN) promotes absorption and mineralization of bone matrix, thus being fundamental during remodeling and bone formation processes [29]. Furthermore, during bone formation, osteoblasts secrete osteonectin (SPARC, BM-40), a protein responsible for collagen and HA crystals binding. For bone maturation to continue, Runx2 must be downregulated otherwise the immature stage of osteoblasts would be preserved [30]. Consequently, ALP expression is reduced [25]. Additionally, osteocalcin expression increases [26] (OCN) accomplishing the osteogenic maturation [30]. The scheme of mesenchymal stem cells differentiation into osteoblasts is shown in Fig. 1.6.

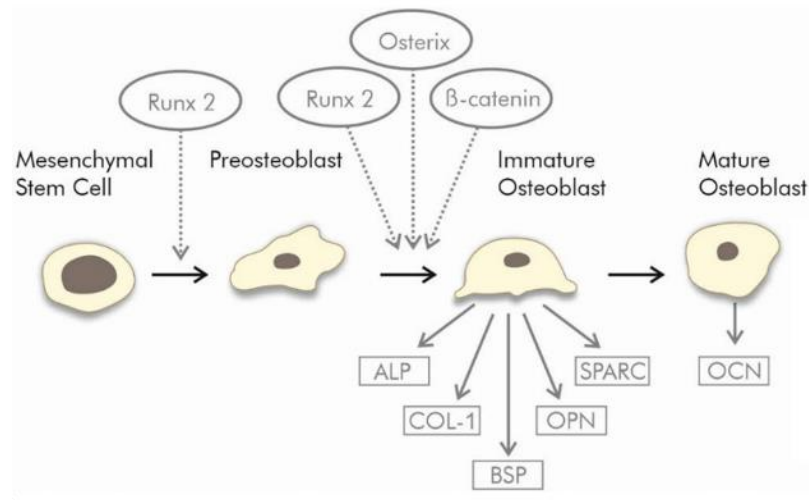


**Figure 1.6** Osteogenic differentiation of mesenchymal stem cells. (Modified with permission from [3])

### 1.3 Bone mineralization

Biomineralization is a lifelong process essential in bone formation and repair. It refers to the physiological deposition of mineral crystals in the extracellular matrix [31]. The process of bone mineralization has been considered a mere physiochemical reaction since

the early part of the 20<sup>th</sup> century. Well and Gyorgy [32] thought mineralization could occur without intermediation of cellular activity, until Sayegh et al. [32] proved cellular implication highlighting the involvement of mitochondria in the process.

In this section, bone mineralization will be outlined considering both extra and intracellular environments, with a focus on organelles and vesicular bodies. As previously stated, osteoblasts differentiate from mesenchymal stem cells in the initial phases of bone formation and are responsible for the synthesis of the mineralized extracellular matrix. Bone matrix is a complex structure consisting of collagen fibers along which nanometer-sized HA platelets orient parallel with respect to the axis of the collagen fibrils [1]. To induce cell-mediated mineralization, the organism must create an environment in which the balance between  $Ca^{2+}$  and  $PO_4^{3-}$  is altered, leading to the precipitation of a  $Ca_x(PO_4)_y$  complexes. In physiological mineralization, this nucleation process occurs through several cooperative mechanisms, with carefully regulated interaction between initiating and inhibiting molecules [33]. In the last decades, several mechanisms explaining early bone mineral formation have been proposed, but many aspects remain largely unclear. One of the hypothesized mechanisms for biomineralization consists in a cell-controlled process in which ALP reduces the level of inorganic pyrophosphate (PPi), an inhibitor of mineralization, generating inorganic phosphate (Pi), an activator of extracellular mineralization. This coupled activity of ALP alters the Pi/PPi ratio in bone microenvironment and promotes its mineralization [34]. Alternatively, another mechanism proposes that amorphous mineral precursors could be transiently produced and deposited within collagen fibrils. Amorphous minerals then transform into more crystalline apatite platelets [35].

However, the proposed models need to be further elucidated as the mineral nuclei formation process could occur intra or extracellularly. Calcium deposits are known to

---

reside intracellularly as granules in mitochondria [36]. Furthermore, other authors, including Mahamid et al., have observed the presence of calcium phosphate containing vesicles in mouse bone cells [37]. Recently, Boonrungsiman et al. [36] suggested another model that clarifies and connects the aforementioned findings. Amorphous calcium phosphate could be stored in mitochondria and transported via vesicles to the extracellular matrix before converting to a more crystalline form of apatite. The authors observed calcium containing vesicles joining calcium-containing mitochondria, suggesting a mitochondria-driven mechanism for calcium storage and transport. Probably, ionic calcium (and phosphate) is transferred from mitochondria to intracellular vesicles, through a direct process such as diffusion [36]. Additionally, Tang et al. have proposed a mechanism to reveal mitochondrial granules formation. Mitochondrial granules are likely to be built in the endoplasmic reticulum, where calcium and phosphate clusters are generated and transported into mitochondria [38].

## 1.4 Bone sarcomas

Bone sarcomas are a mesenchymal tumor family originating from bone and exhibit highly heterogeneous subtypes. The mainly known bone sarcomas are osteosarcoma, Ewing sarcoma and chondrosarcoma. Among all rare sarcomas, undifferentiated pleomorphic sarcoma (UPS) accounts for approximately 2% of primary malignant bone tumors. The genesis of bone sarcomas can be attributed to a mechanism based on an oncogenic event taking place in a microenvironment that promotes cancer growth and migration. These events are likely to occur during mesenchymal stem cells differentiation (MSCs) [39].

Osteosarcoma (OS) mostly affects children and young adults [40]. It usually occurs in the metaphysis of long bones where high turnover takes place [41] (mainly femur and tibia). Osteosarcomas can be divided into high-grade and low-grade sarcomas. The latter

are very different in their clinical, pathologic and therapeutic-prognostic features and are classified as periosteal OS, parosteal OS and low-grade central OS (described in the following).

Parosteal OS (Fig. 1.7) anatomically originates from the outer layer of the periosteum [42]. The bone matrices produced are often arranged in long parallel streamers outside the periosteum. At radiography, it appears as a lobulated and exophytic mass with central dense ossification adjacent to the bone. Cortical thickening is present as well. Periosteal OS is a rare tumor and usually occurs along the diaphysis of long bones, most commonly in the tibia (Fig. 1.8) [42]. The tumor arises from the inner layer of periosteum and has a predominantly cartilaginous component. Common radiographic features include a soft-tissue mass with periosteal reaction, cortical erosion and thickening. Periosteal reaction often extends perpendicularly from the inner cortex to the outer margin of the tumor.

OS generates when mesenchymal cells produce osteoid and immature bone [41], and more rarely, the tumor may arise in the soft tissues. Although its origins have not been fully elucidated, several investigations have suggested osteogenic differentiation dysfunctions as key factors in OS etiology [43], [44]. During osteoblastic differentiation, affected cells are likely to arrest at an undifferentiated stage producing malignant bone tissue [45]–[47]. OS cells seem to interact with growth factors like their early osteoprogenitors and proliferate, leading to cancer progression and invasion. Interestingly, it has been observed that more malignant OS phenotypes share similarities with early osteogenic progenitors, while less aggressive ones resemble more differentiated bone mesenchymal stem cells (bMSCs) [43], [48].

Chondrosarcoma mainly occurs in the proximal femur, with a small percentage arising in soft tissue [5]. In the long bones, it generally originates in the medullary cavity of the metaphysis. The tumor is characterized by a chondrocyte-derived hyaline-like

---

extracellular matrix, which encases malignant cells. With respect to OS, it exhibits low vascularization [49].

UPS is a malignant high-grade tumor with fibroblastic differentiation alteration. It is characterized as a mixture of atypical fibroblasts and pleomorphic undifferentiated cells arranged in a storiform pattern. It is commonly found in the metaphysis of long bones, being femur, tibia and humerus the most frequent locations [50].

The typical features and symptoms of bone sarcomas are local pain, followed by localized swelling and limitation of joint movement. In some cases, a pathological fracture can be the first sign of disease [41]. The diagnosis is achieved through the combination of both clinical and radiographic approaches. Radiography and computed tomography are conventionally employed to investigate osseous changes. Magnetic Resonance Imaging (MRI) is used to assess the soft tissue component, monitor tumor relationship with surrounding tissues, vessels and nerves and its intramedullary extension. The final and necessary step to diagnosis is biopsy. In the context of such complex pathologies, a multidisciplinary approach consisting of cooperation between orthopedic surgeons, radiologists and histopathologists is fundamental to correctly diagnose the disease. A multidisciplinary approach is also needed in the treatment of patients, having bone sarcomas treatment long-term adverse effects that can affect patients' life quality [47].

The management of OS is based primarily on neoadjuvant chemotherapy, surgical resection and adjuvant chemotherapy. Currently, surgical treatment of localized OS preceded by neoadjuvant chemotherapy and followed post-operative therapies is the most diffused modality. Importantly, thanks to neoadjuvant chemotherapy, limb-salvage surgeries are possible in most cases [51]. More rare sarcomas, such as UPS, commonly follow OS's treatment procedure, while in chondrosarcoma, surgical management is performed as both radiation and chemotherapy have been shown to be ineffective [39].

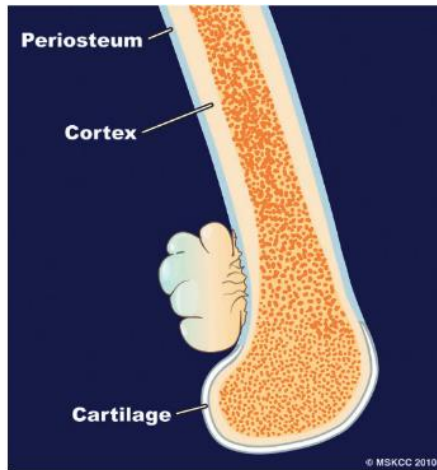


**Figure 1.7** Scheme of parosteal OS showing tumor typical structure. (Adapted with permission from [42])

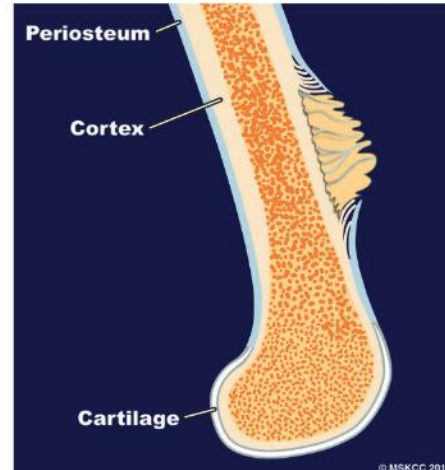


**Figure 1.8** Scheme of periosteal OS showing tumor typical structure. (Adapted with permission from [42])

## 1.5 Osteoblasts cell model in vitro research

The in vitro study of osteosarcoma is carried out employing different types of cells. Due to limited availability of primary human osteoblast cells [52], osteosarcoma-derived cells are commonly used as osteoblastic models. Primary human osteoblasts isolation from bone explants is a non-trivial process that can be performed through enzymatic digestion and spontaneous culture of bone fragments. Moreover, the behavior and characteristics of human osteoblastic cells strongly depend on site of isolation, age of the individual and gender differences. For all these reasons, osteosarcoma cell-lines are preferred as osteoblastic models. They present several advantages, like ease of maintenance, unlimited number of divisions and relative phenotypic stability. On the other hand, some disadvantages may arise from populations heterogeneity, full range of phenotypic characteristics of the original cells not expressed and non-physiological proliferation due to loss of contact inhibition [53]. The currently available culture models for osteoblastic



---

differentiation in vitro study include non-tumor immortalized cell lines, malignant cell lines (SaOS-2) and pluripotent stem cells induced to differentiate [53].

### 1.5.1 Characteristics of SaOS-2 cell line

SaOS-2 cell line [54] was isolated in 1975 from an 11-year-old Caucasian female. The cell-line has been characterized by Rodan and colleagues [55], and it has been widely used as an in vitro model with "normal" osteoblastic behavior. These cells show a mature osteoblastic phenotype characterized by a higher level of ALP activity (4-6  $\mu\text{mol}/\text{mg}/\text{min}$ ) if compared to other OS cell lines, such as MG-63 and SaOS-1 (2.5  $\text{nmol}/\text{mg}/\text{min}$ ). In the early phases of culture, the ALP level is comparable to human osteoblastic cells [53] but shows a 120-fold increase after 14 days of culture under the same conditions. It has been reported that SaOS-2 ALP activity can be induced by dexamethasone and by phosphate substrates, thus generating different cellular phenotypes [56]. As expected, SaOS-2 cells share several similarities with human osteoblastic cells as they express the typical osteoblastic markers osteocalcin, bone sialoprotein and collagen type I, and have slow proliferation (if compared to other OS cell lines) comparable to human osteoblasts. Moreover, the expression of cytokines and growth factors is similar to human osteoblastic cells, as well as the expression of PTH and calcitriol [57]. Interestingly, SaOS-2 cells produce calcified matrix typical of woven bone [55]. It is noteworthy, that the structure of collagen synthesized by SaOS-2 cells is very similar to the collagen formed by human osteoblasts but exhibits higher levels of lysine hydroxylation [3]. Unlike osteoblasts, SaOS-2 cell line has been tested positive for type IV collagen and expresses, in late phases of cell culturing, osteocytes' characteristic genes. In addition, further alterations in the protein expression pattern are present. Among them, tumor protein P53 down-regulation is certainly the most relevant. Despite originating from osteosarcoma, its capacity to generate

mineral matrix and to retain osteodifferentiation markers, makes SaOS-2 cell line the most representative and convenient model for studying human osteoblasts' differentiation in vitro [3].

### 1.5.2 Calcium depositions genesis in SaOS-2 cells

SaOS-2 cell line has been shown to form calcined matrix in vitro [55]. Based on the assumption that calcium carbonate compounds may act as bioseeds onto which calcium phosphate is layered, we report in the following the main findings on calcium depositions formation in SaOS-2 cells.

Calcium carbonate and calcium phosphate depositions formation are both exergonic processes. Like most biological reactions forming skeletal elements, these reactions are controlled by enzymes which regulate metabolites or ions transport systems [58]. In the context of mineral deposits formation, the prime enzymatic candidate is the carbonic anhydrase (CA) [59]. CA acts both as a calcium carbonate anabolic enzyme, facilitating and accelerating bicarbonate formation [60], which is a precursor of calcium carbonate synthesis, and as a catabolic enzyme that promotes calcium carbonate dissolution [61]. Thanks to EDX (Energy Dispersive X-ray analysis) mapping, it has been observed that calcium phosphate deposits generated by SaOS-2 cells are not only rich in Ca and P, but also in C [58]. This reveals CA involvement in bone formation [62], as the enzyme accelerates calcium carbonate formation constituting a substrate for phosphate deposition. The bulk of these data might indicate that carbonate and phosphate calcium deposits are co- or sequentially synthesized by SaOS-2 cells. In support of that, Sorrentino et al. [63], have recently shown that calcium carbonate acts as HA precursor in bone mesenchymal stem cells (bMSCs) induced to differentiate towards osteoblasts. Despite all these observations, until now, no biochemical data have elucidated the predicted replacement of carbonate anion by a phosphate anion, generating calcium phosphate. The involvement of

---

phosphates groups in this process can be further explored. It has been reported that orthophosphates, originating either from polyphosphates or organic-phosphate ( $\beta$ -glycerol phosphate), often act as a substrate for calcium phosphate and HA synthesis [64]. In a work by Werner et al. [58], both orthophosphates and the hydrolytic products of polyphosphates displayed an inhibitory effect on CA, inactivating calcium carbonate bioseeds formation. [65] Finally, polyphosphates have been observed to cause an increased expression of genes involved in biomineralization such as ALP.

To summarize, in a coupled reaction biochemical system driven by CA, calcium carbonate is likely to be dissolved via bicarbonate, and in turn the released  $Ca^{2+}$  ion becomes accessible to orthophosphates, generating insoluble salt calcium phosphate. Interestingly, the process is regulated by a negative feedback by which phosphoric acid, enzymatically released from polyphosphates via ALP, inhibits CA and prevents further enzymatic synthesis of calcium carbonate [65].

## 1.6 Synchrotron-based techniques

Since their discovery in late 1895 by William Rontgen, X-rays have played a pivotal role in medicine, biology, physics and chemistry allowing to characterize morphology, chemical composition and structure of materials [66]. At the time of the discovery, the nature of the radiation being completely unknown, the terminology X-rays was adopted. Later, X-rays were identified as electromagnetic waves with wavelengths in the range 0.025-25 Å [67]. X-rays' characteristics make them a challenging probe to investigate properties of materials as they can penetrate deeply and non-destructively into solids depending on energy and electronic density of materials. When X-rays photons have wavelengths in the range of the typical atomic distances, they can be scattered from atoms leading to diffraction. Furthermore, photons energy can be tuned to trigger electronic

transitions so that both chemical nature and electronic properties of the material can be investigated [66].

X-rays are generated by laboratory sources (X-ray tubes, rotating anodes) and dedicated facilities, called synchrotrons. Synchrotrons produce beams of electromagnetic radiation from the infrared to the hard X-ray regime. These facilities produce an electronic beam which is accelerated and injected into evacuated storage rings where electrons can circulate at highly relativistic velocities. Bending magnets, undulators and wigglers, located along the ring, perturb electrons trajectory provoking a tangential emission of photons (synchrotron light). The emitted synchrotron light is delivered to beamlines, located tangentially to the beam, and then tuned to fit specific applications (Fig. 1.9) [67]. Among them, X-rays techniques like X-ray diffraction, X-ray absorption spectroscopy, and X-ray imaging, provide unique insights into the structural, chemical, and electronic properties of materials. Synchrotron radiation possesses several distinctive properties that make it a powerful tool for various scientific applications:

1. High intensity: synchrotron radiation is exceptionally bright, providing intense beams of light across a wide spectral range;
2. Broad spectrum: synchrotron radiation spans a broad spectrum from infrared to hard X-rays which allows researchers to tailor experiments to the specific characteristics of the material under investigation;
3. Collimation and directionality: the emitted synchrotron radiation is highly collimated and directional, facilitating precise investigations of small-scale structures and details;
4. Tunability: beamlines can tune the energy of the emitted radiation to match the absorption edges of specific elements in materials, enhancing the selectivity of experiments;

5. Coherence: synchrotron radiation exhibits high spatial and temporal correlation of the wavefront, advantageous for X-ray diffraction and imaging;
6. Polarization: beneficial for studies that are sensitive to the polarization state of the incident light;
7. Pulsed nature: advantageous for time-resolved experiments, capturing dynamic processes with high temporal resolution.

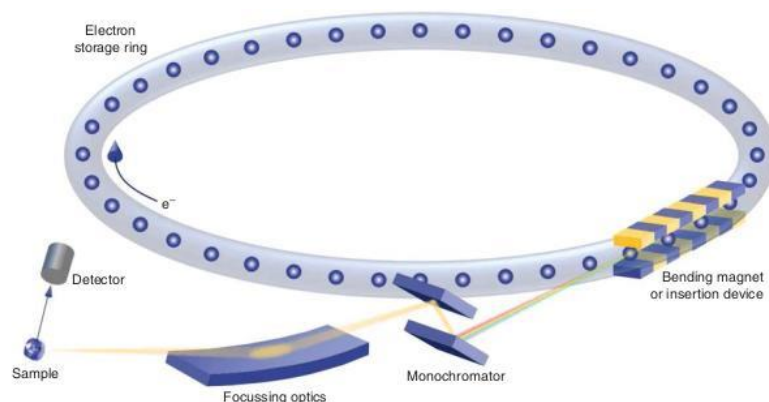


**Figure 1.9** Schematic of a synchrotron. Electrons travel at highly relativistic velocities in an evacuated storage ring and emit electromagnetic (synchrotron) radiation as their direction is changed by ‘insertion devices’ placed along the storage ring. At the beamlines (tangential to the storage ring), the radiation can be tuned and focused using X-ray optics to investigate a sample. (*Adapted with permission from [66]*)

### 1.6.1 X-ray Absorption Spectroscopy (XAS)

X-ray absorption spectroscopy (XAS) refers to the phenomenon of X-ray absorption by a tightly bound core electron which is ejected from the atom. XAS measurements need an intense and tunable X-ray energy source which can be provided by synchrotron facilities. The technique comprises both X-ray fluorescence (XRF) and X-ray absorption fine structure (XAFS). XAFS, in turn, includes X-ray absorption near-edge spectroscopy (XANES) and extended X-ray absorption (EXAFS) spectroscopy.

X-rays are electromagnetic waves with energies in the range 500 eV-500 keV. At this energy regime, X-rays can be absorbed by matter generating the well-known photoelectric effect. Specifically, an X-ray photon can be absorbed by an electron from a tightly bound core level of an atom (Fig. 1.10 A). For this interaction to happen, the binding energy ( $E_0$ ) of the core electron must be lower than the energy of the incident X-ray and the selection rules for the angular momentum state must be satisfied. If there is an available electronic state, the X-ray is absorbed and the electron in the available state is removed from its quantum level and ejected from the atom (Fig. 1.10 A) [68]. When discussing XAS, the absorption coefficient ( $\mu$ ) is used to describe the probability that an X-ray of energy  $E$  is absorbed by matter.  $\mu$  is expressed by the Lambert-Beer law:

$$I = I_0 e^{-\mu t} \quad (1.1)$$

where  $I_0$  is the intensity of the incident beam,  $t$  is the sample thickness, and  $I$  is the transmitted intensity [67]. Far from absorption edges, absorption coefficient is proportional to the fourth power of  $Z$  and inverse proportional to the cube of the energy [69]. This dependence constitutes the fundamentals of all X-rays based imaging techniques (CT, radiography), where contrast is generated because elements absorb differently according to their atomic number. For example, soft-tissue elements ( $Z \leq 8$ ) have low absorption coefficient and, to image such elements with sufficient contrast, different imaging techniques have been developed. Among them, soft X-ray microscopy and phase-contrast micro-computed tomography that will be described in Section 1.6.2. Following an absorption event, the atom has an empty electronic core level (vacancy) and emits a photoelectron. The atom can relax from its excited state in two ways, by emitting photons or a secondary electron. X-ray fluorescence is the mechanism according to which an electron from a higher electronic core level fills the inner core hole ejecting a photon at a well-defined energy (Section 1.6.1.2). Auger effect consists in an emission of a second

---

electron in the continuum after the filling of the vacancy from a higher electronic level electron [68]. The main advantage of XAS relies on the fact that, since each electronic core-level of an atomic species possess a well-defined binding energy, it is possible to select the element to probe by tuning the incident photon energy to a specific and tabulated binding energy. When the incident beam is well-tuned, there is a sharp rise in absorption which is identified in spectroscopy by an absorption edge. The application of this principle to molecules, liquids and solids constitutes XAFS.

#### 1.6.1.1 X-ray Fluorescence Microscopy (XRFM)

X-ray fluorescence imaging elucidates the spatial distribution of the chemical elements contained in a sample of interest and is based on the phenomenon of X-ray fluorescence excitation. Absorption of X-ray radiation by matter generates a photon-electron interaction in the inner levels of atoms' shells. If the energy of the incident photon is greater than the binding energy of an electron, the electron is knocked out from the atom producing a sharp rise in absorption (Fig 1.10 A) [70]. Due to the electron expulsion, an electron from an external shell fills the vacancy in the inner shell emitting a photon (fluorescence Fig. 1.10 B). If the excess energy remaining after the relaxation of the electron from an outer shell is used to eject a second electron, the phenomenon observed is called Auger emission (Fig. 1.10 C). Differences in electron binding energies depend on the orbital occupied. Electronic shells are marked by capital letters ( $K$ ,  $L$ ,  $M$ ,  $N$ ) and the closer the shells are to the nucleus, the higher the electron binding energy [71]. Furthermore, in an atom, not all transitions are allowed. The relaxation of an electron from one bound electronic state to another follows the selection rules for electronic dipole radiation [70].

In fluorescence, the energy of the emitted photon corresponds to the difference between the energy of the incident photon and electron binding energy and thus, it depends only

on the energy of the electronic levels which are specific for each element. As each atom possesses a finite number of levels and only some transitions are possible, the emitted photon is also called characteristic X-ray radiation. The characteristic radiation provides a discrete spectrum which represents the fingerprint of a specific chemical element [71]. The emitted fluorescence is represented as lines defined by the letters  $K$ ,  $L$ ,  $M$  indicating which electronic shell had the original vacancy, and by the subscript  $\alpha$  or  $\beta$ , identifying the outer shell from which the electron relaxes by emitting fluorescence. For example, a  $K_\alpha$  line is produced by a vacancy in the  $K$  shell which is filled by an electron relaxing from the  $L$  shell ( $\alpha$ ). A  $K_\beta$  line, is produced by a vacancy in the  $K$  shell filled by an  $M$  shell electron (Fig. 1.11).

Information on the 2D distribution of the chemical elements constituting a sample can be obtained by raster scanning the specimen with a focused X-ray beam. The conventional synchrotron-radiation setup consists of a  $45^\circ/45^\circ$  geometry (Fig. 1.12) where the sample is inclined by  $45^\circ$  with respect to the incident beam and the detector is perpendicular to the beam.

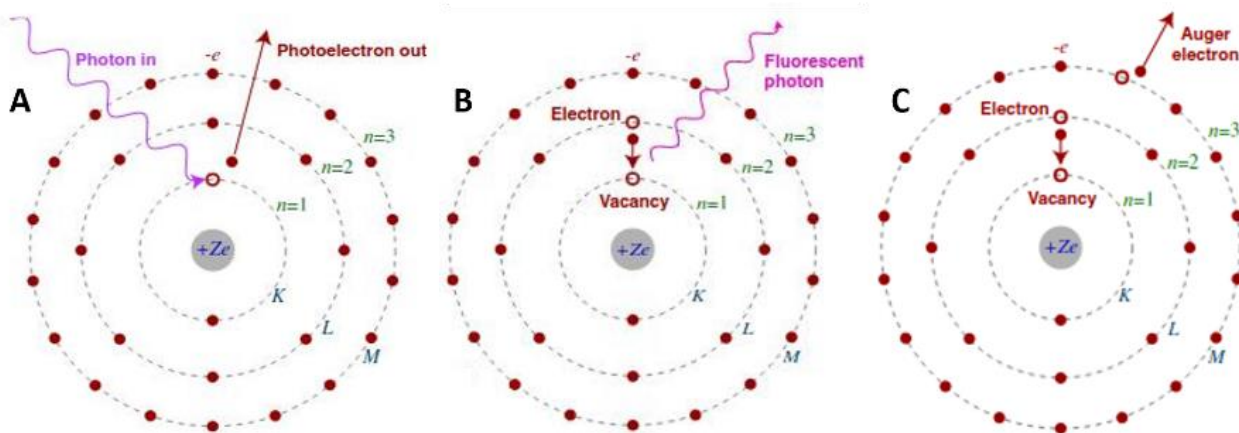


**Figure 1.10** The absorption of an x-ray photon and ejection of a core electron (A). The generated vacancy can be filled by an electron from an outer shell and the excess energy can be emitted as characteristic x-ray radiation (B) or by ejecting an Auger electron (C).



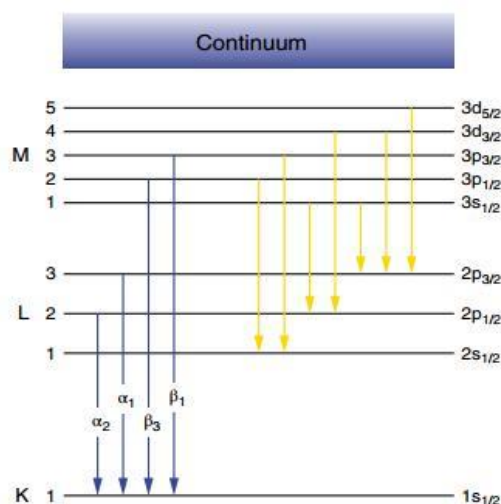


**Figure 1.11** The Siegbahn nomenclature of x-ray fluorescence lines. The blue set represents  $K$  emission, the yellow set  $L$  emission. (Adapted with permission from [66])

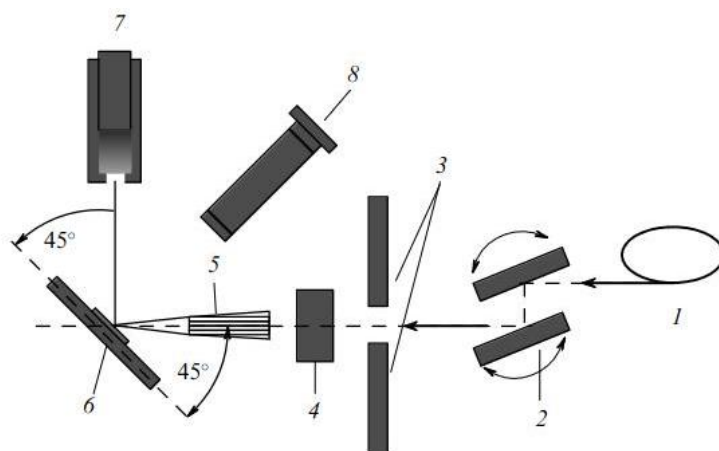


**Figure 1.12** Typical setup for fluorescence microscopy: 1 is the SR source, 2 is the monochromator, 3 is the slit system, 4 is the ionization chamber, 5 is the focusing optics, 6 is the sample, 7 is the detector, and 8 is the light microscope. (Adapted with permission from [70])

### 1.6.1.2 X-ray Absorption Fine-Structure Spectroscopy (XAFS)

XAFS technique studies the modulation of X-ray absorption probability due to the chemical and physical state of atomic species. The XAFS spectrum is usually divided into two regimes: XANES and EXAFS (Fig. 1.13) [68]. XANES is sensitive to the oxidation state and the coordination chemistry of the absorbing atom, while EXAFS describes

distances, coordination number and species of the absorbing atom's neighbors. XAFS is element specific and sensitive to the short-range order of the absorbing atom, as compared to X-ray Diffraction (XRD in Section 1.6.3) which describes the long-range structural order [67]. Hence, XAFS can be applied to characterize amorphous materials and disordered systems, including solutions.

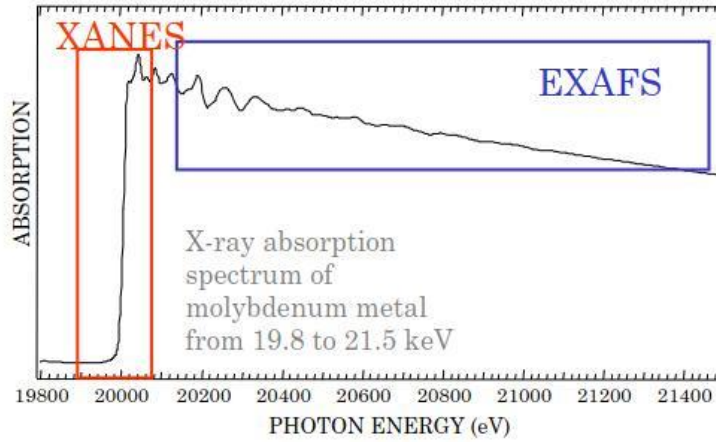


**Figure 1.13** X-ray absorption spectrum of molybdenum metal divided in XANES and EXAFS regions.

Conventionally, in XAFS, absorption is measured through the intensity of  $\mu$  as a function of the incident beam energy near and at energies above the absorption edges. Absorption can be measured in transmission as:

$$\mu(E) = \log\left(\frac{I}{I_0}\right) \quad (1.5)$$

or in X-ray fluorescence:

$$\mu(E) \propto \frac{I_f}{I} \quad (1.6)$$

where  $I_f$  is the intensity detected for a specific fluorescence line.

XAFS process can be physically described through the photoelectric effect, according to which, upon X-ray absorption, a photoelectron is emitted by the absorbing atom (Fig. 1.14). The description becomes more complicated when a neighboring atom is added. The

photoelectron, after leaving the absorbing atom, can scatter from the neighboring atom and return to the absorbing one, thus altering  $\mu(E)$ . Formally, being X-ray absorption a transition between two quantum states,  $\mu(E)$  can be described with Fermi's Golden Rule:

$$\mu(E) \propto |\langle i | H | f \rangle|^2 \quad (1.7)$$

where  $\langle i |$  is the initial state represented by a core electron,  $|f \rangle$  is the final state represented by a core-hole and a photoelectron, and  $H$  is an interaction term. Since the core-level electron is tightly bound to the atom, the initial state won't be affected by the presence of the neighboring atom [68]. On the other hand, the final state will be perturbed.  $\mu(E)$  can be expanded and rearranged in the following configuration:

$$\mu(E) = \mu_0(E)[1 + \chi(E)] \quad (1.8)$$

where  $\mu_0(E)$  depends only on the absorbing atom as if there were no neighbors and  $\chi(E) \propto \langle i | H | \Delta f \rangle$  is the fine-structure contribution and depends on the effect of the neighboring atoms by a term  $\Delta f$ . The term  $H$  represents the momentum states and is proportional to  $e^{ikr}$ . If we approximate the initial state with a  $\delta$  function:

$$\chi(E) \propto \int \delta(r) e^{ikr} \psi_{SCATT}(r) dr = \psi_{SCATT}(0) \quad (1.9)$$

where  $\psi_{SCATT}$  is the wave function scattered by the photoelectron. This relation, also known as EXAFS equation, depends on the amplitude of the scattered photoelectron and it is used to describe EXAFS spectra. On the contrary, there is not a simple analytic description for XANES spectra. In fact, EXAFS equation breaks down at low  $k$  due to a  $1/k$  dependency, introduced by the description of the out-going photoelectron through a spherical wave-function [68].

XANES spectrum is delimited by energies that range from  $-50$  eV below the absorption edge to  $100$  eV above. Below the absorption edge, the spectra are linear and smooth, increasing sharply when the binding energy is reached (edge-jump), and then oscillate

beyond it. The position and shape of the absorption edges are generally influenced by the oxidation state, coordination number, ligand type chemistry of the absorbing atom [67].

In the context of this thesis, the chemistry of calcium compounds has been considered of paramount interest. In the following, XANES Ca *K-edge* and XANES Ca *L<sub>3,2</sub> - edge* spectra of calcium compounds will be briefly described and shown. Bone is a composite material made of a low-crystallinity carbonated HA embedded in a collagen matrix. Due to its composition, bone is an ideal target for XAFS spectroscopy as the technique can yield a chemical fingerprint of  $\text{Ca}^{2+}$  bonding configuration and symmetry [72]. However, despite the increasing interest in calcium and its compounds both in biology and industry, the origin of specific spectral features has not been understood yet.

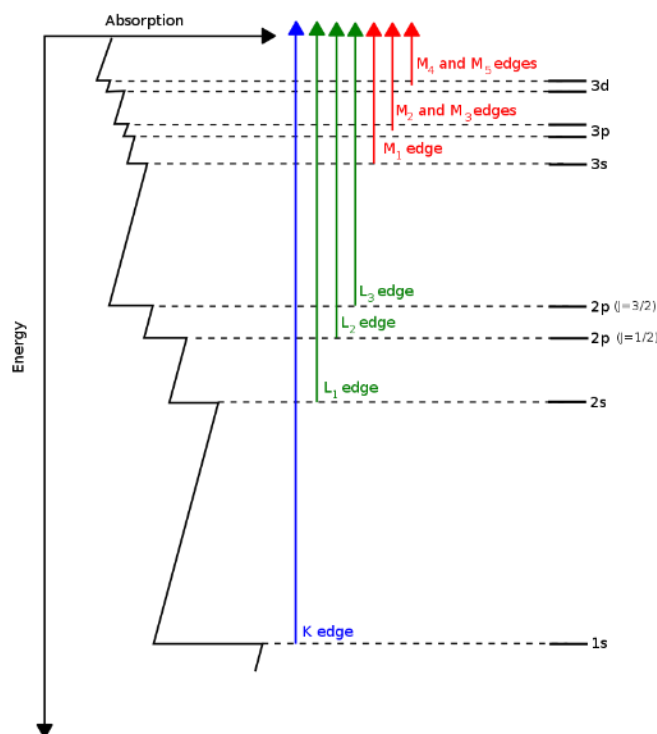


**Figure 1.14** Core electron excitation from K, L, and M band edges. (Adapted from <http://creativecommons.org/licenses/by-sa/3.0>).

### XANES at the Ca K-edge

From the spectral point of view (Fig. 1.15 A), calcite is clearly identified through two weak split pre-edge peaks in A representative of  $1s$  to  $3d$  transition, the shoulder in B identifies a transition from  $1s$  to  $4s$  molecular orbitals and the edge/post-edge signals in C and D complete the white line. In literature, the reduction in number of features has been attributed to an increase in structural disorder in the sample [73], [74].

Given a XANES spectrum of an HA reference sample, it is possible to identify up to eight structures, labelled from A to H in Fig. 1.15 B. The features in the pre-edge region (A) are commonly attributed to electronic transitions from the  $1s$  energy levels to bound  $3d$  or O  $2p$  molecular orbitals. As energy increases, it is possible to appreciate the white line, composed of a shoulder-like structure, assigned to the  $1s$  to  $4s$  transition (B), and a principal peak (C) corresponding to the  $1s$  to  $4p$  transition [75]. Features in D are generated mainly by transitions to unoccupied states from  $5s$  states and the XANES structures labelled from E to H are mainly due to multiple scattering contributions.

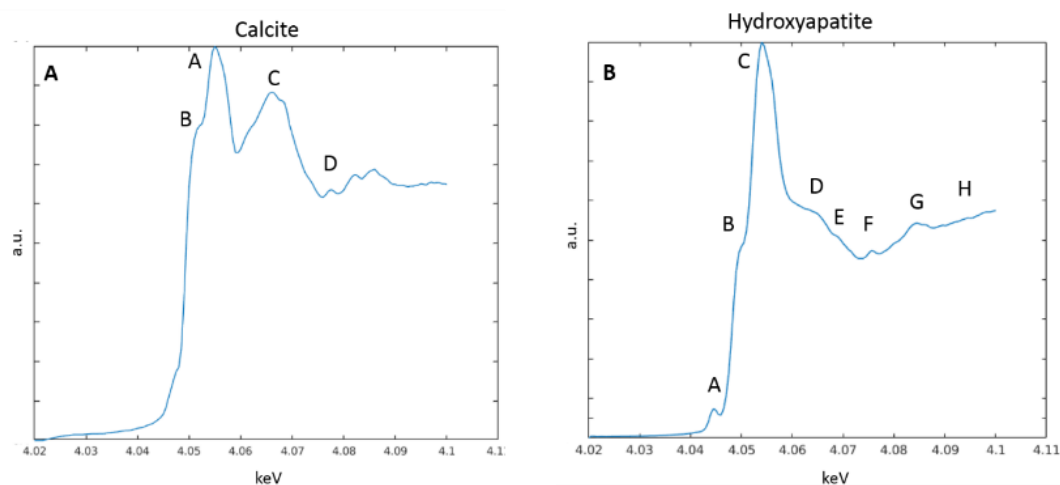


**Figure 1.15** XANES spectra at the Ca K-edge of calcite (A) and HA (B) references.

### XANES at the Ca $L_{3,2}$ – edge

The features of XANES Ca  $L_{3,2}$  – edge of  $\text{Ca}^{2+}$  in octahedral symmetry were first described by de Groot et al. [76] for  $\text{CaF}_2$ . Since then, other calcium compounds have been characterized [72], [77]. The main spectral features of calcite and HA spectra from references (Sorrentino et al. [63]) are provided in the following (Fig. 1.16 A and B). The  $\text{Ca}^{2+}$  cation has no  $3d$  electrons, hence,  $2p$  absorption is determined by the transitions from  $2p_63d_0$  to  $2p_53d_1$  which generate the two main absorption peaks,  $L_3$  and  $L_2$  indicated as  $a_2$  and  $b_2$  in Fig. 1.16. The peaks appearing before the absorption edges are assigned to crystal field splitting that introduces new transitions that wouldn't be allowed in symmetric environments, affecting both energy position and intensity of the peaks. In HA spectrum, the pre-peak before  $L_2$  shows the typical “hook” shape feature. In addition, the calcite spectrum has very strong pre-edge peaks if compared to HA (Fig. 1.16 A). From this comparison, one can infer that XANES spectra are unique in terms of intensity and number of peaks. Although no structural information about the calcium sites can be quantitatively derived from the spectrum alone, this uniqueness makes Ca  $L_{3,2}$  – edge XANES spectroscopy a powerful tool for probing local calcium structure in different materials through comparison with reference spectra [78].

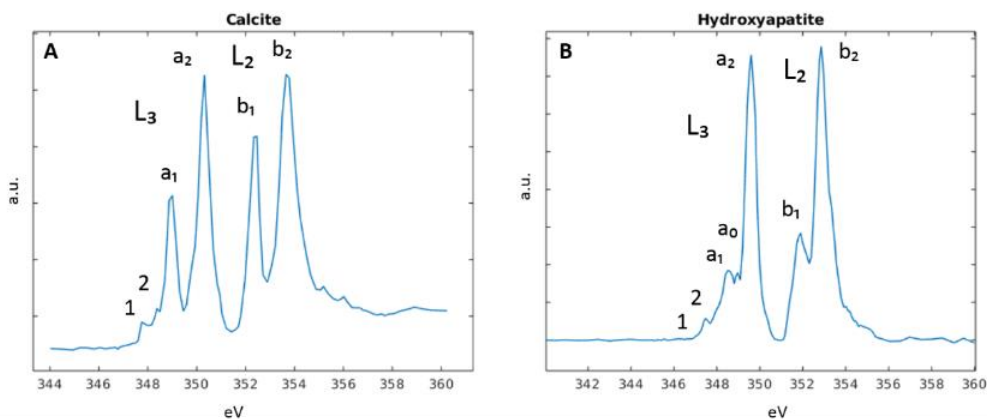


**Figure 1.16** Calcite (A) and HA (B) XANES Ca  $L_{3,2}$  – edge spectra. The main spectral features are indicated in letters.

## 1.6.2 Synchrotron radiation-based imaging

The discovery of X-rays in 1895 opened the way to imaging techniques based on the interaction of electromagnetic radiation with matter. Radiographs of objects were first obtained and up to now, thanks to technological advances and the use of synchrotron light sources, new X-rays imaging techniques have been developed. In the following, we describe soft X-ray microscopy and tomography, and phase-contrast computed tomography [79].

### 1.6.2.1 Soft X-ray microscopy and cryo-Soft X-ray Tomography (cryo-SXT)

X-rays mainly interact with the inner shell electrons of atoms, making microscopy sensitive to elements and bonds between atoms [79]. Currently, thanks to advances in X-ray sources, focusing optics and specimen preparation methods, X-ray microscopy provides high resolution details in biological specimens [80]. The technique allows to probe matter at high resolution providing complementary information to that obtained by optical and electron microscopes [81]. Soft X-rays have a photon energy between 100 and 1000 *eV*, corresponding to wavelengths in the 1 to 10 *nm* range [80]; which give higher spatial resolution than longer wavelengths at the diffraction limit [82]. The technique achieves good contrast in natural aqueous environments using the wavelengths between the inner-shell absorption edges of oxygen and carbon, 2.3 and 4.4 *nm* corresponding to an energy range between 284 – 543 *eV*, called water window. Photons within this window are absorbed nearly 10 times stronger by carbon than by water (oxygen), allowing for a direct visualization of cell structures [83]. With this technique, it is possible to image hydrated cells up to 10  $\mu\text{m}$  thickness, but the exposure required for imaging at 30 *nm* (or higher) resolution would lead to radiation damage by breaking chemical bonds in the sample. To avoid radiation damage sample cryogenic fixation is necessary [80]. Furthermore, cryo X-ray microscopy allows to study cells in a quasi-native state without modifications arising from chemical fixation.

The optical setup of a soft X-ray microscope is similar in concept to that of a bright-field microscope (Fig. 1.17). A condenser lens illuminates the specimen, and an objective focuses the transmitted light onto the detector. In presence of X-rays, Fresnel zone plates are the optics chosen as they can produce a focal spot with a Rayleigh resolution limited to 1.22 times the width of the narrowest zone that can be produced. Zone plates rely on diffraction to focus the light and consist of radially symmetric rings, Fresnel zones, alternatively opaque and transparent [80], [83]. To summarize, the condenser illuminates the sample with a desired FOV, typically between  $10 \mu\text{m} \times 10 \mu\text{m}$  and  $16 \mu\text{m} \times 16 \mu\text{m}$ , and the objective Fresnel zone plate lens after the sample forms an image of the FOV onto the detector [84].

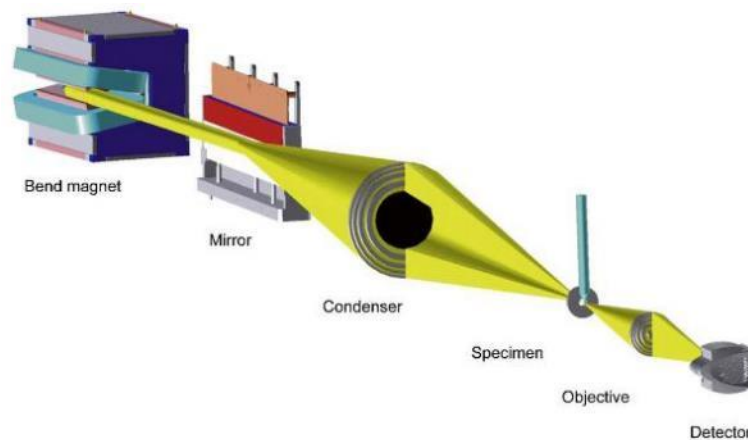


**Figure 1.17** Schematic representation of the main components of a soft X-ray microscope designed for cellular imaging. (*Adapted with permission from [83]*)

As previously mentioned, soft X-ray microscopy images  $10 \mu\text{m}$  thick samples. Images acquired from specimens of this thickness will present many superimposing structures [82]. Therefore, 3D imaging becomes crucial to resolve the high complexity of biological specimens. If enough 2D images are recorded at incremental angles around a rotation (tilt) axis, 3D tomographic reconstruction of the sample can be performed [85]. The principles



of tomography are graphically resumed in Fig 1.18. Projection images are acquired at specific angular intervals over a total range (ideally  $180^\circ$ ) and processed to retrieve a 3D reconstruction of the specimen either by filtered-back projection or by algebraic reconstruction methods [86]. In the water window, specifically at  $520\text{ eV}$  for tomographic acquisitions shown in this thesis, the practical angular rotation range is  $110^\circ$  due to setup geometrical limitations. This limited tilting range results in regions missing information in the Fourier space (missing wedge), leading to an elongation of volumes along the beam direction [84], [87].

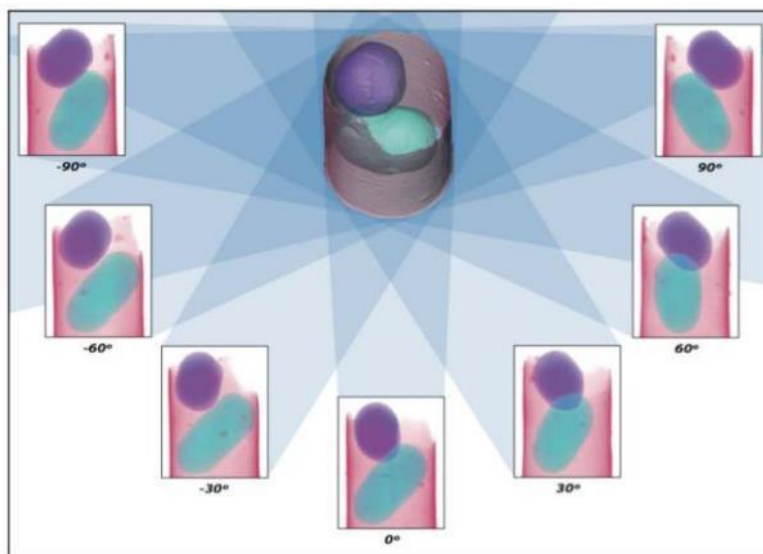


**Figure 1.18** 3-D reconstruction scheme of two cells in a glass capillary calculated from 2-D projections collected sequentially around a rotation axis (shown at  $30^\circ$  increments). (*Adapted with permission from [83]*)

### 1.6.2.2 Phase-Contrast micro-Tomography (PhC micro-T)

Conventional X-ray imaging techniques (radiography and computed tomography) measure X-ray beam's intensity attenuation when passing through a sample [88]. However, when imaging low-Z samples, such as biological tissues, at high energy (hard X-ray), the contrast generated by the absorption from various materials might be insufficient to resolve different structures. Propagation phase-contrast imaging converts phase shifts

(phase distortions), occurring when X-rays travelling through a sample refract, into intensity variations that are recorded by the detector. These phase effects, which do not contribute to the image formation in conventional techniques, can be stronger than attenuation when a soft tissue is analyzed through hard X-rays, thus providing improved contrast [88]. Although phase-contrast imaging can be accomplished with laboratory setups, higher spatial resolution can be achieved with synchrotron X-rays. The technique can be combined with tomography to obtain the 3D distribution of the sample.

Phase-contrast imaging considers X-ray light interactions with matter from a wave perspective treating X-rays as electromagnetic waves. An electromagnetic wave passing through an object interacts with atoms depending on their atomic number. X-rays refractive index can be generally expressed as:

$$n = 1 - \delta + i\beta \quad (1.10)$$

The term  $\delta$  is related to the phase-shift and  $\beta$  to the absorption properties of the medium through the linear attenuation coefficient ( $\mu = 2k\beta$ ). Both  $\delta$  and  $\beta$  are real, positive and small numbers that vary according to the sample electrons density and incident beam energy [89]. For biological samples,  $\delta$  is approximately three-orders magnitude larger than  $\beta$  ( $\delta$  between  $10^{-6} - 10^{-7}$  and  $\beta$  between  $10^{-9} - 10^{-10}$ ) implying that the phase-shift of an hard X-ray beam propagating through a soft-tissue is larger than intensity attenuation [88]. To understand how the presence of an object can affect both amplitude and phase of a wave-field, we assume to have a coherent, monochromatic, point-like source at infinite distance from the sample. We also assume that the beam follows a straight trajectory within the sample (projection approximation) [90]. After the interaction with the object, the incident wave will be modulated as follows:

$$\Psi(x, y) = \Psi_0(x, y)e^{-k \int \beta(x, y, z) dz} e^{-ik \int \delta(x, y, z) dz} = \Psi_0(x, y)e^{i(\Delta\Phi(x, y) - B(x, y))} \quad (1.11)$$

According to equation (1.11), beam amplitude is reduced by a factor dependent on  $\beta$  and phase-shifts are introduced depending on  $\delta$ . When dealing with X-rays imaging, the intensity of the wave-field ( $I(x, y)$ ) is the quantity measured by the detector and it is described by the Lambert-Beer law. Intensity evolutions upon propagation in free space can be described through the transport of intensity equation (TIE) [89]:

$$-k \frac{\partial I(x, y)}{\partial z} = \nabla_{xy} [I(x, y) \nabla_{xy} \phi(x, y, z)] \quad (1.12)$$

In case of an object at distance  $d'$  from the source and a detector at distance  $d$  from the object, the wave propagates in free space over a distance  $d'$  where it gets distorted and propagates again in free space to the detector (Fig. 1.19). The deviation from the original direction of the wave-front is expressed as a position-dependent refractive angle:

$$\alpha(x, y) = \frac{1}{k} \nabla_{xy} \phi(x, y) \quad (1.13)$$

which provides a link between the phase-shift and  $\alpha$ , a detectable quantity. The goal of phase-sensitive techniques is to convert the diffraction angle into intensity modulations in the detector. In the context of this thesis, Projection-Based Imaging (PBI) has been applied to retrieve the phase signal for its simple experimental setup, for the fast acquisition and for the elementary phase-retrieval process. The key features of the technique are the coherence of the source and the presence of a propagation distance between the sample and the detector which is set according to the desired spatial resolution. In principle, waves distorted by the object create interference patterns that appear as white-black lines contouring the sample (edge enhancement). This pattern consists of intensity modulations which are proportional to the phase Laplacian of the waves refracted by the sample. To retrieve the phase information, a method developed by Paganin et al. [91], based on the TIE in paraxial and projection approximation [92], has been applied. The solution elaborated by Paganin to extract the phase information

assumes a single material sample where  $\delta$  and  $\beta$  are constants and the phase is proportional to the thickness of the sample. It describes how X-ray intensity propagates from the object to the detector image and how, by retrieving the process, the captured image can be back propagated to the object plane [88]. The methods described account for the production of a planar image, but, in case of three-dimensional samples, a 3D map of the analyzed object can be derived through X-ray tomography. The main principle of this technique is to expose the sample to the X-ray beam at several angles acquiring projections of the object. Projections are acquired by rotating the sample at different  $\theta$  angles and the spatial distribution of the object is recovered through a Filtered Back-Projection (FBP) algorithm. Introducing Paganin's approach for the reconstruction of the phase-retrieval projections, we assume the object to be homogeneous so that attenuation and phase-shift phenomena are constant through the object and provided as input parameters to the algorithm [88].

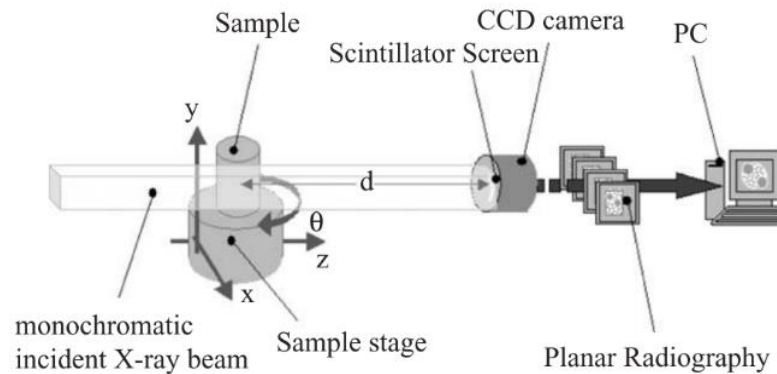


**Figure 1.19** Experimental setup for absorption and phase-sensitive micro-CT at the SYRMEP beamline. (Adopted with permission from [93])

### 1.6.3 X-ray Diffraction (XRD)

In crystals, atoms are arranged into periodic structures. This arrangement is strongly influenced by external factors that can modify and alter crystals' periodic organization. Solid elements can be classified into amorphous, polycrystalline and single-crystal

materials. Amorphous solids have an isotropic atomic arrangement while crystalline materials are anisotropic [94]. In general, X-ray diffraction (XRD) techniques are used to characterize at the atomic level a wide range of materials including minerals, metals, polymers, semiconductors in a non-destructive way.

Crystalline structures are made of arrays of atoms arranged in a repeated pattern. The smallest recurring element of a crystal is called unit cell, and its size and shape can be described three-dimensionally by three axes ( $a$ ,  $b$ ,  $c$ ) having length  $a$ ,  $b$ ,  $c$  and angles between them defined by  $\alpha$ ,  $\beta$ ,  $\gamma$  (Fig. 1.20). Once the unit cell is known, the whole crystal can be reconstructed propagating the unit cell along all directions. According to the length of the axis and angles between them, crystal's elemental structures can be arranged in direct lattices, a mathematical concept introduced by Bravais. To better understand the equations that govern diffraction, the geometrical concept of crystallographic plane is introduced. Crystallographic planes are defined as planes that intersect all lattice points, parallel to each other and equally spaced. The distance between neighboring planes is called interplanar distance ( $d$ ) or d-spacing [94]. Crystallographic planes orientation in space is specified through the Miller indices in the form  $(h k l)$ .

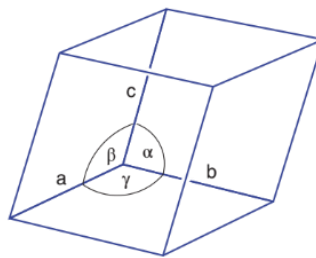


**Figure 1.20** A unit cell of a crystal defined by the parameters  $a$ ,  $b$ ,  $c$ ,  $\alpha$ ,  $\beta$ ,  $\gamma$ . (Adapter with permission from [66])

Another important concept when dealing with crystalline materials is the reciprocal lattice. Reciprocal lattice was introduced by Ewald to better describe diffraction geometry

from a wave-vector point of view. A second lattice, reciprocal to the direct is defined by three elementary translations  $a^*, b^*, c^*$  where  $a^*$  is perpendicular to both  $b$  and  $c$ ,  $b^*$  is perpendicular to both  $a$  and  $c$ ,  $c^*$  is perpendicular to both  $a$  and  $b$ . In terms of interplanar distance,  $d^*$  is perpendicular to the corresponding crystallographic plane and inversely proportional to  $d$  through  $d_{hkl}^* = \frac{1}{d_{hkl}}$ . A 2-D example illustrating the relationship between direct and reciprocal space is shown in Fig. 1.21. Both direct and reciprocal space concepts can be used to understand the geometry of diffraction by a lattice. Direct space is more intuitive whereas reciprocal space is useful for the visualization of diffraction patterns [95].

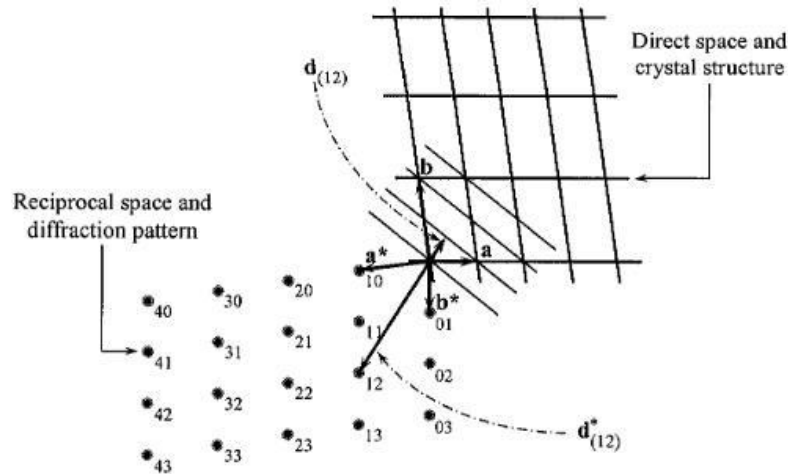


**Figure 1.21** Example of converting crystallographic planes in the direct lattice into points in the reciprocal lattice. The corresponding Miller indices are shown near the points in the reciprocal lattice. (*Adapted from [95]*)

When an X-ray beam pass through a crystal, it gets scattered by the electrons in atoms. If X-rays are considered as electromagnetic waves, the wavefronts can interfere constructively generating a diffraction pattern. This phenomenon was analyzed by Bragg and diffraction from a crystalline sample was exemplified through a mirror-reflection of the incident beam from a series of crystallographic planes. All parallel crystallographic planes are identified by the same triplet of Miller indices  $(h k l)$ , and thus, each plane can

be considered as a scattering object [94]. When an incident wavefront forms incident and reflected  $\theta$  angles with the planes  $(h k l)$  and constructive interference condition is satisfied, diffraction can be described by the Bragg's Law:

$$n\lambda = 2d_{hkl}\sin\theta \quad (1.14)$$

where  $\lambda$  is the X-rays wavelength,  $n$  is the order of reflection,  $d_{hkl}$  is the interplanar distance and  $\theta$  the diffraction angle (Fig. 1.22) [95].

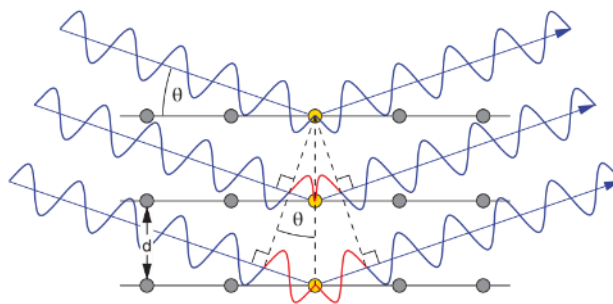


**Figure 1.22** The Bragg law describes interference between rays elastically scattered from successive atomic planes and separated by  $d$ . When the optical path difference (shown here in red) between adjacent rays is an integer multiple  $n$  of the x-ray wavelength, interference is constructive, and a diffraction peak will be seen at that angle. (Adapted with permission from [66])

Ewald introduced a better visualization of the diffraction phenomenon exploiting the concept of reciprocal lattice. Consider an incident wave characterized by the wave vector  $\mathbf{k}_0$ . Upon elastic scattering, the scattered wave is characterized by  $\mathbf{k}_1$  which has the same length as  $\mathbf{k}_0$  (equal to  $\frac{1}{\lambda}$ ) and forms a  $2\theta$  angle with  $\mathbf{k}_0$ . It is now possible to overlap  $\mathbf{k}_0$  and  $\mathbf{k}_1$  with a reciprocal lattice so that the end of  $\mathbf{k}_0$  coincides with the origin of the lattice (Fig. 1.23) [95]. It is important to remember that diffraction occurs only when  $\mathbf{k}_1$  end coincides with a point in the reciprocal lattice. All possible orientations of  $\mathbf{k}_1$  delineate a sphere, called Ewald sphere, whose radius is equal to  $\frac{1}{\lambda}$ . When the sample analyzed is constituted by multiple crystals (in the context of this thesis we provide mineral bone as

an example), the irradiated crystallites have random orientations. Consequently,  $d_{hkl}^*$  are arranged on the surface of the Ewald's sphere in a circle that is perpendicular to  $\mathbf{k}_0$ . The scattered vector  $\mathbf{k}_1$  will be aligned along the surface of a cone as shown in Fig. 1.24. Assuming the number of randomly oriented crystallites approaches infinity, the diffracted intensity will be measured as a ring formed by the cone base and the detector's plane (Fig. 1.24) [95]. Similarly, other independent reciprocal lattice vectors will form rings having different intensity and diameters, also known as Debye rings. Through a radial integration of the diffraction pattern, it is possible to plot the scattered intensity as a function of the Bragg angle (Fig. 1.25 for HA diffraction pattern) or the interplanar distance. In real conditions, diffraction patterns appear as broadened peaks due to both sample and instrumental contributions. In the case of bone apatite, peak broadening represents low crystallinity, lattice distortions and imperfections caused by ion and molecule substitutions, and the small size of the mineral nanocrystals [95].

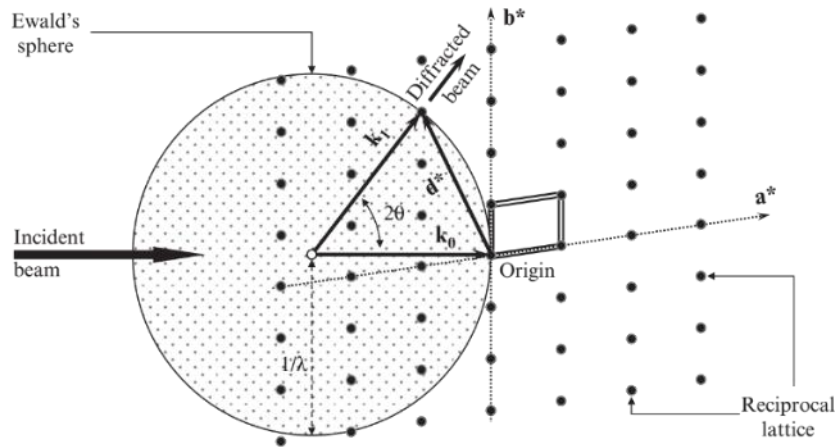


**Figure 1.23** The visualization of diffraction using the Ewald's sphere with radius  $1/\lambda$  and the two-dimensional reciprocal lattice with unit vectors  $a^*$  and  $b^*$ . The reciprocal lattice's origin is on the sphere's surface at the end of  $\mathbf{k}_0$ . Diffraction can only be observed when a reciprocal lattice point, intersects with



the surface of Ewald's sphere. The incident and the diffracted beam wavevectors have a common origin in the center of Ewald's sphere. (Adapted from [95])

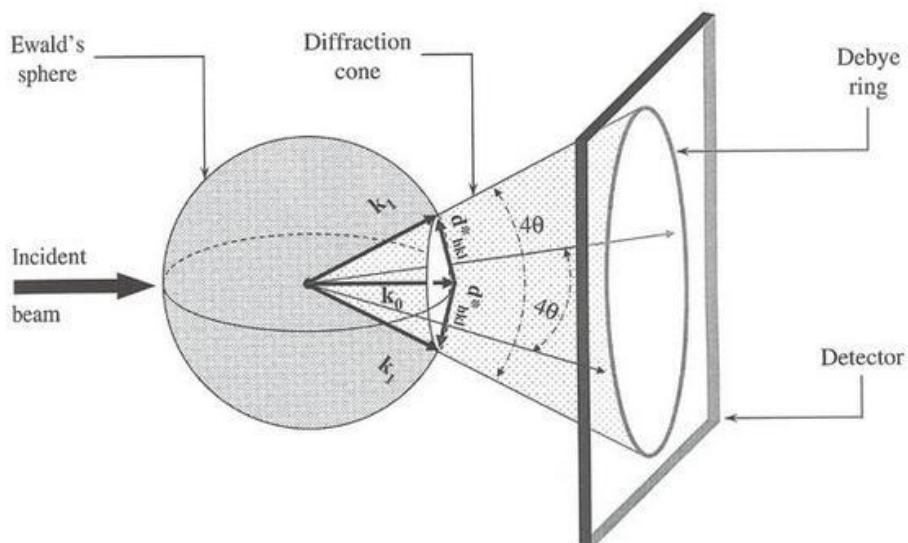


**Figure 1.24** Illustration of how diffraction cones are projected onto a flat detector surface. The projected image of several diffraction cones is a set of concentric rings, or segments of concentric rings if the plate is not large enough. (Adapted from [95])

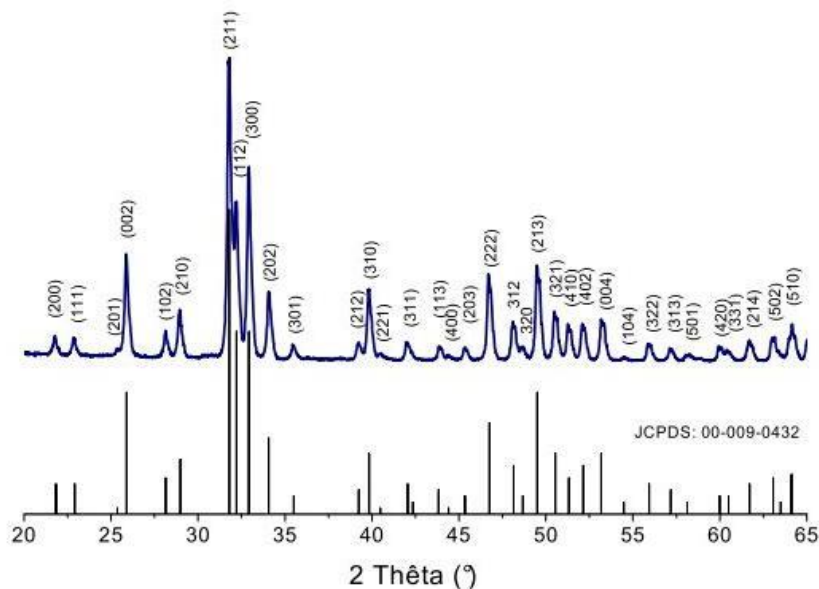


**Figure 1.25** Diffraction pattern of pure hydroxyapatite (JCPDS no. 09-0432) with the corresponding Miller indices ( $\lambda = 0.15406$  nm).

## 1.7 Nuclear Magnetic Resonance

Magnetic resonance imaging (MRI) is a non-invasive imaging technique that performs three-dimensional (3D) imaging of body organs with high spatial resolution. The key advantage of MRI lies in its ability to capture cross-sectional anatomical details of organs, thanks to soft tissue contrast and depth penetration. Moreover, MRI goes beyond anatomical imaging by offering functional insights based on diverse tissue properties, including proton density, temperature, biochemical content, oxygen level, and pH [96]. This versatility of MRI becomes particularly crucial in the study of bone sarcomas, a group of rare tumors originating in bone tissue that require precise and detailed imaging for accurate diagnosis and effective treatment planning. The detailed imaging provided by MRI not only helps in evaluating the extent of tumors invasion into surrounding tissues but also aids in distinguishing between different types of sarcomas and identifying early changes in bone marrow and soft tissues.

### 1.7.1 Principles of Nuclear Magnetic Resonance

Magnetic Resonance Imaging (MRI) is used to detect hydrogen ( $H^+$ ) nuclei within the water molecules of tissues. Protons, subatomic particles with a positive charge, continually rotate along their axis giving rise to a quantum-mechanical property known as spin. Only unpaired protons, found in atoms with an odd number of protons and neutrons, exhibit spin, while atoms with an equal number of protons and neutrons display no overall spin. The spinning motion of an electric charge creates a magnetic field; hence each proton can be considered as a small bar magnet described by a randomly oriented magnetic moment (Fig. 1.26 A). When an external magnetic field ( $B_0$ ) is applied, protons' magnetic moments align either parallel (spin =  $1/2$ ) or antiparallel (spin =  $-1/2$ ) to  $B_0$ . The proton precesses at a speed determined by the Larmor frequency ( $\omega = \gamma B_0$ ), where  $\gamma$  is the gyromagnetic

---

ratio (for proton  $\gamma = 267.56 \times 10^6 \text{ rad/s/T}$ ). If a second alternating magnetic field ( $B_1$ ) is applied orthogonally to  $B_0$ , it is possible to perturb the proton's magnetic moment from the  $B_0$  direction. The alternating magnetic field  $B_1$  is applied through a radio frequency (RF) pulse which must have the same Larmor frequency as the investigated nucleus to induce a transfer of energy to the protons. The rotation angle is dictated by the RF pulse's amplitude and duration (Fig. 1.26 A), and upon cessation, protons return to their equilibrium status through a relaxation process. During relaxation, protons lose energy through two processes: longitudinal relaxation ( $T_1$ ) and transverse relaxation ( $T_2$ ) (Fig. 1.26 B, C).  $T_1$ , or spin-lattice relaxation, involves releasing absorbed energy to surrounding nuclei, increasing vibration within the lattice and resulting in higher thermal energy [96]. Specifically,  $T_1$  relaxation is the time taken by the magnetization moment  $M_z$  to reach 63% of the original position (Fig. 1.26 B, D). In  $T_2$ , or spin-spin relaxation, the adsorbed energy is released by spins because of random mutual interference between each other.  $T_2$  relaxation represents the time for the magnetization moment  $M_{xy}$  to decay to 37% of its initial value (Fig. 1.26 C, E). Pure  $T_2$  decay takes place theoretically only with a completely homogeneous  $B_0$ . However, tissues having different susceptibility properties can affect the homogeneity of the magnetic field and cause spins in different locations within the sample to experience slightly different magnetic fields, leading to dephasing of the transverse magnetization. As a result, the transverse magnetization loses coherence and exhibits a faster decay described by a  $T_2^*$  constant (Fig. 1.26 E). Since tissues have different relaxation properties, images highlighting differences in  $T_1$  ( $T_1$ -weighted image, Fig. 1.26 D) or  $T_2$  ( $T_2$ -weighted image, Fig. 1.26 E) relaxation properties of materials can be generated [97]–[99]. The return to equilibrium of the transverse magnetization constitutes the NMR signal, also known as the Free Induction Decay (FID) signal collected by a receiving antenna. While the  $\vec{B}_0$  field aligns the z axis, the transverse magnetization varies sinusoidally along

the x or y axis due to the magnetization precession around  $\vec{B}_0$  and its amplitude decreases exponentially due to the relaxation phenomenon. Thus, the antenna collects a damped sinusoidal signal.

### 1.7.1.1 Magnetic Resonance Imaging (MRI)

In the biomedical field, magnetic resonance imaging (MRI) is widely employed for distinguishing soft tissues based on proton density and relaxation times. Most in vivo MRI studies utilize protons ( $^1\text{H}$ ) due to their high abundance in biological tissues. In tissues with a significant free water content, such as blood, brain, skeletal muscle, and spinal cord,  $T_2$  and  $T_1$  relaxation times are long and can generate a relatively strong MRI signal [13]. Conversely, tissues with low water content, where protons are confined in a rigid crystal phase, such as bone and teeth, exhibit rapid MRI signal decay, resulting in a dark image lacking discernible structured contrast [100]. In MRI, it is possible to obtain grey-scale medical images with pronounced contrast between different tissues by carefully optimizing acquisition sequence parameters. This optimization involves varying two key parameters: the echo time ( $T_E$ ) and the repetition time ( $T_R$ ). The  $T_E$  corresponds to the time between the center of the first RF pulse and the center of an echo. An echo is generated when two perturbations of the magnetic moment's magnetization are applied and is measured during relaxation. The  $T_R$ , on the other hand, denotes the time between two pulse cycles and is always greater than the echo time. By adjusting the  $T_R$  and  $T_E$ , it is possible to generate either a  $T_1$  or a  $T_2$ -weighted signal. For a  $T_1$ -weighted image, a short  $T_R$  is used to prevent complete recovery of longitudinal magnetization. In contrast, for a  $T_2$ -weighted image, a long  $T_E$  allows complete decay before signal acquisition. Clinical MR protocols include anatomy defining sequences like  $T_1$  and Proton Density (PD), and fluid sensitive sequences such as PD fat-saturated ones.

---

### 1.7.1.2 Magnetic Resonance Spectroscopy (MRS)

MRI faces limitations in providing specific chemical information about the analyzed tissue. Magnetic resonance spectroscopy (MRS) addresses this limitation by enabling the analysis of the chemical composition of tissues and determining the concentrations of specific metabolites *in vivo*. MRS operates on the same principles as MRI, but with a distinct approach: instead of forming an image, the signal is collected to generate a spectrum. The Fourier Transform (FT) is applied to the FID, translating it from the time domain to the frequency domain. Since the NMR signal is constituted by different resonant frequencies, the application of a FT produces a spectrum displaying multiple Lorentzian curves (peaks), each centered at its resonance frequency [99]. The area under each peak correlates with the quantity of metabolites in the studied tissue. The frequency of each peak is expressed relative to a reference signal, and the difference between the reference frequency and the peak frequency is called chemical shift ( $\delta$ ). Chemical shifts are expressed in parts per million to ensure independence from the applied field. High-quality spectra exhibit recognizable peaks corresponding to metabolites, accompanied by reliable measurements of their amplitudes. Achieving such quality necessitates of an intense and homogeneous applied magnetic field. While the first depends on the scanner, the second can be optimized using shim coils to reduce resonance frequency dispersion [101], [102].

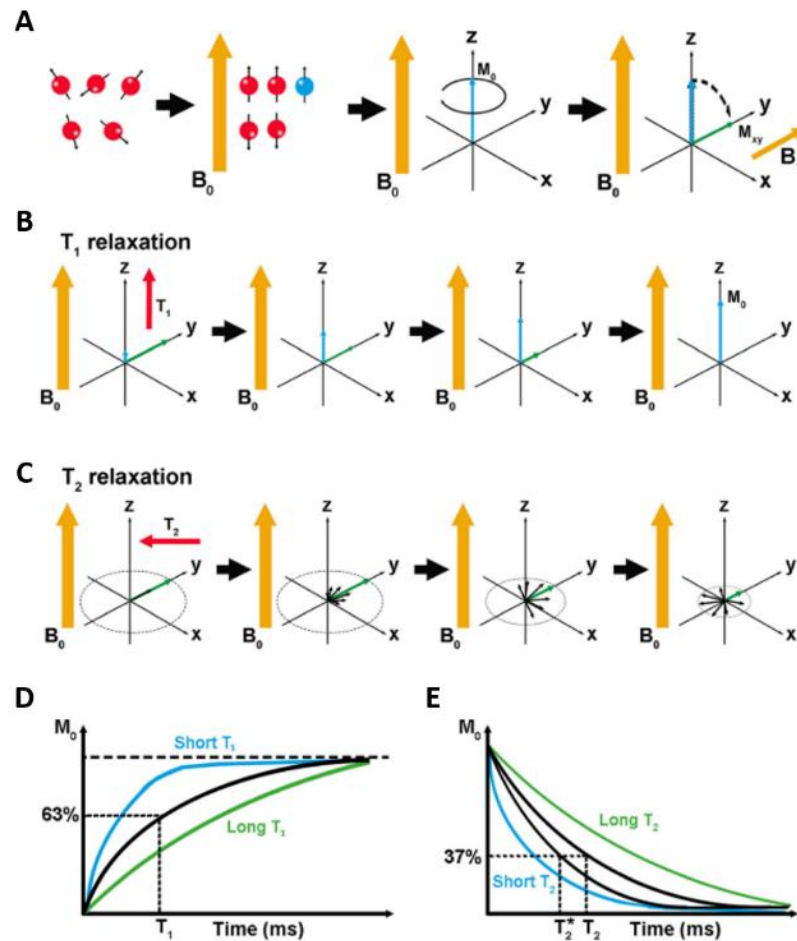


**Figure 1.26** Schematic representation of the basic principles of MRI. A) Protons spin around their axis until an external magnetic field  $B_0$  (orange arrow) is applied inducing protons alignment parallelly (red protons) or antiparallelly (blue protons) and generate a magnetization vector ( $M_0$ , blue arrow). If a second magnetic field ( $B_1$ ) is applied orthogonally to  $B_0$ ,  $M_0$  is tilted along the  $x$ - $y$  direction ( $M_{xy}$  green arrow). When  $B_1$  is switched off,  $M_{xy}$  returns to the equilibrium through two relaxation processes:  $T_1$  and  $T_2$  relaxation (B and C). D)  $T_1$  relaxation is defined as the time necessary to achieve 63% of the original longitudinal magnetization. E)  $T_2$  relaxation is defined as the time needed to dephase up to 37% of the original magnetization. (Adapted with permission from [96])

### 1.7.1.3 Ultra-High Field nuclear magnetic resonance (UHF NMR)

The approval of ultra-high field (7T) magnetic resonance scanners for clinical use by the US Food and Drug Administration (FDA) and the European regulatory authority,

---

and the consequent release of clinical UHF scanner, have triggered the setup and adaptation of NMR sequences for UHF applications [103]. At the moment, the majority of the clinical MR systems are 1.5 and 3T systems, but 7T UHF scanner for clinical research are getting more and more employed in hospitals and academic centers [104]. UHF 7T scanners provide unique advantages with respect to lower field strength scanners, but some technical and safety challenges need to be addressed.

The increase of the main field strength,  $B_0$ , to 7T presents several advantages:

- increment of the magnetization  $M_0$ ;
- the signal-to-noise ratio (SNR) scales with the square of  $B_0$  allowing to increase spatial and temporal resolution, or reduce scan time;
- the enhancing of contrast-to-noise ratio (CNR) is relevant for functional MRI, and quantitative susceptibility mapping (QSM);
- spectral resolution gets improved at UHF, and allows better identification of the different metabolites;
- applications to different nuclei including  $^{23}\text{Na}$ ,  $^{31}\text{P}$ ,  $^{17}\text{O}$  and  $^{13}\text{C}$ .

UHF systems also presents unique technical challenges. The  $B_1$  field required scales quadratically with  $B_0$  field strength affecting a key safety measure of tissue heating called specific absorption rate (SAR) [105]. The RF wavelength in tissues reduces from  $\sim 35\text{cm}$  to  $\sim 15\text{cm}$  from 3T to 7T, decreasing tissue penetrability. Additionally, the use of body coils for transmitting RF pulses becomes impractical at 7T, thus RF transmit phase arrays are employed, making it difficult to image large areas. Furthermore, there are significant variation in receive  $B_1$  inhomogeneity, requiring accurate flip angle selection and additional sensitivity maps. Finally, at higher fields,  $T_1$  values increase, and  $T_2$ ,  $T_2^*$  values decrease due to the enhancement of susceptibility [106].

From this introduction we clearly understand that, despite the advantages introduced by the increased field strength, the use of UHF should depend on the target. Some applications provide more information than lower powered scanners, while others may not benefit from UHF system due to the demanding technical challenging they present.

### **1.7.2 Imaging of bone sarcoma**

Among bone sarcomas, osteosarcoma is the most common malignant bone tumor with chondrosarcoma and Ewing sarcoma following in incidence [107]. The evaluation of bone tumors often requires the use of multiple imaging modalities, encompassing radiography, bone scintigraphy, CT, MRI, and PET (Positron Emission Tomography). Imaging, conducted prior to any intervention, plays a crucial role in the diagnosis, staging, restaging, monitoring response to treatment, and surveillance for recurrence. Due to the large variety of sarcoma subtypes and consequently diverse tumors features and treatment plans, there is no singular diagnostic pathway corresponding to a specific imaging study [108]. Conventional radiography is usually the first step in the diagnostic process, representing an essential tool for assessing the lesion's site and edges, bone matrix mineralization, cortical involvement, and periosteal reaction. It remains the cornerstone for differential diagnosis of skeletal tumors and tumor-like lesions [108]. Classical radiological signs related to malignancy include “sunburst periosteal reaction”, “onion skin periosteal reaction” and “Codman triangle” (Fig. 1.27) [109]. On the other hand, CT proves particularly valuable when lesions are situated in anatomically intricate areas like the spine or pelvis, offering visualization of fine bony details and small calcifications.



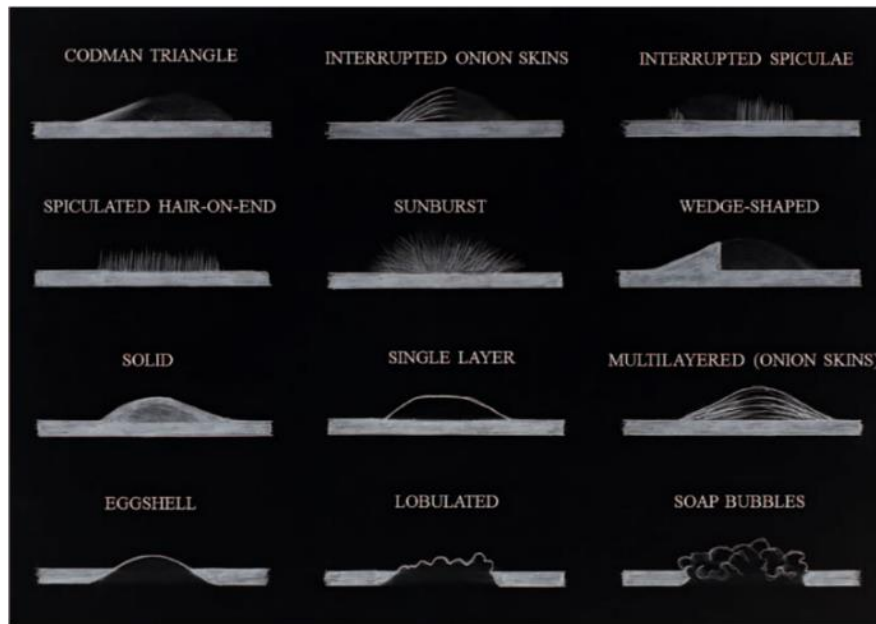


**Figure 1.27** Patterns of periosteal reaction. Continuous periosteal reaction: eggshell, lobulated, soap bubbles, solid, single layer, multilayered, spiculated, sunburst; interrupted periosteal reaction: wedge-shaped, Codman triangle, interrupted onion skin, interrupted spicule. (*Adapted with permission from [109]*)

Over the past few decades, MRI has emerged as the key element of musculoskeletal (MSK) radiology, owing to its non-invasive capacity to assess soft tissue, bone, and articular structures [107]. Particularly renowned for its effectiveness in local staging of bone tumors, MRI stands out for its precise characterization of musculoskeletal lesions, offering insights into their composition, extent, bone marrow infiltration, and involvement of adjacent soft tissues [108]. It is particularly useful for planning optimal biopsy sites, determining the type of surgical resection, and evaluating responses to chemotherapy. MRI's capability to generate images without exposing the patient to ionizing radiation sets it apart from other imaging techniques commonly used in bone sarcoma diagnosis, such as CT scans. This non-invasive nature makes MRI an ideal choice for repeated examinations, crucial when monitoring the progression of the disease and the response to treatment over time.

Conventional MR imaging primarily relies on the qualitative interpretation of variations in the  $T_1$  and  $T_2$  relaxation properties of both normal and pathological tissue. Despite its effectiveness, there exists a notable challenge in distinguishing between neoplasms (both benign and malignant) and non-neoplastic reactive or inflammatory lesions, due to overlaps in their signal characteristics [110]. Differentiating hyperintense tumor signals from reactive peritumoral edema using fluid-sensitive sequences can be challenging (2) as they exhibit similar imaging features. In the following, the conventional MR imaging techniques used in this study are described.

### 1.7.2.1 Proton Density (PD) and Proton Density Fat-Saturation (PDFS)

Proton density (PD) weighted images are related to the number of nuclei in the area being imaged (number of hydrogen protons) and show contribution of both  $T_1$  and  $T_2$  signal. To optimize signal distinction, PD-weighted sequences utilize a long repetition time ( $T_R$ ) of 2000+ milliseconds and a short echo time ( $T_E$ ) around 20 milliseconds, minimizing differences in  $T_1$  and  $T_2$ . This sequence proves particularly effective in joint assessment, offering excellent signal differentiation between fluid, hyaline cartilage, and fibrocartilage. The dominant signal intensities for different tissues in PD-weighted images are as follows:

- fluid: high signal intensity (white);
- muscle: intermediate signal intensity (grey);
- fat: high signal intensity (white);
- hyaline cartilage: intermediate signal intensity (grey);
- fibrocartilage: low signal intensity (black).

Various pathological conditions can display distinct appearances in PD MRI images due to differences in tissue composition, water content, and proton density. Here are some examples of how different pathologies might manifest on PD images:

- 
- edema: characterized by increased fluid accumulation in tissues, exhibits brighter appearances that can indicate inflammation or tissue injury;
  - cysts: bright or light grey areas, owing to their fluid content;
  - tumors: tumors with a substantial cellular component might appear with intermediate signal intensity, while areas of necrosis or hemorrhage might present differently;
  - inflammatory conditions: characterized by bright signal intensities due to augmented water content and altered tissue properties;
  - bone marrow changes: marrow infiltration due to cancer, might impact proton density and water content, resulting in signal intensity alterations.

On the other hand, the Proton Density fat-saturated (PDFS) MRI sequence serves as a specialized imaging technique designed to enhance contrast and visualization of non-fatty soft tissues. By selectively suppressing fat signals, this sequence improves visibility for edema, injuries, and pathologies in ligaments, bones, cartilage, and muscles. PD fat-saturated sequences are particularly advantageous in musculoskeletal imaging, where the presence of fat can often obscure subtle findings.

The dominant signal intensities for different tissues in PD fat-saturated sequences are:

- muscle: intermediate signal intensity (grey);
- bone marrow: intermediate to low signal intensity;
- blood vessels: low signal intensity;
- fat: low signal intensity;
- ligaments: intermediate to low signal intensity;
- nerve Roots: intermediate signal intensity (grey);
- cartilage: intermediate to low signal intensity;
- fluid: high signal intensity (white);

- tendons: intermediate to low signal intensity.

According to the pathology, lesions appear differently on PD fat-saturated scans:

- bone marrow edema and contusions commonly seen after trauma or in inflammatory conditions, show increased signal intensity;
- muscle injuries: strains or tears can be identified as areas of increased signal;
- tumors: highly cellular or vascular tumors show increased signal, while those with high fibrous content appear darker.

In conjunction with conventional MRI sequences, advanced MRI techniques including diffusion-weighted imaging (DWI) and MR spectroscopy (MRS) are being explored for sarcoma imaging as they provide crucial information about tumor cellularity and metabolism [107].

### **1.7.2.2 Diffusion-Weighted Imaging (DWI)**

Diffusion-weighted (DW) imaging stands as a non-enhanced functional MR imaging technique that captures differences in the Brownian motion of water molecules caused by variations in tissue microstructure [110], [111]. Tissues with increased cellularity and a resultant increased amount of cell membranes lead to decreased Brownian motion or restricted diffusion, while tissues with decreased cellularity tend to have unrestricted or increased diffusion. As such, cellular or malignant masses typically exhibit restricted diffusion, resulting in a hyperintense DWI signal [112]. Through a visual assessment of restricted diffusion, DW imaging provides quantitative functional evaluation of tissue cellularity at the molecular level and holds great potential in differentiating between benign and malignant lesions, as well as improving the MR imaging evaluation of treatment response [110], [113] and tumoral boundaries individuation [114]. Specific benefits of DW imaging include a short scanning time and the absence of a requirement for intravenous contrast material, making it easily integrable into routine imaging

protocols. DWI commonly employs a single-shot diffusion-weighted spin echo (SE) echo planar imaging (EPI) pulse sequence. Diffusion sensitizing is achieved through diffusion gradients causing signal attenuation, and the resulting signal intensity is related to the apparent diffusion coefficient (ADC) [ $\text{mm}^2/\text{s}$ ] by the formula in Eq. (1.15):

$$S_b = S_0 e^{-bADC} \quad (1.15)$$

where  $S_b$  is the diffusion-weighted signal and  $S_0$  the non-weighted signal,  $b$  is the b-value, which is the amount of diffusion weighting and depends on the gradient strength  $G$  and gradient timing [115]. DWI can be extended by measuring the ADC in at least six independent directions to quantify the directional anisotropy of the diffusion. Instead of a scalar ADC parameter, the diffusivity can be described by a 3x3 tensor  $D$  which is diagonalized by an eigenvector and eigenvalue analysis where the principal eigenvector yields the direction with the highest diffusion (quantified by the eigenvalues). However, it is rather hard to interpret quantitative changes in the diffusivity and diffusion anisotropy directly from the diffusion tensor itself. Therefore, several scalar indices which can be quantitatively compared between measurements and subjects were introduced [115]. Among them, the mean diffusivity (MD) or ADC, given in Eq. (1.16), describes the average direction of the diffusion in the tissue:

$$ADC = \frac{(\lambda_1 + \lambda_2 + \lambda_3)}{3} \quad (1.16)$$

The apparent diffusion coefficient (ADC) is a quantitative measure of Brownian motion, with low values reflecting highly cellular microenvironments and high values observed in acellular regions that allow free diffusion of water molecules [110]. There are different methods to measure ADC values. ADC is usually derived by drawing a region of interest (ROI) in the most homogeneous area of the tumor. Minimal ADC value ( $ADC_{min}$ ), mean ADC value ( $ADC_{mean}$ ) and maximal ADC value ( $ADC_{max}$ ) can be easily derived.  $ADC_{min}$  represents the most cellular component of the tumor [109].  $ADC_{mean}$  and  $ADC_{max}$

include non-viable necrotic and cystic portions of the tumor.  $ADC_{mean}$  represents the mean tissue composition and has been correlated with proliferation of the tumor, while  $ADC_{max}$  has been associated with low cellular component of the tumor [116].

These parameters have been used to classify musculoskeletal tumors subtypes in both soft tissue and bone [113]. In soft tissues, masses composed of fluid exhibit high ADC values because of free water motion. In bone, ADC values in hypercellular and malignant lesions show higher signal with respect to fatty marrow [110]. A possible explanation is that yellow marrow has reduced water content with little extracellular matrix, and that the larger lipid-laden cells in yellow marrow may restrict water movement to a greater degree than the smaller hematopoietic cells of red marrow. Fat itself, being hydrophobic, may act more than as a physical barrier to diffusion and function as a repellent. Thus, osseous tumors manifest as areas of high restricted diffusion against a background of low ADC signal in bone [110]. Because cellular changes are expected to manifest prior to morphological variations, DW imaging holds potential in detecting treatment response earlier than conventional imaging. ADC maps can provide quantitative information regarding therapy response by delineating regions of tumor necrosis (increased diffusivity) reflecting successful treatment. A study by Hayashida et al. [116] on 18 patients with bone sarcoma and Ewing sarcoma revealed changes in ADC values, and no changes in tumor volume or morphology, in tumoral regions showing good response to neoadjuvant chemotherapy.

### **1.7.2.3 Proton Magnetic Resonance Spectroscopy ( $^1\text{H}$ -MRS)**

While conventional MRI plays a pivotal role in the assessment of musculoskeletal lesions, it lacks specificity for accurate differentiation of malignant from benign diseases [101]. MRS has emerged as a noninvasive method for probing tumoral metabolism within the musculoskeletal system [102], [117]. In the context of MSK tumors, where benign

---

lesions outnumber malignant masses, noninvasively discriminating benign and malignant masses may obviate biopsy [118] or improve the targeting of the most suspicious portion of a lesion [101]. In addition,  $^1\text{H}$ -MRS stands out as an innovative tool for preoperative lesion characterization and, potentially, for post-treatment assessment and postsurgical tissue evaluation.

Recently, MRS research on musculoskeletal tumors has focused on the increase of choline levels in malignant bone and soft-tissue tumors [102], [119]–[123]. Choline has already been used as a marker of malignancy in several organ systems, including brain [124], breast [125], prostate, and liver [126], [127]. The biological rationale behind choline levels increase has been shown in *in vitro* studies demonstrating that uncontrolled cell proliferation induces changes in the concentration of choline-containing compounds [128], detected in  $^1\text{H}$ -MRS spectra as a discrete total choline peak at 3.2 ppm (Fig. 1.28 A). The choline peak contains contributions from glycerol-phosphocholine, phosphocholine, and free choline, all involved in the phospholipid metabolism of cell membranes (Fig. 1.28 B). The elevated choline concentration in tumors can be attributed to the accumulation of phosphocholine resulting from increased expression and activity of choline kinase and phospholipase. Besides malignant transformation, hypoxia and pH changes in the tumor microenvironment can activate cell signaling pathways leading to increased choline concentration [129]. Choline concentration is likely to increase along with membrane synthesis due cellular proliferation, a feature which is characteristic of malignancy. Notably, the choline peak at 3.2 ppm lies in proximity to the creatine peak at 3.0 ppm (Fig. 1.28 A). As both metabolites are abundant in normal muscle, it is fundamental to carefully place the voxel for spectroscopy within the tumor to avoid contaminant signals from the surrounding tissues [102].

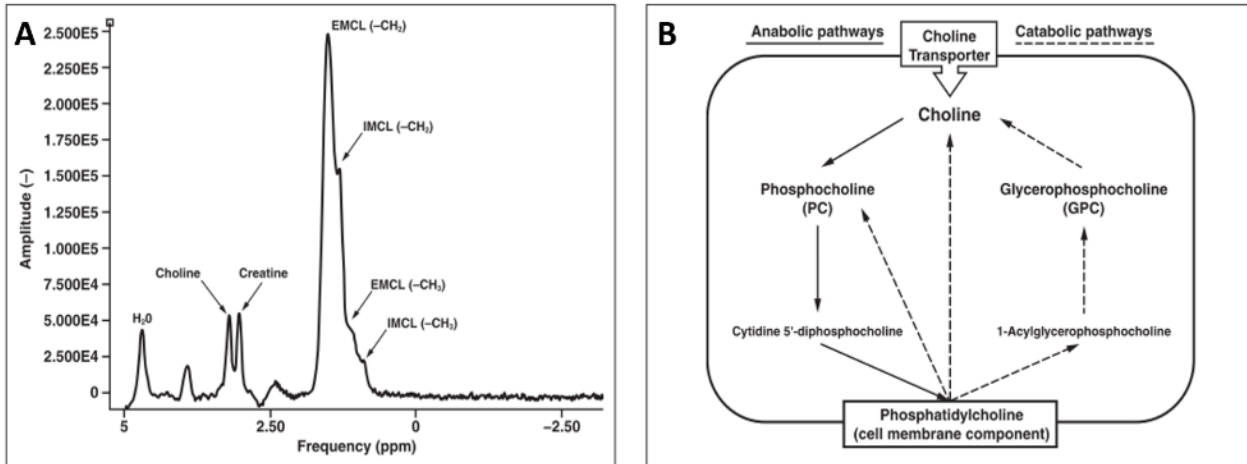


**Figure 1.28** A) Typical MR spectrum of normal muscle: water, choline, creatine, and intramyocellular (IMCL) and extramyocellular (EMCL) lipids. The Choline peak is approximately centered at 3.2 ppm. B) Diagram showing the pathways involved in choline metabolism. Elevated choline concentration in tumors is believed to be primarily due to accumulation of phosphocholine resulting from increases in activity of choline kinase and phospholipase. (*Adapted with permission from [101]*)

The presence of choline in tumoral masses holds promise as a discriminant between benign and malignant lesions, acknowledging that some benign lesions may exhibit choline presence, as observed by Wang et al. [123]. While qualitative assessment of choline peak presence or relative quantification based on SNR is common, a more robust quantification method is preferable [119], [120]. Fayad et al. [102], have translated to musculoskeletal lesions a method previously described and tested for breast cancer [130] which allows for an estimation of Cho concentration in units of *mmol/kg*. Quantitative measurements of Cho content are needed for added specificity in the distinction of benign and malignant disease, to characterize tumor subtype, understand grade and prognosis of malignant lesions, help treatment plan selection and monitor its efficacy along time [102]. Fayad et al. [119] identified a significant difference in choline's concentration between histologically proven areas of malignancy and nonmalignant tissue. They further noted a correlation



---

between choline content and tumor histologic grade [120] underscoring the potential of presurgical  $^1\text{H}$ -MRS in guiding biopsies toward the most suspiciously aggressive areas of the tumor. Furthermore, a recent study by Hieh et al. [131] highlighted  $^1\text{H}$ -MRS potential in the assessment of treatment prognosis. They observed a correlation between tumor size reduction and choline concentration decrease through the early detection of changes in choline content in malignant lesions. Currently,  $T_2$ -weighted imaging stands as the gold standard in detecting recurrent or residual tumors during postoperative disease studies, being  $T_2$  signal intensity absence the criterion for excluding recurrent disease. However, this technique encounters a limitation due to  $T_2$  signal hyperintensity caused by reconstructive myocutaneous flaps, lasting for 6-12 months or more, restricting its application until the patient develops a mature postsurgical scar. In this context, postoperative proton MRS emerges as a potentially useful tool in the early detection of recurrence.

## 1.8 Aim of the work

Osteosarcoma, and bone sarcomas in general, are rare diseases predominantly affecting young children and adolescents. Despite recent advances in oncology, the etiology of such tumors hasn't been fully elucidated yet. Furthermore, each subtype of this cancer exhibits unique clinical and pathological features, posing challenges in accurate non-invasive diagnosis and tailored treatment strategies development. The principal objective of this thesis is to comprehensively characterize osteosarcoma employing a multimodal approach that spans different length scales. Starting at the cellular level, the early steps of bone mineralization will be investigated in SaOS-2 cells induced to differentiate to osteoblasts, providing new insights on osteosarcoma genesis and progression. At tissue level, the ex vivo study of bone biopsies will be focused on giving new knowledge on osteosarcoma tissue

architecture, structure and composition, elucidating the complexity of tumor micro-environment. Through advanced nuclear magnetic resonance techniques, a non-invasive approach will be proposed for both sarcomas' diagnosis and treatment monitoring. Finally, this thesis aims at providing new insights that may pave the way for optimized diagnosis and innovative therapeutic strategies, exploiting advanced synchrotron X-ray as well as magnetic resonance techniques.

# Chapter 2: Biomineralization in Osteosarcoma cells

OS is the most common primary malignant bone tumor and its etiology has been recently associated with osteogenic differentiation dysfunctions. OS cells keep a capacity for uncontrolled proliferation showing a phenotype similar to undifferentiated osteoprogenitors with abnormal biomineralization. Within this context, both conventional and X-ray synchrotron-based techniques have been exploited to deeply characterize the genesis and evolution of mineral depositions in SaOS-2 cells exposed to an osteogenic cocktail for 4 and 10 days. A partial restoration of the physiological biomineralization, culminating with the formation of hydroxyapatite, was observed at 10 days after treatment together with a mitochondria-driven mechanism for calcium transportation within the cell. Interestingly, during differentiation, mitochondria showed a change in morphology from elongated to rounded, suggesting a metabolic reprogramming of OS cells possibly linked to an increase in glycolysis contribution to energy metabolism. These findings add a dowel to the genesis of OS giving new insights on the development of therapeutic strategies, to restore the physiological mineralization in OS cells.

## 2.1 Materials and Methods

### 2.1.1 SaOS-2 cells culture and osteogenic induction

Human osteosarcoma cell line SaOS-2 was purchased from American Type Culture Collection (ATCC, Manassas, VA, USA). Cells were grown in RPMI 1640, supplemented with 10% heat inactivated Fetal Bovine Serum (FBS), 2 mM glutamine, 1000 units/mL penicillin and 1 mg/mL streptomycin, at 37 °C in a 5% CO<sub>2</sub> 95% air humidified atmosphere. After 24 h from seeding, cells were treated with vehicle or osteogenic differentiation cocktail containing 20 nM 1,25-Dihydroxyvitamin D<sub>3</sub>, 50 μM L-Ascorbic acid 2-phosphate and 10 mM glycerol phosphate, replacing the media every 48 h.

### 2.1.2 Alizarin Red staining

SaOS-2 cells were seeded at  $1 \times 10^4/cm^2$  and treated with an osteogenic cocktail after 24 h. Furthermore, 2% alizarin red S was dissolved in distilled water and the pH was adjusted to 4.1–4.3 using 0.5% ammonium hydroxide. Cultures were fixed with cold EtOH 70% for 30 min at room temperature, washed and stained with alizarin red S solution for 30 min. After removal of unincorporated excess dye with distilled water, the mineralized nodules were labelled as red spots.

### 2.1.3 Alkaline Phosphatase activity assay

After 7 days of treatment, the cells were freshly harvested, washed twice in ice-cold phosphate buffered saline (PBS) and centrifuged at 3000 rpm for 5 min. For the treated samples, a cell scraper was used to detach cells and collect them into ice-cold PBS before pelleting via centrifugation. Cells were lysed in ice by a 1 mL solution of 40 mmol/L HEPES, 110 mmol/L NaCl, 0.25% deoxycholate and 1 mg/mL aprotinin,

---

pH 7.4. The homogenate was used for the ALP spectrophotometric assay by using p-nitrophenyl phosphate as a substrate. ALP activity was normalized for the protein content. Proteins were measured by the Bradford method using Bio-Rad protein assay. One unit of ALP activity is defined as the amount of protein capable of transforming 1 mmol of substrate in 1 min at 25 °C. Statistical analysis was performed using GraphPad Prism 8 software using a t-test and differences were deemed significant for \*  $p < 0.05$ .

#### **2.1.4 Gene expression analysis**

Total RNA from cells was collected after 7 days of osteogenic induction and extracted using the NucleoSpin RNA kit (Macherey Nagel, Düren, Germany) following the manufacturer's instructions. The level of expression of the osteogenic markers runt-related transcription factor 2 (RUNX2), collagen type I (COL1A1), osteocalcin (BGLAP), osteopontin (SPP1) and osteonectin (SPARC) was analyzed by quantitative real-time PCR (qPCR), as previously reported [32]. Glyceraldehyde 3-phosphate dehydrogenase (GAPDH) and hypoxanthine phosphoribosyltransferase 1 (HPRT1) were used as housekeeping reference genes ( $2^{-\Delta\Delta CT}$  method). Primer sequences are reported in Table 2.1. Fold changes from untreated control cells were calculated. Data analysis was performed using CFX Manager Software (Bio-Rad), creating a gene study that uses an internal calibrator to normalize the variability between the experiments. Data are reported as mean value  $\pm$  SEM of at least three independent biological replicates. Statistical analysis was performed using GraphPad Prism 6 software using a two-way ANOVA followed by a Sidak's multiple comparison test. p values less than 0.05 were accepted as significant.

Gene		Sequence 5'-3'
GAPDH	F	ACAGTTGCCATGTAGACC
	R	TTGAGCACAGGGTACTTTA
HPRT1	F	ATAAGCCAGACTTTGTTGG
	R	ATAGGACTCCAGATGTTTCC
RUNX2	F	AAGCTTGATGACTCTAAACC
	R	TCTGTAATCTGACTCTGTCC
ALPL	F	TCTTCACATTTGGTGGATAG
	R	ATGGAGATATTCTCTCGTTC
SPARC	F	AGTATGTGTAACAGGAGGAC
	R	AATGTTGCTAGTGTGATTGG
COL1A1	F	CCAGCAAATGTTCTTTTTG
	R	AAAATTCACAAGTCCCATC
BGLAP	F	TTCTTTCCTTCCCTTG
	R	CCTCTTCTTGAGTTTATTGG
SPP1	F	GACCAAGGAAACTCACTAC
	R	CTGTTAACTGGTATGGCAC

**Table 2.1** Primer sequences used for qPCR.

### 2.1.5 X-ray absorption near-edge spectro-microscopy (XANES) and cryo-Soft X-ray tomography (cro-SXT)

*Sample preparation.* SaOS-2 cells were seeded onto gold QUANTIFOIL R 2/2 holey carbon-film microscopy grids. The cells were plated at a concentration of  $2 \times 10^4$  cell/cm<sup>2</sup> on the grids previously sterilized by UV light for 3 h. After 4 and 10 days from osteogenic induction, the attachment and spreading of the cells was carefully verified using visible light microscopy prior to freezing. Immediately prior to freezing, 1.5  $\mu$ L of 100 nm gold fiducial aliquot (chemical reference: gold

---

nanoparticles 100 *nm*, EMGC100, BBI Group, Cardiff, UK) was added to the grids, necessary as external marker for the alignment needed for tomographic reconstruction. The grids were frozen hydrated by rapid plunge freezing in a liquid ethane pool cooled with liquid nitrogen using a GP-Leica Microsystems Excess. Before plunge freezing, water is removed via blotting. The quality of the sample's preparation was checked in cryo-conditions prior to loading into the microscope chamber. After plunge freezing, cryogenic temperature ( $\sim 110$  K) is maintained until and during the measurements. Calcite (Sigma-Aldrich), HA and  $Ca_3(PO_4)_2$  (Bio Eco Active S.R.L, Bologna, Italy) references were prepared by crushing powders in a mortar, and the obtained dust was laid down on a Quantifoil Au TEM grid [40].

*Data acquisition.* Cryo-SXT and cryo-XANES images were recorded at the Mistral beamline of the ALBA Synchrotron. Scanning the X-ray energy through the Ca  $L_{3,2}$  – *edge*, cryo-XANES can be used to determine the Ca bulk chemical state [132]. Two-dimensional Ca  $L_{3,2}$  – *edge* XANES images (12 s exposure time) were collected on selected areas using an effective pixel size of 13 nm and with a variable energy step (0.5 eV of pre-edge and post-edge, 0.1 elsewhere). The total acquisition time was about 1.5 h per energy scan, including the flat field acquisition at each energy step.

*Data processing.* The transmitted intensity at each energy value was normalized to unity dividing by the corresponding flat field image, i.e., the incident intensity on the sample, considering the value of the electron current in the storage ring. Then, all the transmission images were aligned with respect to the first image, applying the x–y shifts, which maximize the cross-correlation between the same selected ROI in the two images [63]. These shifts were calculated using the Python library of cv2 “Open Computer Vision” (the used function is “cv2.matchTemplate()”). Usually, this

operation reduces the effective dimension of the field of view by 10 to 15%. Finally, the absorbance for each pixel can be calculated from the measured transmission as:

$$A = \mu t = -\ln \frac{I}{I_0} \quad (2.1)$$

and can be related as a function of the energy to the linear absorption coefficient using the Lambert-Beer law:

$$T(x, y) = \frac{I(x, y)}{I_0(x, y)} = e^{(-\int \mu_l(x, y, E) dt)} = e^{(-\int \mu_m(x, y, E) \rho dt_m)} \quad (2.2)$$

where  $t$  is the thickness,  $\mu_l$  is the linear absorption coefficient of the material, and  $\mu_m$  is the mass absorption coefficient.

Spectra were extracted only from pixels that satisfied the following signal to noise criteria:

$$\Delta\mu_l t = [\mu_l(349.2\text{eV}) - \mu_l(342\text{eV})]t > 2N \quad (2.3)$$

with  $\mu_l$  as the linear absorption coefficient,  $t$  as the thickness, and  $N$  as the noise defined as the absorbance standard deviation in the pre-edge energy region (341–343.5 eV).

The pixel selection operation was performed using a homemade function created in Matlab. Peak fitting was performed to compare the measured spectra and to estimate the height and area of  $L_2$  and  $L_3$ . To eliminate the contribution of lower energy absorption, the absorbance values in the pre-edge energy region were linearly fitted using the Matlab function “polyfit”, and the corresponding best fitting straight line was subtracted on the full energy range. Then, to eliminate the edge step arising from atomic transitions to the continuous, a double *arctan* function was also subtracted, following the procedure described in [133]. In this case, the Matlab function “CreateFit” was used. The used double *arctan* function was:



$$\frac{h_1}{\pi} \left\{ \text{atan} \left[ \frac{\pi}{\omega_1} (E - E_1) \right] + \frac{\pi}{2} \right\} + \frac{h_2}{\pi} \left\{ \text{atan} \left[ \frac{\pi}{\omega_2} (E - E_2) \right] + \frac{\pi}{2} \right\} + C \quad (2.4)$$

with  $w_1 = w_2 = 0.2 \text{ eV}$ ,  $E_1 = L_2\text{peakmax}$ , and  $E_2 = L_2\text{peakmax} + 3 \text{ eV}$ . The other parameters ( $h_1$ ,  $h_2$ , and  $C$ ) were fitted with the data points in the pre-edge and in the post-edge (355.8–360 eV) energy regions.

Afterwards, all the peaks present in each spectrum were fitted by Gaussians (the chosen number of Gaussians corresponds to the number of peaks), creating a fitting model in Larch software [134]. An example of fitting results for a calcite spectrum is reported in Fig. 2.1.

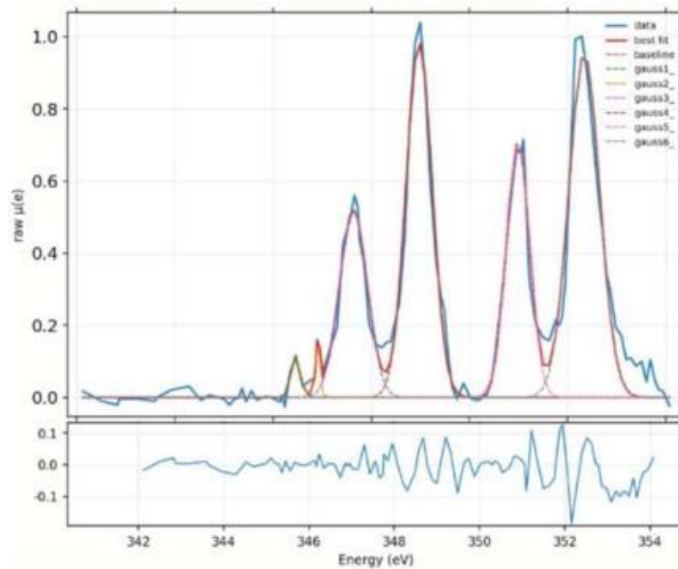


**Figure 2.1** Gaussian peaks fit shown for a typical measured calcite spectrum. The number of fitted peaks is six and they have similar FWHM. The residual, calculated simply as the difference between the fit and the experimental data, is also reported in the inset below the fit.

Cryo-SXT was carried out at 352.9 eV to optimize the contrast between the calcium- and carbon-rich structures and the surrounding water-rich cytoplasmic solution. For each cell, a tilt series was acquired using an angular step of  $1^\circ$  on a  $110^\circ$  angular range with effective pixel size equal to 13 nm at 352.9 eV. Each image of the

---

tilt series was normalized using flat-field images of 1 s acquisition time. The tilt series were manually aligned using eTomo in the IMOD tomography software suite [135] using Au fiducials of 100 *nm*. The aligned tilt series were reconstructed using TOMO3D software, using the SIRT algorithm (30 iterations), and then segmented by Amira (Thermo Fisher Scientific, Waltham, MA, USA).

### **2.1.6 Principal Components Analysis (PCA) on nano-XANES Ca $L_{3,2}$ –edge spectra**

PCA is one of the most efficient and common tools for multivariate data exploration and reduction. By representing the system through a new uncorrelated set of orthogonal variables obtained as linear combinations of the original variables and called PCs, PCA captures the original data variance and reveals similarity, groupings and trend patterns, that may characterize the objects (spectra), according to their similarities in chemical properties. The new coordinates of the objects are called scores, while the loadings represent the importance of each original variable in defining each PC direction. Score and loading values can be represented on bidimensional scatter plots (score and loading plots, respectively), which allow visualization of the similarities between the objects and the inter-correlation among original variables.

PCA was initially applied on a matrix containing standard spectra (3 spectra of standard calcium phosphate and 22 spectra of standard hydroxyapatite). Afterward, PCA was applied to the matrix of the spectra of the real samples obtained from the Ca-depositions at four days and at ten days for a total of 67 spectra (objects). In both cases, all 85 energies available considered in the XANES spectra collected were considered as variables.

---

Prior to PCA analysis, the row spectra were mathematically pre-treated to minimize the unwanted physical effects and noise. The pre-treatment step flow, applied equally to the standard and real samples spectra, consisted of (1) spectral range selection of the main calcium features; (2) range scaling (RS), where the pre-peak and peak regions were scaled with the formula used by Sciutto et al. [136], to have a comparable variability range along the y-axis (intensity); (3) Savitzky–Golay first derivative and (4) column centring.

### 2.1.7 Nano X-ray Fluorescence Microscopy (nano-XRFM)

X-rays fluorescence measurements were performed at the ID16A Nano-Imaging beamline of the European Synchrotron Radiation Facility (ESRF, France). The beamline provides a high-brilliance beam focused down to nanometer size, allowing quantitative 3D characterization of the morphology and the elemental composition of specimens in their native state by combining coherent imaging techniques and X-ray fluorescence microscopy. The 185 m long beamline provides nano-focused beams for analytical imaging addressing problems in biology, biomedicine and nanotechnology using X-ray fluorescence microscopy and nano-tomography. It is optimized for ultimate hard X-ray focusing of a beam with a large energy bandwidth at specific energies (17 keV or 33.6 keV). Cryogenic sample preservation is available for 2D and 3D imaging.

*Sample preparation.* SaOS-2 cells were seeded onto 500 nm thick Silicon Nitride ( $Si_3N_4$ ) membranes at a concentration of 10000 *cell/cm*<sup>2</sup>. After 4 and 10 days from osteogenic induction, the attachment and spreading of the cells was carefully verified using visible light microscopy prior to freezing. The membranes were frozen hydrated by rapid plunge freezing in a liquid ethane pool cooled with liquid nitrogen.

*Data acquisition.* The beam was focused using Kirkpatrick–Baez mirrors to a spot of 23 nm×37 nm, and the fluorescence maps were acquired at 17 keV. The sample was placed in the focal plane and analyzed in cryogenic conditions: elemental maps of Ca, Zn, P, S, Cl and K were obtained through raster scanning. The selected pixel sizes were 50 nm to depict the overall elemental distribution of the ROI, 25 nm for more precise maps of individual mineral nuclei. For each pixel, the fluorescence spectrum was recorded with an energy-resolving detector consisting of six silicon drift diodes, set orthogonal to the incoming beam.

*Data processing.* The acquired spectra were fitted using the PyMCA [137] open-source software to obtain quantitative data. The quantification of the fluorescence intensity is based on a fitting procedure of the recorded fluorescence spectra. Spectra evaluation is made by non-linear least square fitting of a mathematical model to the spectral data to deal with background and resolve peaks overlaps:

$$\chi^2 = \frac{1}{n - m} \sum_i \frac{[y_i - y_{fit}(i)]^2}{y_i} \quad (2.5)$$

where  $y$  is the signal from channel  $i$ ,  $y_{fit}$  is the calculated value of the fitting function in  $i$  channel,  $n$  is the number of channels and  $m$  is the number of parameters in the fitting function. The background was estimated before fitting and then subtracted so that the area under each peak gives the number of counts for that specific fluorescence line. Then, a map of the spatial distribution of the fluorescence intensity can be obtained for each element of interest.

---

### 2.1.8 Micro X-rays Fluorescence Microscopy (micro-XRFM) and micro- XANES

2D micro-X-ray fluorescence (micro-XRFM) maps and single point micro-X-ray Absorption Near Edge Structure (micro-XANES) spectra were acquired at the ID21 beamline at the ESRF in cryogenic conditions. The beamline provides a multi micro-analytical platform for the characterization of elements, species, molecular groups and crystalline structures in complex materials. In this context, cryo-microscopy is essential for the micro-analysis of radiation-sensitive samples as it allows sample characterization in a stable hydrated near-native state and preserves its morphological integrity under the beam. Sample preparation procedure is the same reported in Section 2.1.7.

*Data acquisition.* An energy range between 2 keV and 7 keV is available at ID21, which gives access to the K-edge of calcium at 4.05 keV. XANES spectra were acquired between 4.02 keV and 4.17 keV with 0.5 eV steps. Although the primary beam energy was set around that of the Ca K-edge energy region (4.999 keV), elements with absorption edges at lower energies were also subject to excitation and emission of fluorescence photons. Thus, micro-fluorescence element maps of Ca, P, and K were obtained simultaneously. Fluorescence maps were acquired with 5  $\mu\text{m}$  and 1  $\mu\text{m}$  pixel size to individuate depositions of interest that were then scanned with 500 nm pixel size.

*Data processing.* Elemental peaks deconvolution was performed using the data analysis tool PyMCA [137] as described in the previous section. XANES spectra were acquired with 1  $\mu\text{m}$  pixel size in Points of Interest (POIs) selected from the fluorescence maps, normalized and analyzed with PyMCA (see Section 2.1.7) and plotted using Orange [138].

## 2.2 Results

### 2.2.1 Gene Expression Analysis and Functional Characterization of SaOS-2 Cells after Osteogenic Induction

To characterize SaOS-2 cells after differentiative stimulus, calcium granules deposition and gene expression were evaluated. After seven days of induction, red granules marked by Alizarin red staining were evident in both the control and treated samples, but the latter exhibited more intense calcified nodules (Fig. 2.2 A). The gene expression analysis of six osteogenic markers revealed significant upregulation of all these gene transcripts in treated samples, except for osteonectin (SPARC1) mRNA (Fig. 2.2 B). In particular, the master osteogenic transcription factor (RUNX2) and its downstream controlled gene alkaline phosphatase (ALP) showed a notable increase in mRNA levels. In addition, the COL1A1 gene transcript was markedly increased, reaching a nine-fold higher expression when compared with control cells. Finally, a five-fold upregulation was also observed in the late osteogenic markers osteocalcin (BGLAP) and osteopontin (SPP1). Since the ALP enzyme plays a key role in bone mineralization and osteogenic differentiation, we assayed its catalytic activity and scored a positive correlation with the observed increased gene expression (Fig. 2.2 C). It is worth noting that osteogenic stimulation led to a relevant increase in SaOS-2 cells alkaline phosphatase activity despite its already high baseline levels [55]. Overall, overexpression of early (RUNX, COL1A1, ALP) and late (BGLAP, SPP1) osteogenic genes, increased ALP activity and the presence of extracellular mineral matrix underlined the osteogenic commitment even before differentiation.

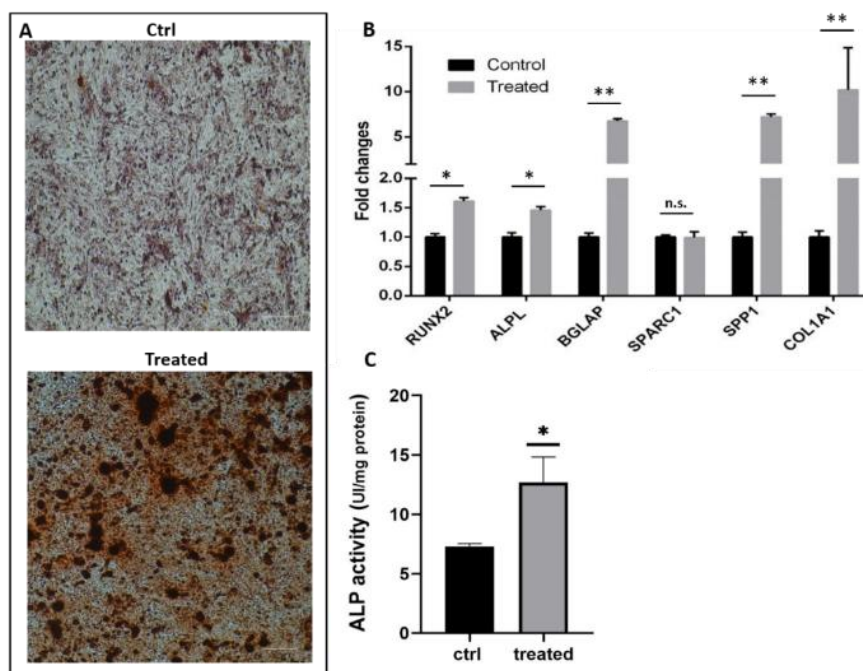


**Figure 2.2** Effects of osteogenic induction on SaOS-2 cell culture at 7 days. (A) Alizarin red staining. Scale bar is 200  $\mu\text{m}$ . (B) qPCR analysis of osteogenic markers (RUNX2, ALPL, SPARC, COL1A1, BGLAP and SPP1) was performed using GAPDH and HPRT1 as reference genes ( $2^{-\Delta\Delta\text{CT}}$  method). Fold changes from untreated control cells were calculated. Data from three biological replicates are reported as mean  $\pm$  SE. Two-way ANOVA followed by Sidak's multiple comparison test was performed, \*  $p < 0.05$ ; \*\*  $p < 0.01$ . (C) Alkaline phosphatase activity. Data are reported as the mean  $\pm$  SE of three biological replicates. Unpaired T-test was performed, \*  $p < 0.05$ .

## 2.2.2 Synchrotron-radiation X-ray techniques for SaOS-2 cells characterization

### 2.2.2.1 4 days control

Micro X-rays fluorescence microscopy (micro-XRFM) allowed to individuate calcium depositions by studying multiple cells in the same field of view (Fig. 2.3). Exploiting micro-XANES at the Ca-K edge, depositions were observed to be made of both calcium carbonate and calcium phosphate, and were mainly spotted in the

extracellular matrix (Fig. 2.3B red and pink asterisks and the corresponding spectra in Fig. 2.3 F). Nano-XRFM permitted to visualize intra and extracellular calcium depositions through a single-cell mapping. In particular, co-localization of Ca with Zn and P could be appreciated in some depositions, and Ca which didn't co-localize with P, probably indicative of calcium carbonate compounds presence, was observed as well (Fig. 2.4 from A to E). These findings were further confirmed by nano-XANES at the Ca  $L_{3,2}$  – *edge*. Calcium depositions exhibited average XANES spectra with intense  $L_3$  and  $L_2$  pre-peaks matching the calcite ( $CaCO_3$ ) reference spectrum (Fig. 2.5 A, B, C and D) and were mainly observed intracellularly through cryo-SXT. In addition, from a morphological point of view, elongated mitochondria were present in the cytoplasmic environment (Fig. 2.5 E and F).

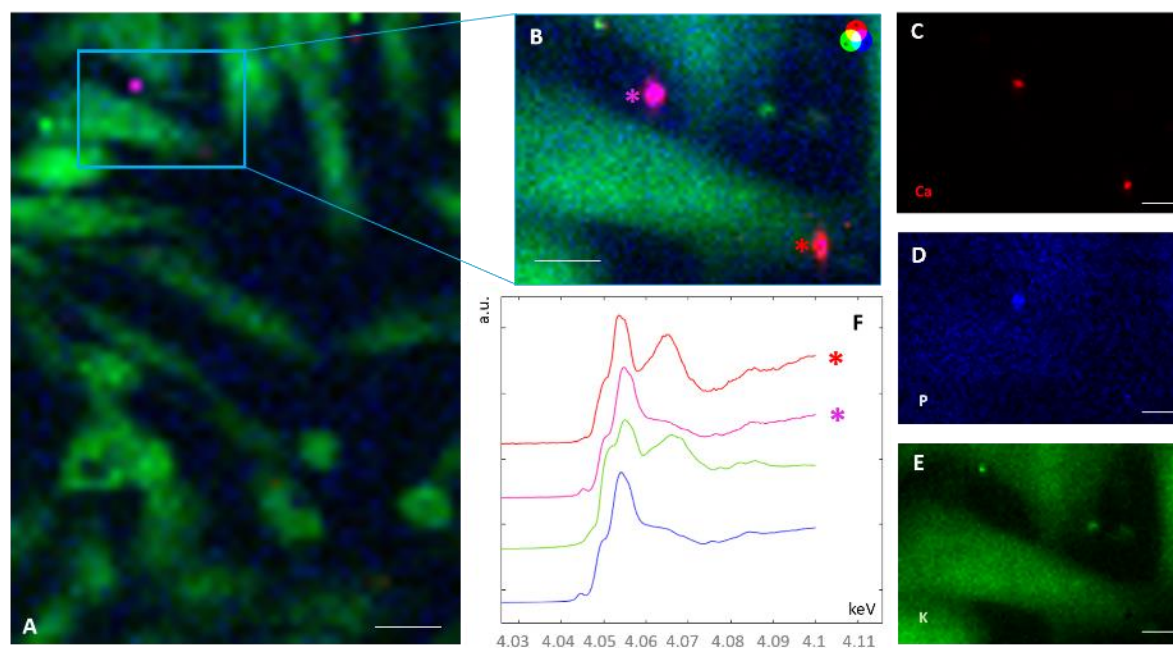


**Figure 2.3** Micro-XRFM maps acquired with 4.99 keV energy and 1  $\mu\text{m}$  step. A) merge of Ca, P and K fluorescence maps, B) zoom on a ROI selected from A). C), D), E) are Ca, P and K fluorescence maps respectively. F) micro-XANES spectra acquired from depositions in B) marked with pink and red asterisks. The green and blue spectra represent calcite and HA references. Scale bar is 35  $\mu\text{m}$ .



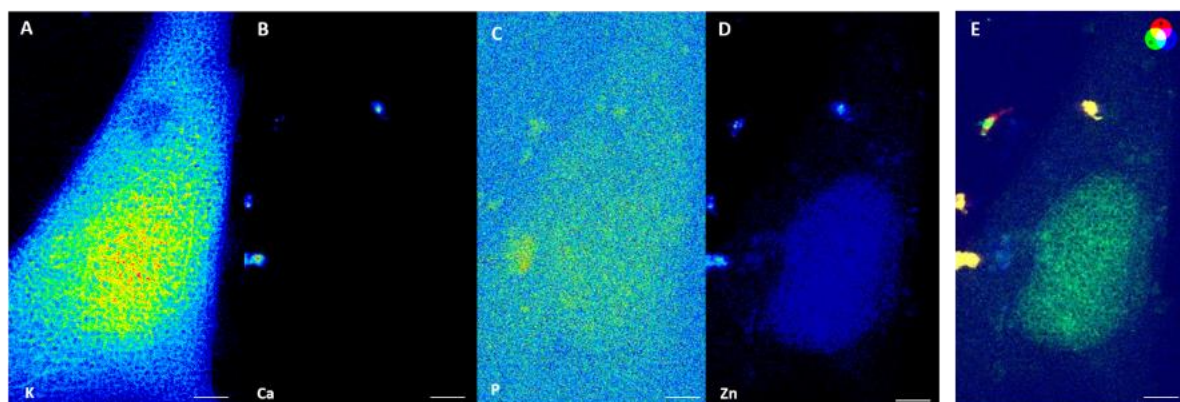


**Figure 2.4** Nano-XRFM maps acquired with 17 keV energy and 50 nm step. A), B), C) and D) represent K, Ca, P and Zn fluorescence maps respectively. E) merge of Ca, P and Zn fluorescence maps. Scale bar is 2  $\mu\text{m}$ .

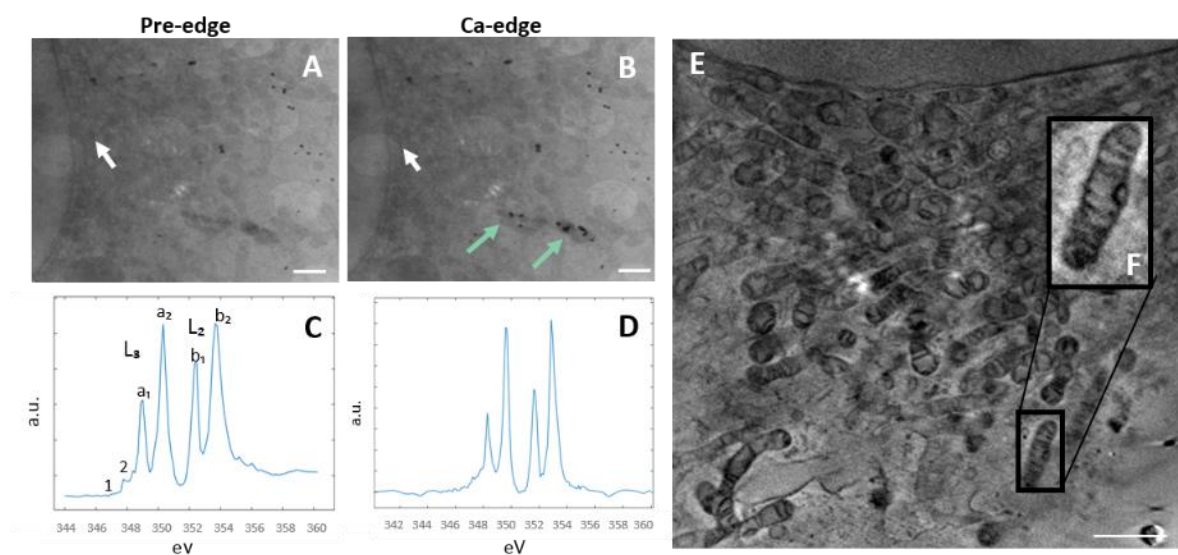


**Figure 2.5** A) and B) Average of absorbance projections recorded at the pre-Ca-edge energy region (A) ( $\approx 342$  eV) and (B) at the Ca  $L_3$  peak maxima ( $\approx 349$  eV). Scale bar is 1  $\mu\text{m}$ . White arrows indicate the edge of cell nuclei, and green arrows indicate the Ca depositions at the  $L_3$  edge. C) and D) show  $\text{CaCO}_3$  reference spectra and the average XANES spectrum of  $\text{CaCO}_3$  extracted from control cells at 4 days, respectively. In C) the main spectral features are indicated by letters and numbers. E) Tomogram slice of a 4 days control sample acquired at 352.9 eV and in F) a zoom on a mitochondrion. Scale bar is 2  $\mu\text{m}$ .

#### 2.2.2.2 4 days treated

Mineral depositions showed micro-XANES Ca K-edge spectra similar to calcium carbonate reference, but with a lower second absorption peak if compared to the calcite spectra observed in 4 days control samples (Fig. 2.6, red spectrum). This peculiar shape might represent a transition from calcium carbonate compounds to calcium phosphate ones. On the other side, in the extracellular environment, depositions were mainly made of calcium phosphate. These observations were additionally confirmed by nano-XRFM which displayed the co-localization of Ca with Zn and P in some depositions (Fig. 2.7). The combination of nano-XANES at the Ca  $L_{3,2}$  – *edge* with cryo-SXT allowed to characterize deposits composition and location. Intracellularly, calcium depositions showed spectral profiles similar to that of the calcium phosphate reference ( $Ca_3(PO_4)_2$ ), as reported in Fig. 2.8 C, suggesting a change in the deposition chemical state during the biomineralization process. Then, thanks to cryo-SXT the intracellular scenario was characterized: elongated mitochondria consistently decreased in number with respect to the control sample, leaving room for round mitochondria containing highly absorbing calcium granules as highlighted by Fig. 2.8 E. Round mitochondria appeared grouped suggesting the occurrence of a fission process. A magnified view of a round mitochondrion is shown in Fig. 2.8 F, and indicates an internal ordered organization of Ca (Fig. 2.8 G). The nano-XANES spectrum in Fig. 2.8 H suggests that intra-mitochondrial granules could be constituted by some form of calcium carbonate different from calcite [25]. Interestingly, round mitochondria appeared in close contact with vesicles (Fig. 2.8 I, black arrow) containing  $Ca_3(PO_4)_2$  depositions (Fig. 2.8 I, green arrow), suggesting a calcium transfer (Fig. 2.8 I, pink arrow and L). Furthermore, calcium granules were depicted through nano-XRFM and nano-X-ray fluorescence tomography in a

spherical 3D arrangement supporting the findings made through nano-XANES and cryo-SXT (Fig. 2.7 F).

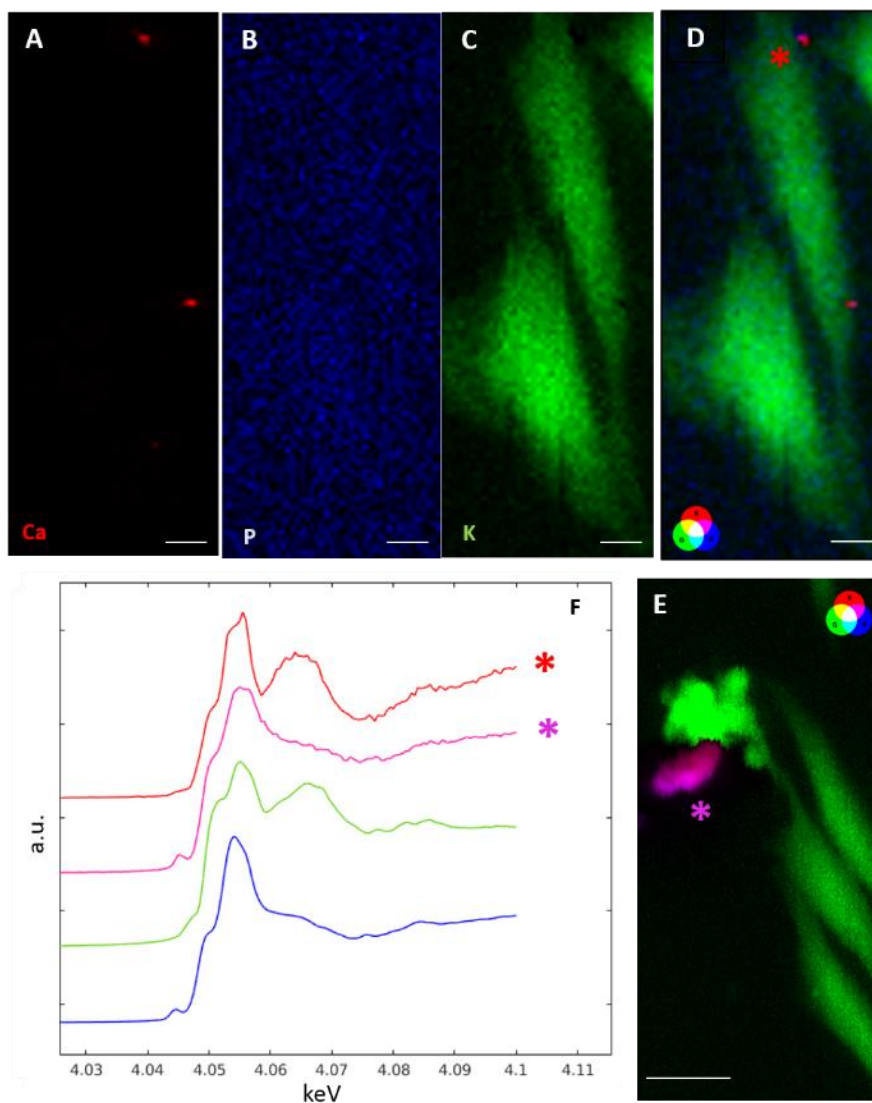


**Figure 2.6** Micro-XRFM maps acquired with 4.99 keV energy and 1  $\mu\text{m}$  step. A), B) and C) are Ca, P and K fluorescence maps respectively. D) Merge of Ca (red), P (blue) and K (green) fluorescence maps (scale bar is 15  $\mu\text{m}$ ). E) merge of Ca, P and K fluorescence from another ROI of the sample Scale bar is 50  $\mu\text{m}$ . F) Micro-XANES spectra acquired from depositions in D) (red asterisk) and E) (pink asterisk). The green and blue spectra represent calcite and HA references.

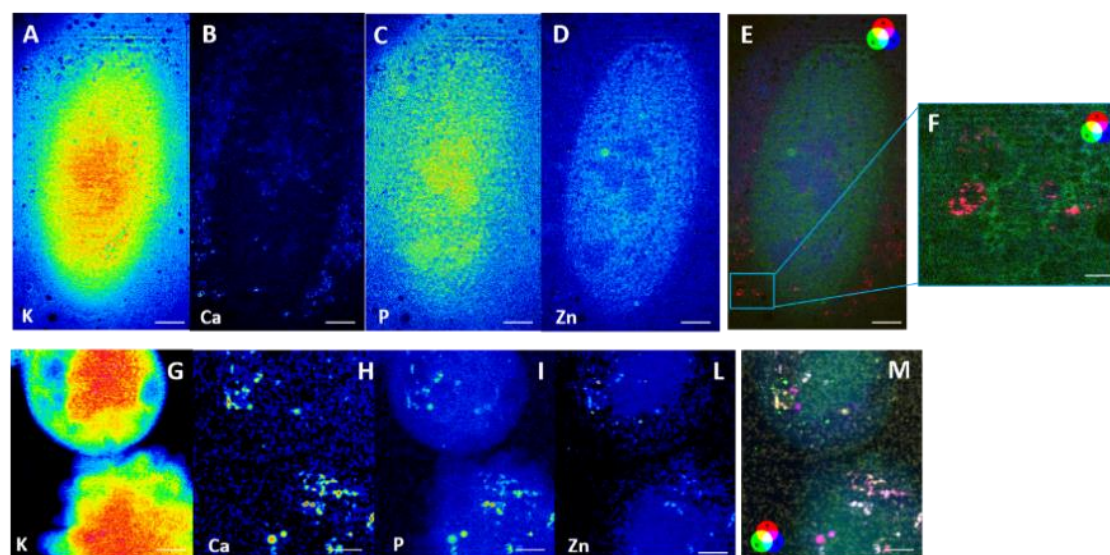


**Figure 2.7** Nano-XRFM maps acquired with 17 keV energy and 50 nm step. A), B), C) and D) represent K, Ca, P and Zn fluorescence maps respectively. E) merge of Ca (red), P (blue) and Zn (green) fluorescence maps. F) Fluorescence tomographic slice from a ROI of interest in E) highlighting the presence of spherical structures containing Ca granules. G), H), I) and L) represent K, Ca, P and Zn fluorescence maps respectively. M) merge of Ca (red), P (blue) and Zn (green) fluorescence maps. Scale bar is 3  $\mu\text{m}$ .

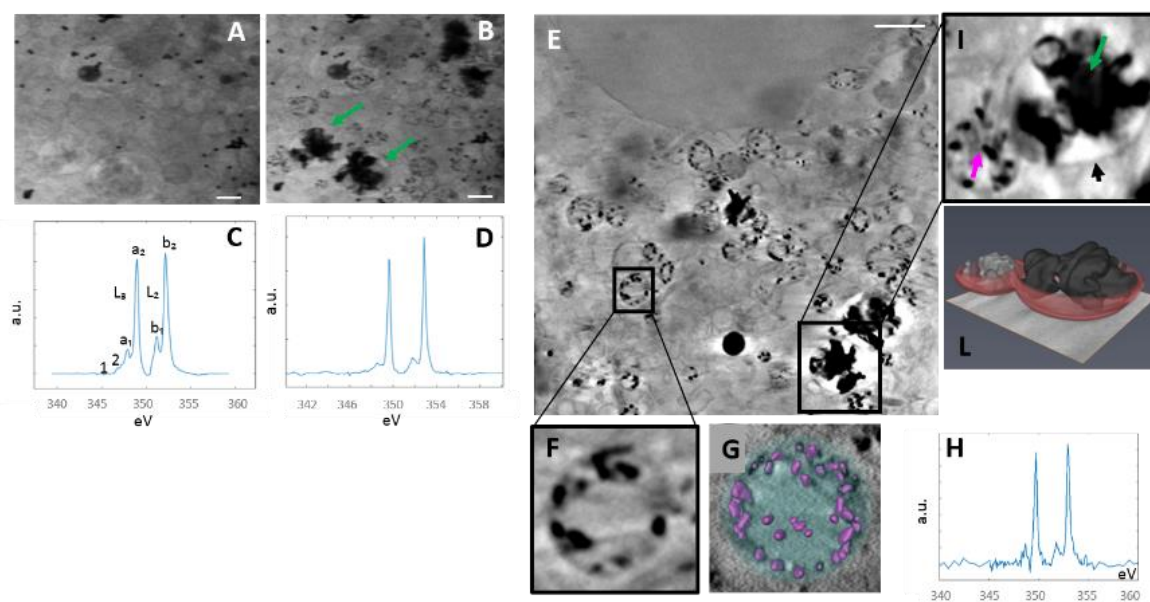


**Figure 2.8** A) and B) average of absorbance projections recorded at the pre-Ca-edge energy region

(A) ( $\approx 342$  eV) and at the Ca L<sub>3</sub> peak maxima (B) ( $\approx 349$  eV) Scale bar is 1  $\mu\text{m}$ . Green arrows indicate the Ca depositions at the L<sub>3</sub> edge. C) Displays Ca<sub>3</sub>(PO<sub>4</sub>)<sub>2</sub> reference spectrum where the main spectral features are indicated by letters and numbers. D) The XANES spectrum represents Ca<sub>3</sub>(PO<sub>4</sub>)<sub>2</sub> spectrum from Ca deposition. E) Shows a tomogram slice acquired at 352.9 eV of a 4 day treated sample. F) provides a zoom on a round mitochondrion and in (G) its 3D reconstruction can be observed: Ca structures are highlighted in pink and the corresponding XANES spectrum can be found in H). I) Shows a zoom on a round mitochondrion transferring Ca (pink arrow) to a calcium phosphate deposition (green arrow) contained within a vesicle (blue arrow). The corresponding 3D reconstruction is provided in L). Scale bar is 1  $\mu\text{m}$ .

### 2.2.2.3 10 days control

Micro-XRFM and micro-XANES provided interesting insights on 10 days control samples. Calcium depositions showed micro-XANES spectra similar to calcium carbonate but having a lower second absorption peak with respect to the standard calcite spectrum (Fig. 2.9 red spectrum). As previously speculated for 4 days treated samples, this shape could represent a transition from a calcium carbonate to a calcium phosphate compound. Furthermore, depositions made of HA were present (Fig. 2.9 blue spectrum). Interestingly, some calcium depositions provided spectra with no shoulder in the pre-peak region (Fig. 2.9, yellow spectrum) which could be attributed to some form of amorphous calcium carbonate probably involved in the crystalline calcium carbonate generation process as suggested by Werner et al. [59]. Nano-XRFM confirmed the presence of calcium carbonate displaying Ca and Zn co-localization in deposits inside the cytoplasmic environment (Fig. 2.10). Then, nano-XANES at the Ca L-edge showed average spectra matching both calcite ( $\text{CaCO}_3$ ) and  $\text{Ca}_3(\text{PO}_4)_2$  references (Fig. 2.11 A to H), supporting the observation made at microscopic scale. Finally, mitochondria morphology was defined thanks to cryo-SXT which highlighted the presence of both elongated and round mitochondria in the



cellular environment, the latter containing highly absorbing Ca structures (Fig. 2.11 I, L and M).

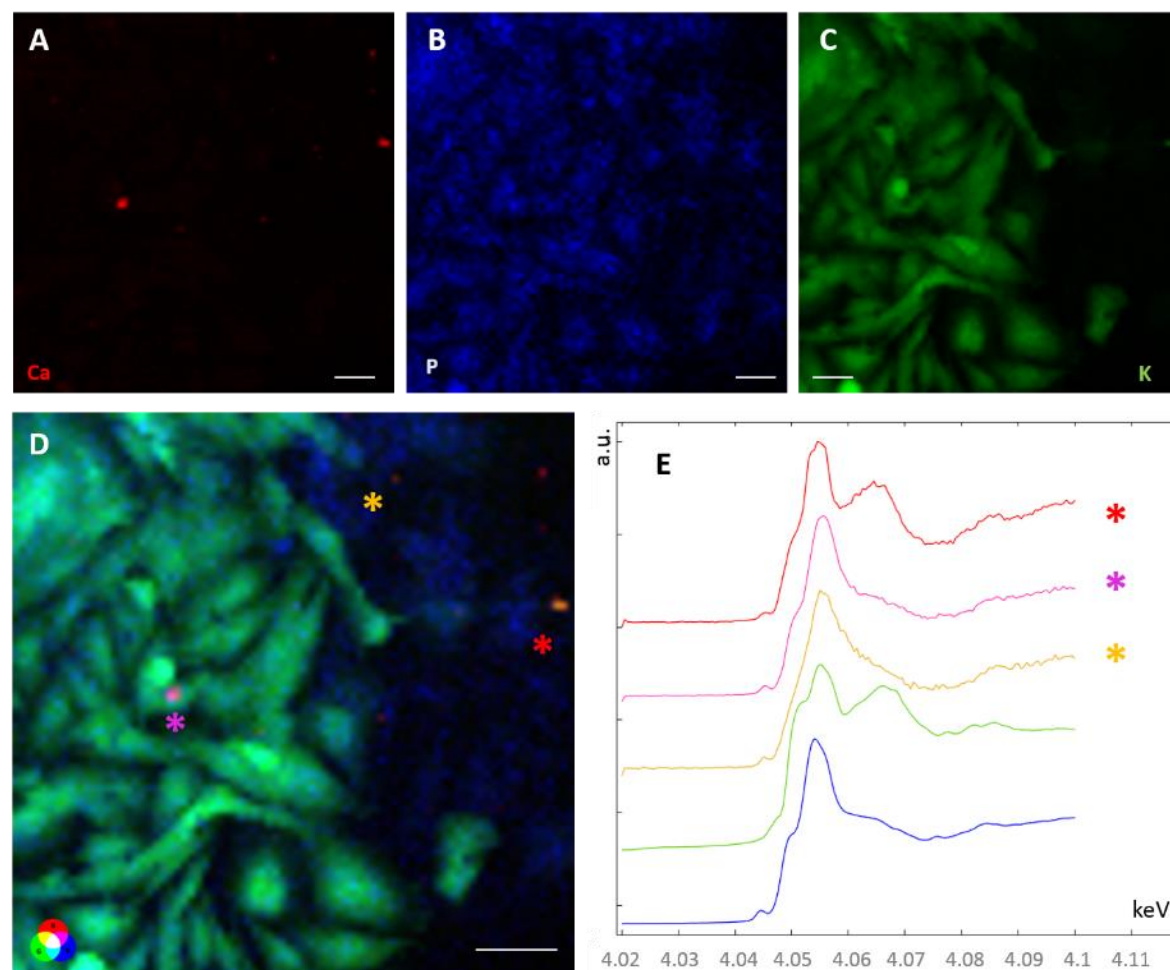


**Figure 2.9** Micro-XRFM maps acquired with 4.99 keV energy and 1  $\mu\text{m}$  step. A), B) and C) are Ca, P and K fluorescence maps respectively. D) merge of Ca (red), P (blue) and K (green) fluorescence maps. E) micro-XANES spectra acquired from depositions in D) indicated by asterisks. The green and blue spectra represent calcite and HA references. Scale bar is 50  $\mu\text{m}$ .

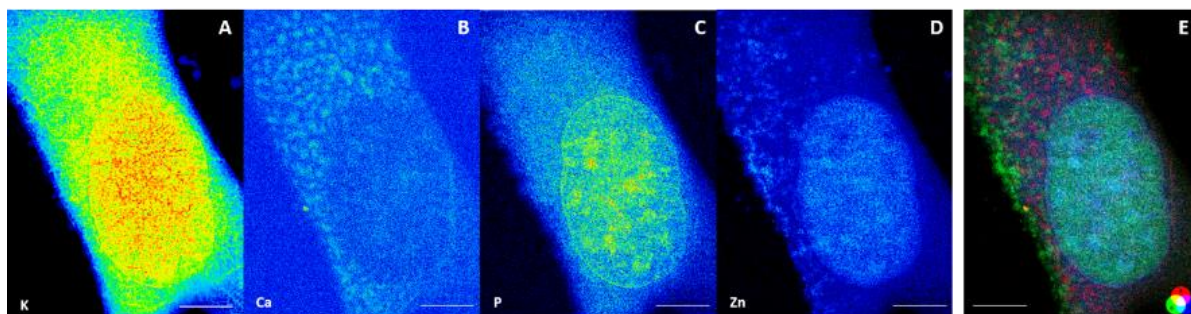


**Figure 2.10** Nano-XRFM maps acquired with 17 keV energy and 50 nm step. A), B), C) and D) represent K, Ca, P and Zn fluorescence maps respectively. E) merge of Ca (red), P (blue) and Zn (green) fluorescence maps. Scale bar is 5  $\mu\text{m}$ .

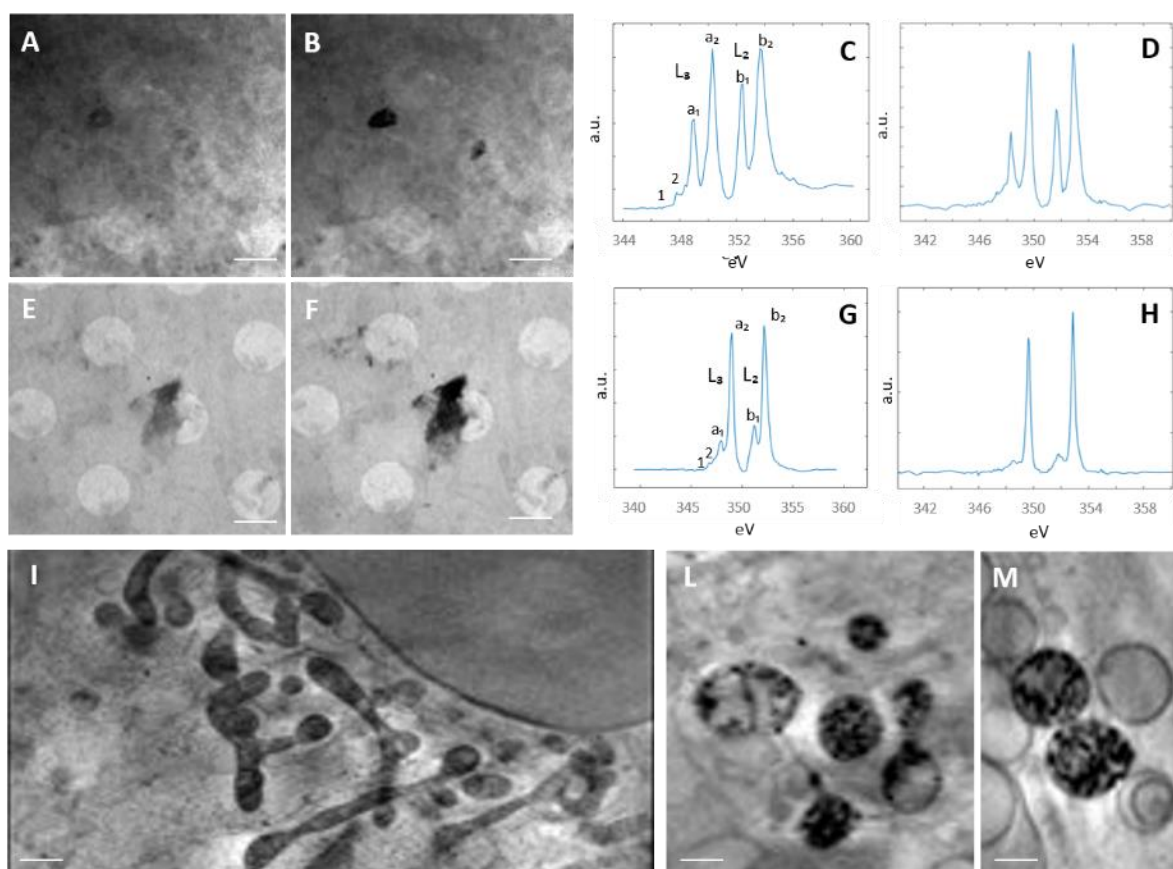


**Figure 2.11** A), B), E) and F) average of absorbance projections recorded at the pre-Ca-edge energy region (A and E) ( $\approx 342$  eV) and at the Ca  $L_3$  peak maxima (B and F) ( $\approx 349$  eV) Scale bar is 1  $\mu\text{m}$ . C) and D) show the average XANES spectrum of  $\text{CaCO}_3$  deposition in B) and  $\text{CaCO}_3$  reference spectra, respectively. G) shows  $\text{Ca}_3(\text{PO}_4)_2$  reference spectrum. In H) the average XANES spectrum

represents  $\text{Ca}_3(\text{PO}_4)_2$  spectrum from Ca deposition in F). In C) and G) the main spectral features are indicated by letters and numbers. I) Shows a tomogram slice acquired at 352.9 eV of a 10 days control sample (scale bar is 1  $\mu\text{m}$ ). L) and M) provide a zoom on mitochondria containing calcium granules (scale bar is 300 nm).

#### 2.2.2.4 10 days treated

Combining micro-XRFM and micro-XANES, calcium depositions in the extracellular environment were observed to be made of HA (Fig. 2.12). These findings were confirmed at the nanoscopic scale through XRFM which showed co-localization of Ca with Zn and P in both intra and extracellular environment (Fig. 2.13). From the morphological point of view, the scenario further evolved with respect to 4 days of differentiation. In tomographic images, round mitochondria appeared more elongated and bound (Fig. 2.14 C and D), mimicking a mitochondrial fusion process. In addition, mitochondria were linked together, suggesting the formation of a mitochondrial network (Fig. 2.14 E) and a restoration of the conventional elongated shape. In the reconstruction slices reported in Fig. 2.14 C and D, these organelles exhibited highly absorbing structures not made of Ca, as confirmed by nano-XANES spectroscopy. This could be a consequence of the calcium transfer from mitochondria to depositions during the early days of differentiation suggested by Fig. 2.8 I. In this case, once transferred, calcium is likely to be substituted by an absorbing element possessing the same electronic valence (for example  $\text{Mg}^{2+}$ ). Nano-XANES at the Ca  $L_{3,2}$  – *edge* and cryo-SXT confirmed that, after 10 days of osteogenic differentiation, the chemical structure of the mineral depositions further evolved towards HA (Figure 2.14 A, B, C and D). Intracellularly, spectra acquired from calcium depositions exhibited the main characteristic  $L_3$  and  $L_2$  absorption peaks of calcium compounds and the low-intensity peaks structure before the  $L_3$  main peak ( $a_1$ ,  $a_0$  in Fig. 2.14



C). Furthermore, the “hook” shape of the  $L_2$  pre-peak ( $b_1$  in Fig. 2.14 C), which is typical of the HA Ca  $L_{3,2}$  -edge absorption spectrum, could be easily observed [23].

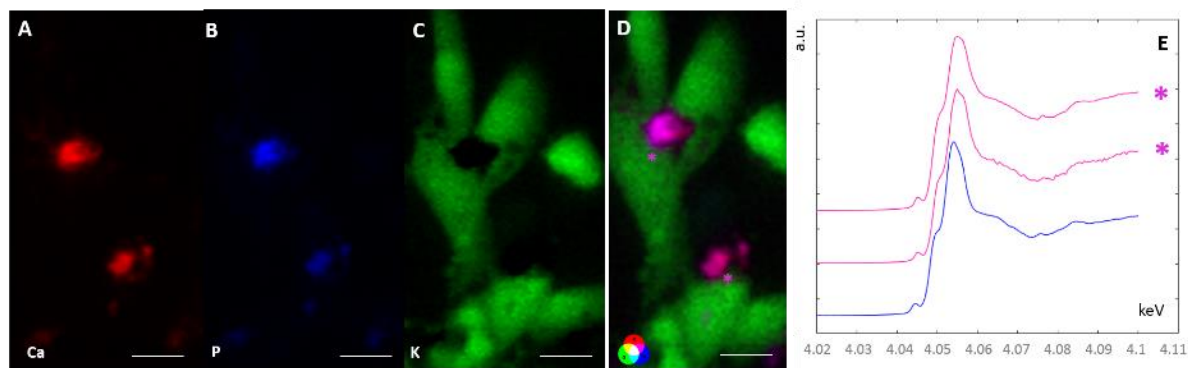


**Figure 2.12** Micro-XRFM maps acquired with 4.99 keV energy and 1  $\mu\text{m}$  step. A), B) and C) are Ca, P and K fluorescence maps respectively. D) merge of Ca (red), P (blue) and K (green) fluorescence maps. E) micro-XANES spectra acquired from depositions in D) indicated by asterisks. Scale bar is 50  $\mu\text{m}$ .

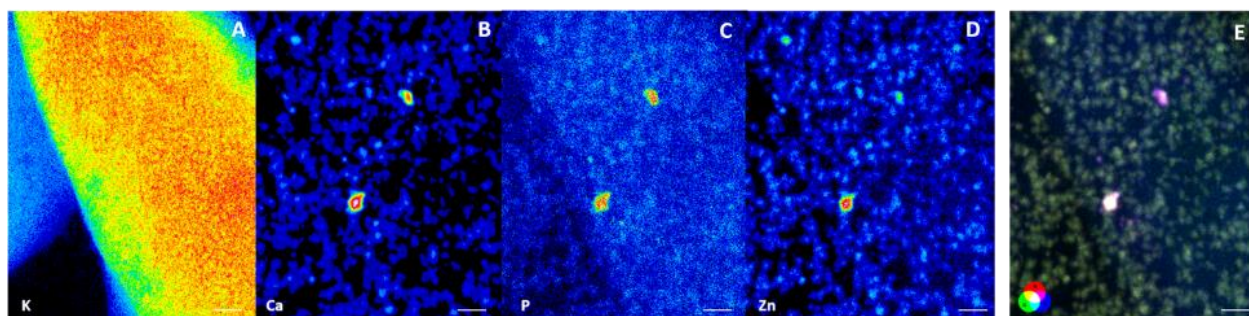


**Figure 2.13** Nano-XRFM maps acquired with 17 keV energy and 50 nm step. A), B), C) and D) represent K, Ca, P and Zn fluorescence maps respectively. E) merge of Ca (red), P (blue) and Zn (green) fluorescence maps. Scale bar is 2  $\mu\text{m}$ .

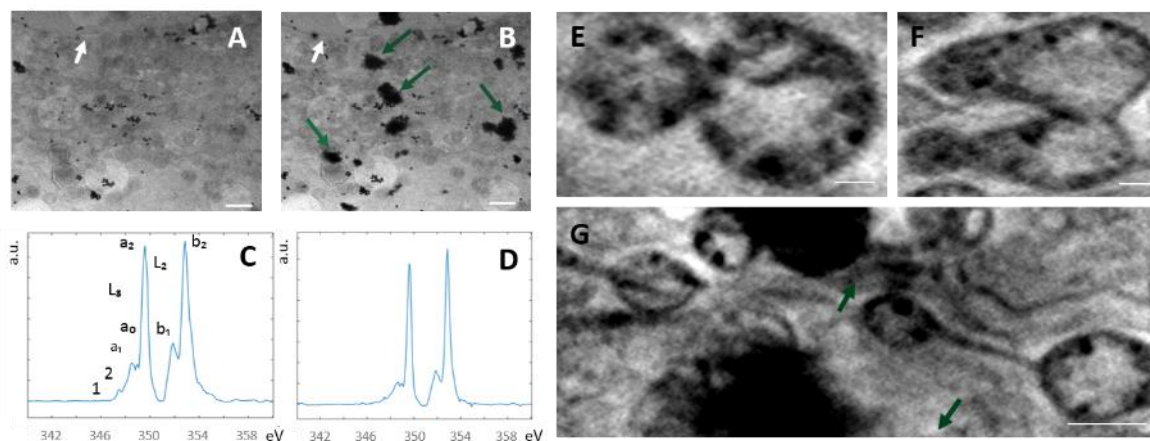


**Figure 2.14** A) and B) average of absorbance projections recorded at the pre-Ca-edge energy region (A) ( $\approx 342$  eV) and at the Ca L<sub>3</sub> peak maxima (B) ( $\approx 349$  eV). Scale bar is 1  $\mu\text{m}$ . Dark-green arrows indicate the Ca depositions at the L<sub>3</sub> edge. C) and D) show representative HA spectra detected in a deposition and HA reference spectra, respectively. In C) the main spectral features are indicated by letters and numbers. From E) to G): tomogram slices of a 10 days treated sample acquired at 352.9 eV. E) provides a zoom on mitochondria containing elements different from Ca, F) and I) show a mitochondrion during a fusion process and a zoom on a mitochondrial network, respectively. Dark-green arrows indicate HA depositions. Scale bar is 300 nm.

For a more in-depth description of the spectroscopic data, principal component analysis (PCA) was used to better distinguish the nano-XANES spectra acquired at 4 and 10 days after treatment. PCA considers the whole spectral profile (Fig. 2.15 A and C), enhancing important information such as peaks shape and intensity.

The technique was applied to standard spectra of calcium phosphate  $\text{Ca}_3(\text{PO}_4)_2$  and HA, to evaluate the efficacy of the data processing in the extraction of the relevant information from XANES results (Figure 2.15 A). The score PC1 vs. PC2 plot (Figure 2.15 B) showed an efficient discrimination between calcium phosphate and HA, due to their peculiar spectral features within the entire energy region of interest (between 347 and 355 eV). Concerning the PCA results related to the spectra

acquired from cells (Figure 2.15 C and D), a good separation between the treated 4 and 10 days spectra can be observed, confirming the evolution of the chemical composition of Ca depositions. In this case, the discrimination seems to be enhanced by changes in shape and relative intensity presented by the main peaks,  $L_3$  (at  $\approx 349$  eV) and  $L_2$  (at  $\approx 353$  eV), by the pre-peak  $a_0$ , previously mentioned as a discriminant between calcium phosphate and HA, and the pre-peak  $b_1$ .

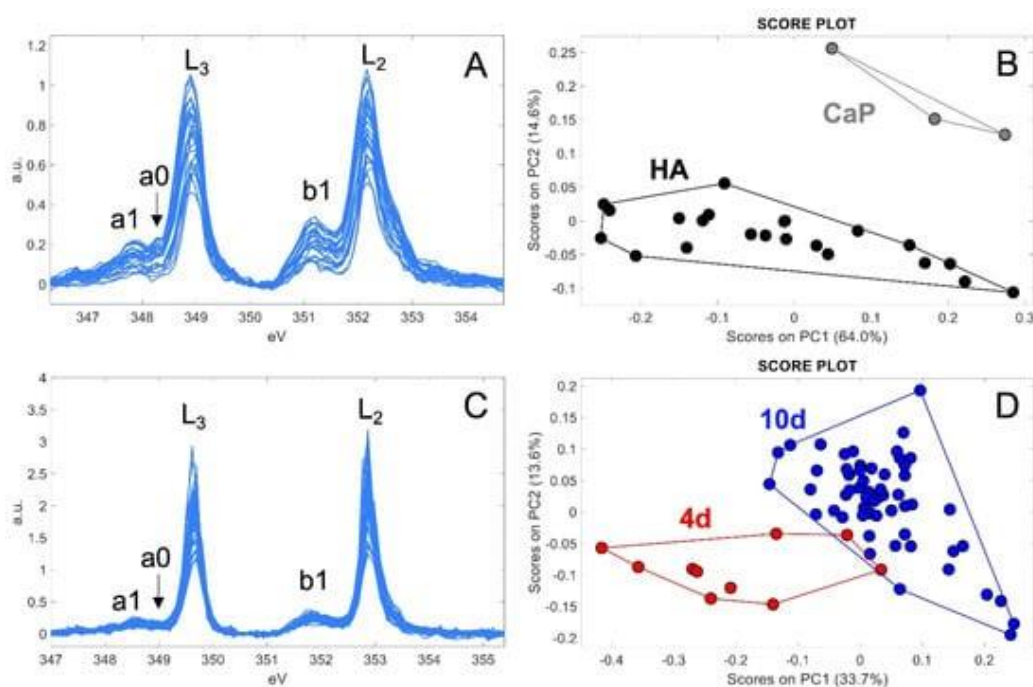


**Figure 2.15** Results of principal component analysis applied to nano-XANES spectra: (A) measured standard spectra of calcium phosphate (CaP) and hydroxyapatite (HA); (B) score plot showing the separation between calcium phosphate and HA spectra; (C) measured spectra from Ca depositions taken at 4D and 10D after the treatment; (D) score plot showing the separation between 4 days and 10 days spectra.

### 2.2.2.5 PCA analysis on micro-XANES Ca-K edge spectra

To further characterize micro-XANES data, we used PCA analysis to better distinguish the spectra acquired under each experimental condition. Among the

derived spectra, the reference spectra from HA and calcite were considered too. The score PC1 vs PC3 scatter plot is displayed in Fig. 2.16 A and shows a clear division of the spectra in four clusters. A good separation between HA and calcite (green and light blue clusters in Fig. 2.16 A) can be appreciated, calcite spectra being mainly spotted in control samples (light blue average spectrum in Fig. 2.16 B) and HA detected in treated cells and 4 days SaOS-2 (green average spectrum in Fig. 2.16 B). Interestingly, 10 days control spectra generate two more clusters (orange and red clusters with the corresponding average spectra in Fig. 2.16 B). The red one is characterized by spectra similar to those of calcite but showing a lower second absorption peak with respect to the reference. The second cluster (orange average spectrum) provides a pre-peak at 4.0505 keV and the main absorption peak of the white line at 4.0551 keV.

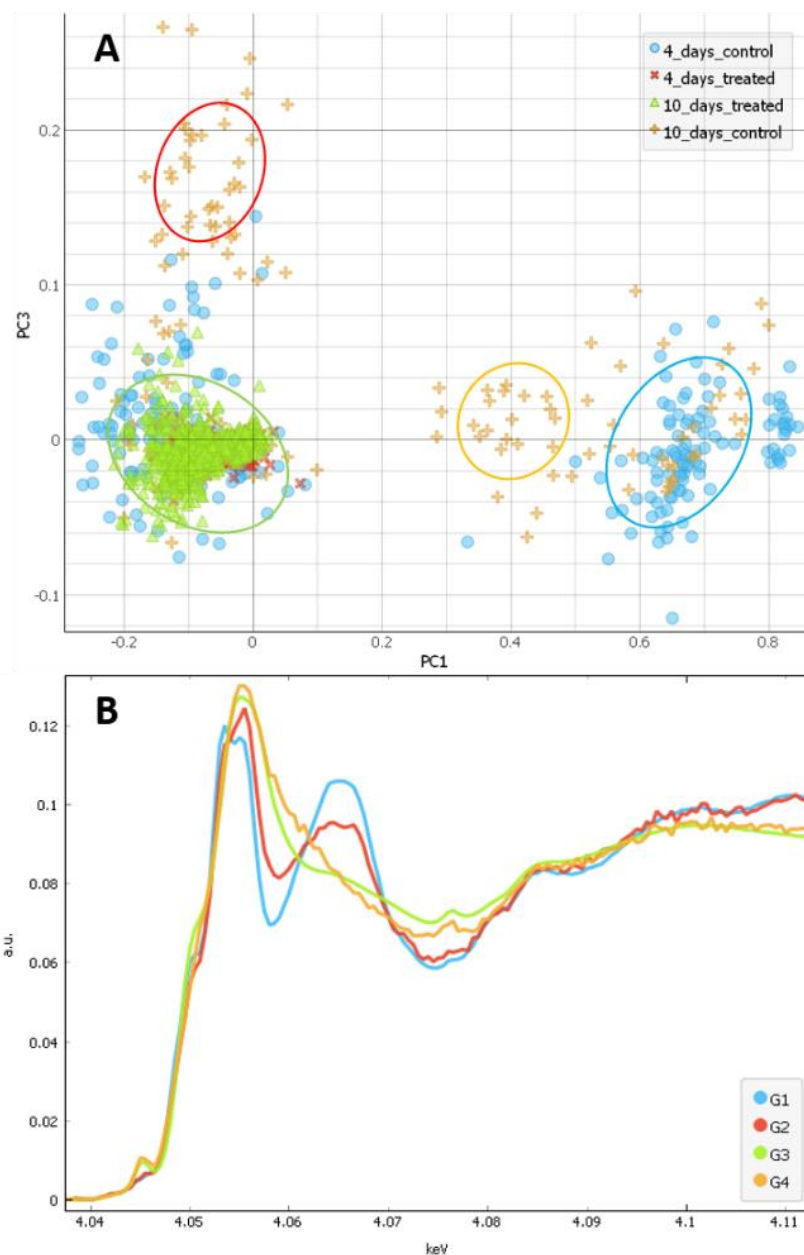


**Figure 2.16** Results of principal component analysis applied to micro-XANES spectra: A) score plot showing the separation between HA and calcite spectra (green and light blue clusters respectively). The different experimental conditions can be easily identified thanks to the legend in A). B) average spectra from data groups selected in the scatterplot: red, light-blue, orange and green selection from A).

---

## 2.3 Discussion and Future Perspectives

Recent studies have pointed out that OS development might be associated with differentiation defects that may arrest cells at an undifferentiated stage [43]–[45]. In order to depict and characterize the defective differentiation process occurring in OS, we studied the early phases of bone biomineralization in the osteoblast-like SaOS-2 cell line. SaOS-2 cells were induced to differentiate towards osteoblasts using a differentiating cocktail, and data derived from samples at 4 and 10 days after treatment were compared to controls. To delineate early bone biomineralization, which is still lacking a complete characterization, the evolution and formation of bone mineral matrix was monitored exploiting synchrotron-based nano-cryo-XANES microscopy at the Ca  $L_{3,2}$  – *edge*, cryo-soft X-rays tomography (cryo-SXT), micro- and nano-X-rays fluorescence microscopy (XRFM), and micro-cryo-XANES microscopy at the Ca K-edge.

It is known that biomineralization culminates in the formation of HA nodules. However, the pathway leading to the generation of crystalline materials within the cells has been poorly characterized, especially in human cell-lines. In a previous work on bone mesenchymal stem cells (bMSCs) induced to differentiate towards osteoblasts [63], it was suggested that biomineralization starts within the cell with calcite which evolves towards hexagonal HA crystals similar to those present in mature human bone. Furthermore, it was also revealed that in the early phases of biomineralization, bone-constituting elements, including Zn, can be incorporated along differentiation [139]. Studying SaOS-2 cells differentiation process we observed that, like in bMSCs differentiation, hexagonal HA is the final product of biomineralization. More precisely, the biomineralization process starts within the cells with the formation of crystalline calcium carbonate, and continues with the

---

nucleation of calcium phosphate nodules which evolve towards HA [40]. Calcium phosphate and HA nano-XANES spectra were distinguished exploiting PCA analysis, thus underlining the evolution of calcium phosphate compounds generated at 4 days towards HA at 10 days after treatment. After 4 days of osteoblastic induction, some calcium carbonate mineral nuclei were present, confirming that biomineralization starts within the cell early after the osteogenic stimulus as observed in bMSCs [139]. The occurrence of Zn in the early mineral nuclei, observed thanks to nano-XRFM, provided experimental evidence of the germinal role of Zn in HA nucleation as hypothesized a long time ago [140] and later shown in bMSCs by Procopio et al. [65], [139]. In summary, all these findings suggest that the process of Ca deposition formation can start with a calcium carbonate compound, which subsequently incorporates Zn and nucleates HA by integrating phosphates to build the lattice structure of the bone mineral.

In a recent work, Werner et al. [59] tested the hypothesis that  $CaCO_3$ -formed bioseeds can be transformed into a mixed hybrid mineral made of calcium carbonate and phosphate, and finally into HA. Therefore, they proposed that the initial  $CaCO_3$  bioseed formation is enzymatically driven by CA, and that the subsequent carbonate/phosphate exchange reaction is a non-enzymatic step when a phosphate-rich extracellular environment is present. In another work [65], they also showed that orthophosphate and hydrolysis products of polyphosphate inhibit CA activity, triggering a feedback regulatory system between CA-driven calcium carbonate deposition and the consequent inactivation of this process by orthophosphates, which are fundamental for HA formation. The provided body of knowledge might elucidate the observations made in 10 days control cell cultures which showed a slowed biomineralization process when compared to the treated ones. The spectrum

---

displayed in Fig. 2.9 (red line) was acquired from a mineral deposition in a 10 days control sample. Its shape suggests the presence of a mixed hybrid mineral generated by the transition from calcium carbonate to calcium phosphate. In fact, CA may act catabolizing carbonate group precipitation in favor of a carbonate-phosphate exchange which lowers the second calcium carbonate absorption peak and generates the calcium phosphate pre-peak. It can be speculated that the slowdown of this process is due to the low concentration of phosphates in control cultures with respect to treated ones (we can considerate the differentiating treatment as a source of polyphosphates), and to a disruption of the feedback regulatory system that inhibits CA action. In addition, several spectra characterized by a single absorption peak and a pre-peak could be appreciated as well (Fig. 2.9 yellow spectrum). By a comparison with Ca-K edge XANES spectra available in literature [73], [74], [141], [142], it was found that they could be generated by some form of amorphous calcium carbonate (ACC) compound, which has been proposed as HA bioseed during the  $CaCO_3$  production catalyzed by CA.

The main results obtained from 4 days control samples show similarities with observations made in bMSCs [63]. Both cell lines exhibited  $CaCO_3$  nodules in the intracellular environment indicating the presence of similar osteogenic pathways. This highlights that early differentiated osteoprogenitors and OS cells are similar, supporting the hypothesis that OS cells might arise from MSCs that are unable to undergo terminal differentiation [143]. Their ability to evade senescence may allow OS cells to self-renew and respond to growth factors like their osteoprogenitors [43]. In fact, in agreement with the similarities observed between SaOS-2 and bMSCs, less aggressive OS are known to resemble differentiated MSCs while more aggressive phenotypes mainly behave like their early osteoprogenitors [144].



---

Furthermore, this work provides a better understanding of the relationship between intracellular and extracellular mineralization, in particular on calcium phosphate nucleation within the cell. Calcium phosphate deposits are known to reside intracellularly in mitochondria of mineralizing cells [36]. In addition, Boonrungsiman et al. recently identified calcium phosphate both within osteoblast mitochondrial granules and in intracellular vesicles transporting nodules to the extracellular matrix of mouse cells. They also observed calcium-containing mitochondria conjoining vesicles, suggesting a storage role of mitochondria and a transport mechanism driven by vesicles [36]. Interestingly, a similar behavior was observed in SaOS-2 cells. At 4 days after osteogenic induction, mitochondria contained very small calcium granules and some of them could be observed linked to vesicles containing calcium phosphate depositions, suggesting a mineral transfer. After 10 days of differentiation, no calcium granules could be appreciated in mitochondria, supporting the previously hypothesized transfer, and HA deposits could be observed in both intra and extracellular matrix. A complete scheme of the mechanism of Ca nucleation and transport during the early stages of biomineralization is provided in Fig. 2.17.

Indeed, mitochondria play a role in calcium deposits formation at the intracellular level and shape variations of these organelles might be relevant for the process as they are strongly related to cell functionality. It is also known that mitochondria shape varies according to fission and fusion processes [145]. Fission mainly occurs in growing and dividing cells having non-fused and spherical mitochondria that produce energy through a glycolytic metabolism [145]. In particular, actively proliferating cells, such as stem cells and cancer cells use aerobic glycolysis for energy production. On the other side, fused and interconnected mitochondria are found in cells depending on OXPHOS. It has been observed that pluripotent stem cells mainly use

---

glycolysis switching to OXPHOS during differentiation [146]. Interestingly, mitochondrial dynamics are also involved in MSCs differentiation where mitochondria elongation has been correlated with osteogenesis [147]. In this context, SaOS-2 cells expressed typical genes of mature osteoblasts, such as ALP, BGLAP and SPP1 (Figure 2.2 B), providing evidence of their osteoblast-like nature. In addition, the cell line exhibited elongated mitochondria, indicating a metabolism typical of osteoblasts that relies mainly on OXPHOS. However, at 4 days after induction, mitochondria appeared non-fused and spherical suggesting the presence of a glycolytic metabolism which is characteristic of proliferating stem cells. It is interesting to underline that the vitamin D [148] present in the differentiating cocktail might act reprogramming OS cells and making them more similar to their osteoprogenitors. Later during differentiation, SaOS-2 switched their metabolism to OXPHOS, exhibiting fused and interconnected mitochondria.

In conclusion, this study sheds light on the genesis and evolution of HA in differentiating osteosarcoma cells, identifying HA as the final product of a restored biomineralization. Furthermore, our findings propose a mechanism for mineral transport based on the interaction between mitochondria and vesicles. Finally, through a morphological study of mitochondria, reprogramming of OS cells induced to differentiate was observed, as similarly reported for other cancer types [29,30,31]. Nevertheless, further investigations on other OS cell lines are necessary to corroborate the mitochondria-mediated mechanism proposed by our study.

The aforementioned findings will be better characterized performing additional experiments. First of all, nano-X-ray diffraction will be used to analyze the crystalline structure of calcium depositions and unveil their lattice organization. Mineral depositions are likely to be made of nano crystals rather than well-organized crystals, thus displaying a peculiar diffraction pattern. Indeed, mitochondria metabolism

needs to be studied by monitoring oxygen consumption in SaOS-2 cells cultures during differentiation. Furthermore, a focus on mitochondrial fission and fusion processes will be made by identifying which respiratory mitochondrial complex is responsible for the metabolic switch from glycolysis to OXPHOS. Finally, an evaluation of the interplay between the two key enzymes for the mineralization process (CA and ALP) will be performed. CA is responsible for the carbonate precipitation in the early phases of mineral nucleation and the latter is fundamental for phosphates availability in HA crystal building. Gene expression and enzymatic activity will be conducted to identify the molecular target and signal pathways involved in the regulation of differentiated cells mineralization.

These findings reinforce the theory that osteosarcoma originates from defective osteoblastic differentiation, supporting therapeutic approaches based on differentiating agents that might restore physiological mineralization in OS cells.

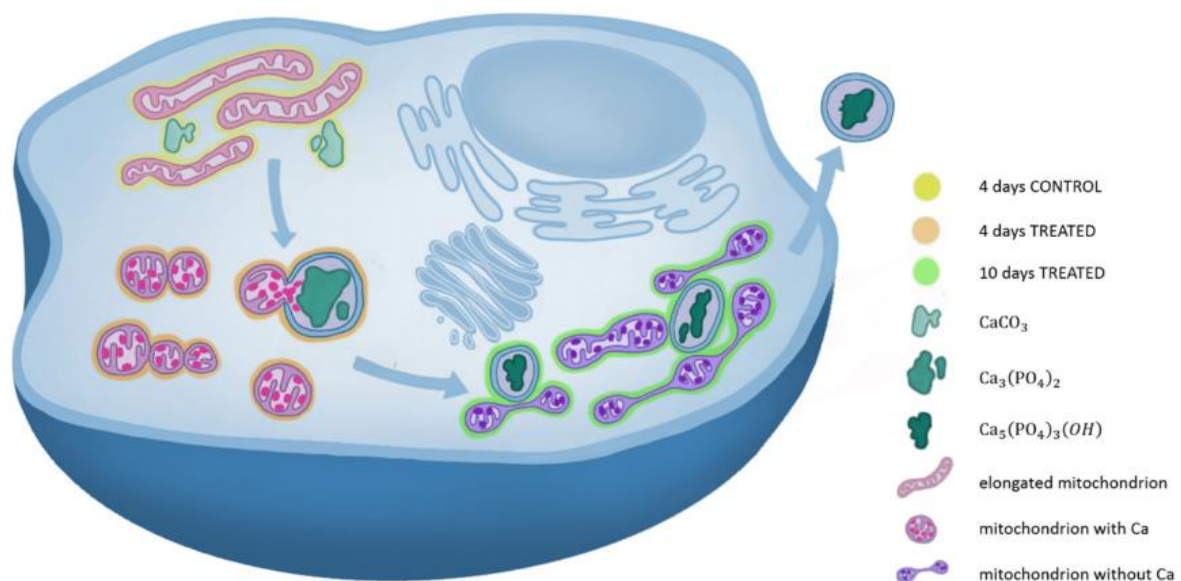


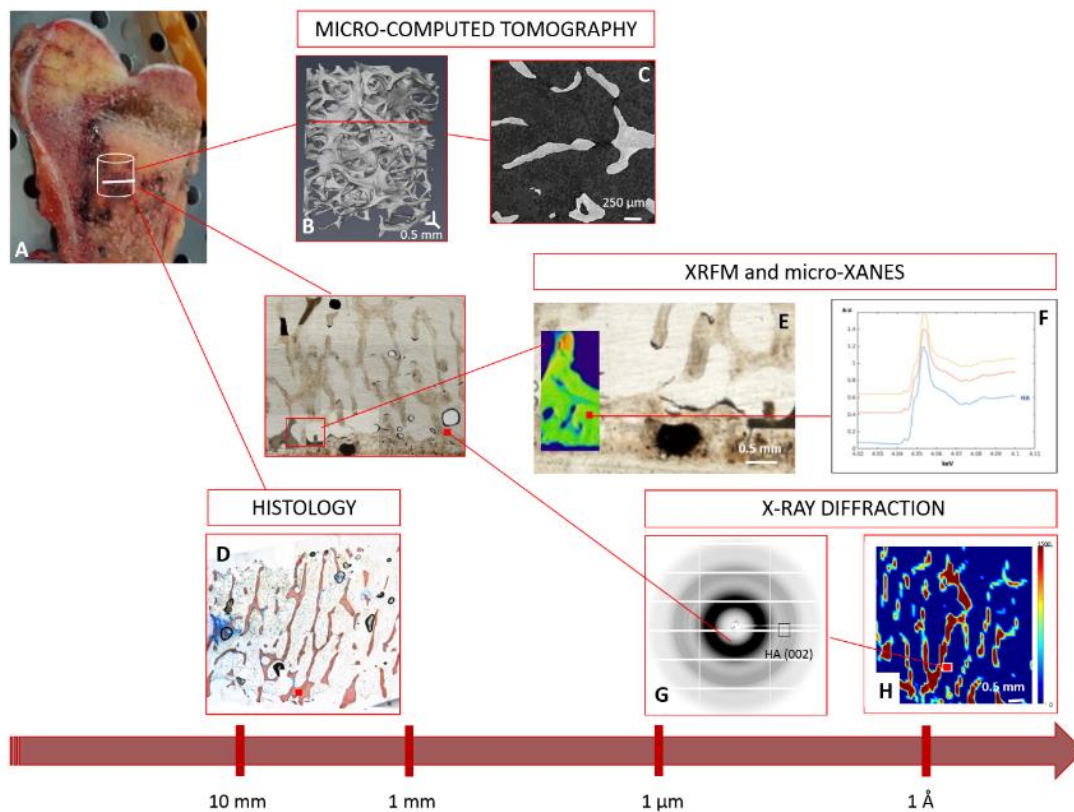
**Figure 2.17** Scheme of an osteosarcoma cell. In yellow, orange and green, are highlighted representative cytoplasmic environments of a 4 days control, 4 days treated, and 10 days treated sample, respectively. Calcium depositions are colored in different shades of green. From the lightest

to the darkest: calcite, calcium phosphate and hydroxyapatite. Elongated mitochondria can be observed in light pink, mitochondria containing calcium in pink and mitochondria after calcium transfer are in violet.

# Chapter 3: Characterization of Osteosarcoma human tissue

OS is the most common primary malignant bone cancer affecting children and young adults and includes several sub-types having different phenotype and characteristics, therapeutic approaches, and outcome. Regardless of the OS sub-type, a common feature is the uncontrolled tumor cells proliferation which unbalances bone homeostasis and creates an abnormal tissue micro-environment affecting the mechanical properties of the bone and producing the so-called woven bone. According to the sub-type, OS is treated by multi-modal treatment approaches that combine surgery with multi-agent chemotherapy. Unfortunately, the current treatment protocols are not effective for all patients and OS can recur locally or spread to other vital organs. Therefore, the effectiveness of new therapeutic approaches is constantly investigated. Recently, significant efforts have been made to characterize the tumour micro-environment (TME) at a cellular level to identify potential new therapeutic targets and strategies. However, an extensive structural and morphological characterization of OS TME on both organic and mineralized matrices at different length scale is currently still lacking. Over the last decade, cutting-edge synchrotron imaging techniques have been developed to overcome the limitations in spatial resolution [149] while facilitating nondestructive ex vivo analysis at high resolution. In our research, we used three different X-ray synchrotron-based techniques to perform a complementary multiscale analysis (with a spatial resolution from

millimeters down to atomic scale) of TME in human OS resected tissues. X-ray phase contrast micro-tomography (PhC micro-T) allowed a morphological characterization of bone architecture, thanks to X-rays diffraction (XRD), the crystalline structure of bone mineral component was depicted whereas micro-X-ray Absorption Spectroscopy (micro-XANES) allowed a molecular characterization at the atomic level (Fig. 3.1). In the present study, OS TME has been investigated in resected tissues of three different sub-types of osteosarcomas (osteoblastic, parosteal and periosteal) extracted from patients during elective surgery. Healthy bone was harvested from wide non-tumoral margins to perform an intra-subject comparison. As such, a deeper multi-scale characterization of different sub-types of OS TMEs holds great potential in the development of more effective and precise therapies with the goal of curing osteosarcoma with less acute and long-term side effects.



---

**Figure 3.1** Analysis of OS TME exploiting a multimodal and multiscale approach. A) Extraction site of the analyzed specimens. B) 3D reconstruction of a bone portion analyzed with PCT and tomographic slice in C). D) Histology slice stained with Mallory triple staining. E) XRFM map and corresponding micro-XANES spectra acquired from multiple points of interest (F). G) XRD diffractogram acquired in a POI containing bone tissue, H) intensity map of the specimen derived from 002 HA peak intensities.

## 3.1 Materials and Methods

### 3.1.1 Bone samples

Human bone samples were extracted after surgical intervention from bones of osteosarcoma patients at Istituto Ortopedico Rizzoli (IOR), Bologna, Italy. The resection was performed by an anatomopathologist from a tumoral area and a non-tumoral region and specimens were frozen at  $-20^{\circ}\text{C}$ . To better visualize collagen and bone minerals, Mallory triple staining was performed on a thin section of each sample. Detailed information on samples and subjects is provided in Table 3.1.

### 3.1.2 Phase-Contrast micro-Tomography (PhC micro-T)

The morphological characterization of osteosarcoma bone samples was performed by synchrotron-radiation X-ray phase-contrast micro-tomography (PhC micro-CT) at the SYRMEP (SYnchrotron Radiation for MEDical Physics) imaging beamline of Elettra synchrotron in Italy [93].

*Data acquisition.* Bone biopsies were enveloped frozen ( $-20^{\circ}\text{C}$ ) in parafilm and then mounted on the sample stage for the PhC micro-T acquisitions. The investigations were performed around 27 keV, by filtering the white beam with 1.5 mm thick Silicon (Si) plus 1 mm aluminum (Al) filter with energy storage ring operating at 2.0 GeV [150]. Phase-contrast measurements were achieved in line mode

---

with a propagation distance between 15 cm and 20 cm. The samples were rotated by 360 ° thanks to a rotating stage and projections were acquired with a 1° step using a sCMOS ORCA Flash 4.0 Hamamatsu camera (2048 pixels × 2048 pixels with physical pixel size 6.5 μm) equipped with a zoom system and coupled to a 17 μm thick GGG scintillator screen. All images were acquired with an exposure time of 200 ms and an effective pixel size that was varied between 0.9 μm and 2 μm. In addition to the sample radiographies, 20 flat fields and 20 dark fields were collected at the beginning of each tomographic measurement for the subsequent image processing step. Tomographic acquisitions were performed in different regions of the sample to account for intrasubject variability of tissue morphology. A volume of interest was acquired within each specimen with a  $2 \times 2 \times 2 \mu\text{m}^3$  voxels size, then, from 1 to 3 volumes were acquired in the same specimen with a  $0.9 \times 0.9 \times 0.9 \mu\text{m}^3$  voxels size. Volumes acquired at 2 μm step size (propagation distance equal to 20 cm) were used to analyze bone architecture (architecture analysis) whereas acquisitions performed at 0.9 μm step size (propagation distance equal to 15 cm) allowed a characterization of osteocytes lacunae (osteocytes' lacunae analysis).

*Data reconstruction.* Volumetric datasets were reconstructed using the open-source software SYRMEP Tomo-Project (STP) [151]. Specifically, after conventional flat-fielding, the projections were phase-retrieved using Paganin's algorithm with a  $\frac{\delta}{\beta}$  ratio equal to 50 [90], [91]. Then, virtual slices corresponding to the axial planes of the samples were recovered by Filtered Back Projection algorithm [89] combined with Shepp-Logan filter [152]. During the stage of processing, possible ring artefacts were attenuated using Rivers filter (width equal to 11) available in STP software.

*Data analysis.* Reconstructed slices were inspected with the open-source software Fiji [153]. 3D visualizations were realized using Amira (Thermo Fisher Scientific,



Waltham, MA, USA). A deeper analysis was carried out using the open-source software Fiji and BoneJ2 plugin to characterize bone volume and osteocytes lacunae [154]. Tomogram images (acquired at both  $2 \times 2 \mu\text{m}^2$  and  $0.9 \times 0.9 \mu\text{m}^2$  pixel size) were first normalized and then equalized (Fig. 3.2 A). Bone tissue and marrow were segmented by setting a threshold value and the bone-marrow was set to black (Fig. 3.2 B). Then, for  $0.9 \times 0.9 \mu\text{m}^2$  pixel size acquisitions, a binary image was derived by setting a further threshold to distinguish bone from osteocytes lacunae (as described in Fig. 3.2 C and D). The latter was used as input for BoneJ2 plugin in Fiji. BoneJ2 [154] is a collection of bone image analysis plugins and provides, among all the available options, a tool (Particle Analyzer) that allows to characterize osteocytes lacunae. Setup parameters and particles volumes limits were set according to [155]. The plugin outputs particles number, particles volumes (in pixels), their centroid's coordinates, moments of inertia and minor and major radius. Bone volume was calculated as the number of white pixels in the binary tomography image. Density of osteocytes lacunae (*Lc.density*) was derived as the ratio between the number of lacunae and the bone volume. To describe the shape of the lacunae *Lacuna stretch* (*Lc.St*) and *Lacuna oblateness* (*Lc.Ob*) were derived from the eigenvalues (moments of inertia) [156].

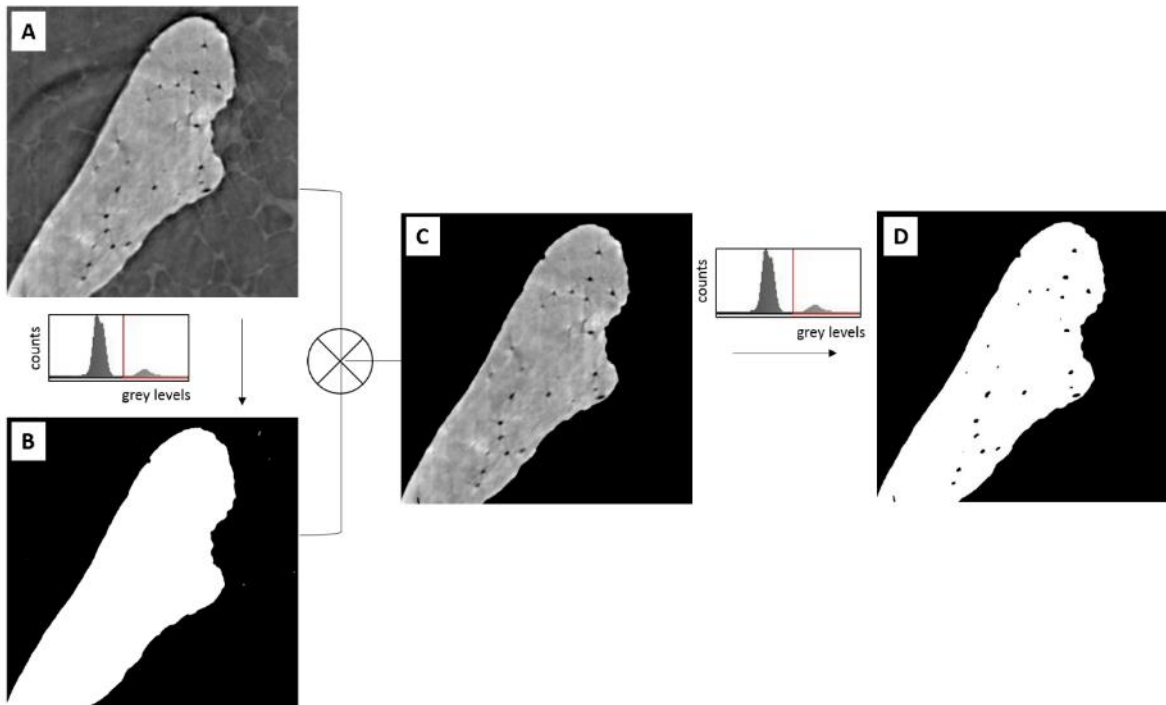
Lacunae can be represented as ellipsoids; thus, a shape tensor can be created for each lacuna according to [156]. This shape tensor provides the eigenvectors defining the ellipsoid axes and the corresponding eigenvalues ( $\lambda_1$ ,  $\lambda_2$  and  $\lambda_3$ ). The *Lc.St* describes the difference between the largest and the smallest eigenvalues of the shape tensor, compared to the largest one:

$$Lc.St = \frac{(\lambda_1 - \lambda_3)}{\lambda_1} \quad (3.1)$$

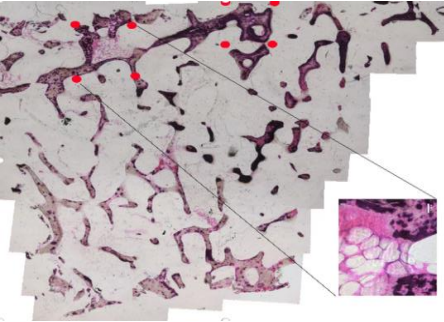
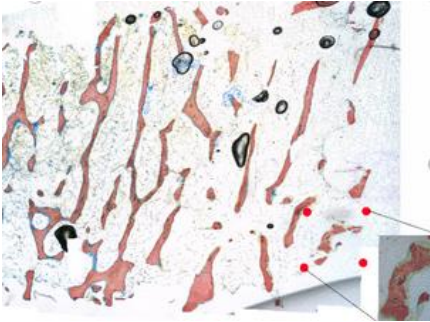
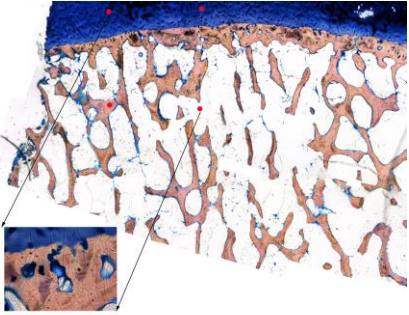
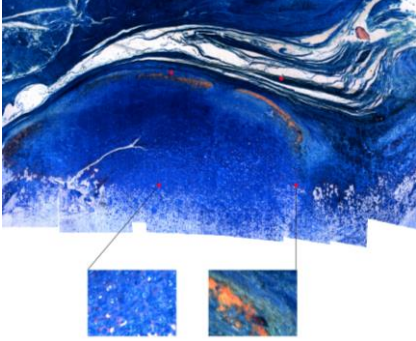
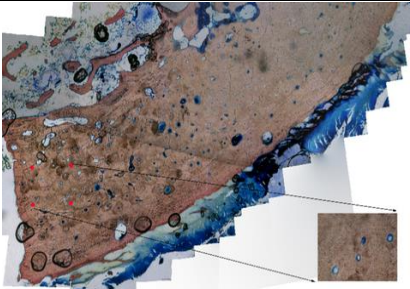
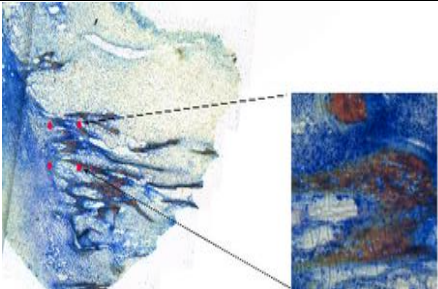
Lacunar stretch takes values in the range  $[0, 1]$ , where 0 corresponds to a perfectly spherical, and 1 to an infinitely stretched object. *Lc.Ob* quantifies the lacunar shape and is defined as:

$$Lc.Ob = 2 \frac{(\lambda_1 - \lambda_2)}{(\lambda_1 - \lambda_3)} \quad (3.2)$$

It provides information on the geometrical anisotropy of osteocyte lacunae, in addition to stretching and takes values in the range  $[-1, 1]$ , where  $-1$  corresponds to a perfect rod and 1 to a perfect plate.



**Figure 3.2** Tomographic acquisitions post-processing scheme performed with Fiji. In A) tomograms after equalization and normalization. A threshold is set to create a binary image that highlights bone tissue (B). After multiplication of images in A) and B), a bone image with black bone marrow background is obtained (C). A threshold is set to segment osteocyte's lacunae and a binary image is derived (D).

ID	CONTROL	TUMOR	SEX	LOCATION	TYPE	AGE	chemotherapy
1			F	distal femur	high grade OS	13	YES
3			F	distal femur	parosteal OS	62	NO
5			M	tibia	periosteal OS	15	NO

**Table 3.1** Information on the analyzed samples and subjects' generalities. Columns 'control' and 'tumoral' provide Mallory triple staining histologic images.

### 3.1.3 X-ray Diffraction (XRD)

X-ray diffraction measurements were performed at the XRD1 beamline of the ELETTRA synchrotron radiation facility in Trieste, Italy.

*Data acquisition.* The bone blocks harvested during surgery were embedded in polymethylmethacrylate resin after a fixation in formalin and dehydration with a graded ethanol series. Thin slices in the range of 50-70  $\mu\text{m}$  were taken off using a diamond saw and attached to a plastic microscope slide that was inserted in the sample holder. The sample detector distance was set to 200 mm, samples were hosted in an aluminium frame and mounted on a curved-slit goniometric head, which allowed aligning them perpendicularly to the direction of the beam. A Pilatus X-ray detector (DECTRIS Ltd. Baden, Switzerland) was employed to collect diffraction patterns and a double-crystal monochromator and mirrors system supplied a beam size of 200  $\mu\text{m}$  or 100  $\mu\text{m}$  diameter with a 12 keV energy. Bone samples were analyzed in 3 different experimental sessions at 3 different wavelengths around 1  $\text{\AA}$ . Samples were scanned in selected ROIs, with a step between 100  $\mu\text{m}$  and 200  $\mu\text{m}$ . For each acquisition step in the ROI, a diffractogram was generated allowing to depict the diffraction signal of hydroxyapatite (HA) present in bone trabeculae where detectable. The diffraction pattern of HA crystals appeared as a sharp ring in the diffractogram referred to as the ‘002’ lattice diffraction ring [149] (Fig. 3.3 A).

*Data processing.* The calibration and integration of the diffraction patterns over the whole detector area was performed by means of the software fit2d [157], exploiting a NIST Lab6 *as* reference. After radial integration performed through fit2d, diffraction patterns appear like spectra (Fig. 3.3 B, blue line). Reflection 002, corresponding to a d-spacing of 3.446  $\text{\AA}$ , proved to be intense and not overlapping with any other neighboring reflection. HA diffraction spectrum is modulated by the amorphous diffraction one, which is mainly due to the scattering from the plastic sample holder and epoxy resin employed to fix the

bone tissue biopsies (Fig 3.3 B, blue line). 002 and amorphous reflection peak (centered in  $d = 6.41 \text{ \AA}$ ) were analyzed performing a single peak fit through WINPLOTR software [158] in a user-defined  $2\theta$  range that was varied according to the wavelength of the incident beam. WINPLOTR allowed to derive peaks intensity, FWHM and  $d$  spacing of the considered peaks.

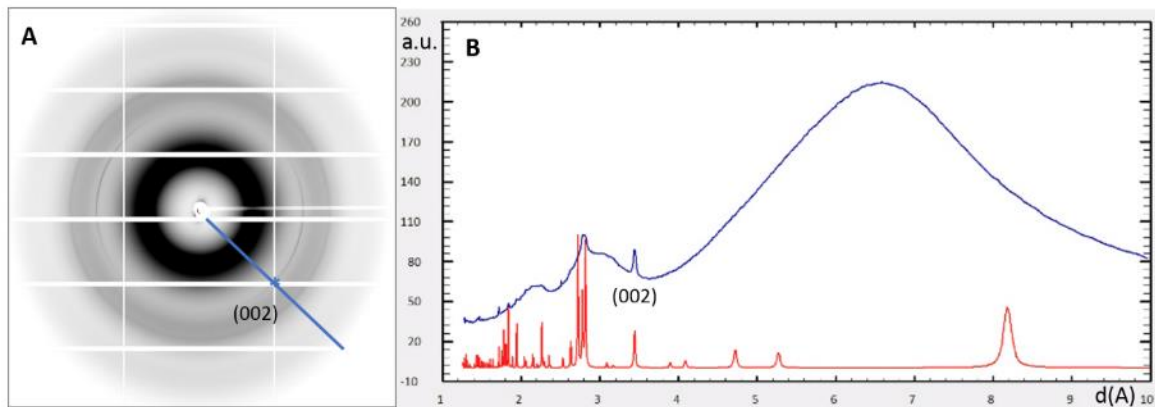


**Figure 3.3** A) Diffractogram from a region containing bone tissue. Through radial integration, a radial spectrum is derived (blue line in B) showing the main HA diffraction peaks. From the HA reference (red line in B), '002' peak can be easily individuated.

*Data analysis.* Intensity and FWHM derived from a specific 002 peak were normalized by the intensity and FWHM values of the corresponding amorphous peak. From peak intensities, it was possible to produce a map of the scanned area displaying the spatial location of the detected HA crystals and their peak intensity. An orderliness parameter ( $\rho$ ), defined as the ratio between the intensity and the FWHM of the 002 HA diffraction peak, was measured to describe sample's orderliness. By means of fit2d, an azimuthal  $360^\circ$  degrees integration on an angular region centered around 002 diffraction ring (one-degree step during integration) was performed. Azimuthal integration data preserve information about the preferential orientation of HA microcrystals. In the case of bone tissue, the mineral phase consists of HA, whose 002 direction (named c-axis) aligns along the collagen

---

fibril axis [1]. Therefore, the angular position of the most intense part of the diffraction peak at 002 was assumed as the direction of a vector with modulus proportional to the diffraction HA ring intensity. The generated vector field was superimposed to the intensity map providing complementary information about bone apatite c-axis orientation and HA abundance.

### **3.1.4 Micro X-ray Fluorescence Microscopy (micro-XRFM) and micro-X-ray Absorption Near Edge Spectroscopy (micro-XANES)**

2D micro-X-ray fluorescence microscopy (micro-XRFM) maps and single point micro-X-ray Absorption Near Edge Spectroscopy (micro-XANES) spectra were acquired at the ID21 beamline of the ESRF (Grenoble, France). The beamline provides a multi micro-analytical platform for the characterization of elements, species, molecular groups and crystalline structures in complex materials.

*Data acquisition.* The bone blocks were embedded in poly-methylmethacrylate resin after a fixation in formalin and dehydration with a graded ethanol series. Thin slices in the range of 90-100  $\mu\text{m}$  were taken off using a diamond saw and were inserted in the sample holder, clamped between two polymer films. Micro-fluorescence maps were acquired with a 4.999 keV energy, corresponding to the Ca K-edge energy region. Elements with absorption edges at lower energies were also subject to excitation and emission of fluorescence photons, generating maps of Ca, P and K simultaneously. Fluorescence maps were acquired with 5  $\mu\text{m}$  and 1  $\mu\text{m}$  step size to individuate bone tissue. XANES spectra were acquired at 1  $\mu\text{m}$  pixel size in Points of Interest (POIs) selected from the fluorescence maps, varying the incident beam energy between 4.02 keV and 4.17 keV with a 0.3 eV step. XANES spectra were acquired in both fluorescence and transmission modes based on the sample thickness. For thick bone sections with a low transmission signal, the

characterization was performed in fluorescence mode. Conversely, when bone was too thin, transmission mode was preferred.

*Data processing.* Fluorescence maps elemental peaks deconvolution was performed using the data analysis tool PyMCA [137], as detailed in Section 2.1.9. XANES spectra were normalized and analyzed with PyMCA and Orange [138].

## 3.2 Results

### 3.2.1 Phase-Contrast micro-Tomography (PhC micro-T)

Synchrotron PhC m-T is a nondestructive 3D imaging technique that allows the visualization of bone architecture, microdamage, morphology and micro-structure at high resolution [149]. At this level, microcracks [159], diffuse damage [160] and osteocytes' lacunae can be appreciated. PhC micro-T was exploited to characterize both osteocytes' lacunae and bone morphology at micrometric and submicrometric scale in three histologically different OS bone specimens (analyzed respectively at  $0.9 \times 0.9 \mu\text{m}^2$  and  $2 \times 2 \mu\text{m}^2$  pixel size). Results of architecture analysis and osteocyte's lacunae analysis are summarized in Tables 3.2 and 3.3.

ID	subject	BV/TV %	Mean Vol [ $\mu\text{m}^3$ ]	Lc.St	Lc.Ob	Lc.density [ $1/\mu\text{m}^3$ ]	# Lc
OS1	control	13.7	$257 \pm 140$	$0.647 \pm 0.150$	$0.585 \pm 0.357$	$1.25 \cdot 10^{-05}$	8696
OS1	tumor	9.6	$228 \pm 121$	$0.640 \pm 0.130$	$0.569 \pm 0.353$	$1.30 \cdot 10^{-05}$	6381
OS1	tumor	10.8	$248 \pm 132$	$0.637 \pm 0.133$	$0.522 \pm 0.377$	$1.27 \cdot 10^{-05}$	6969
OS1	tumor	8.4	$252 \pm 128$	$0.654 \pm 0.133$	$0.623 \pm 0.341$	$1.39 \cdot 10^{-05}$	5980
OS1	tumor	8.4	$225 \pm 111$	$0.674 \pm 0.129$	$0.649 \pm 0.330$	$1.38 \cdot 10^{-05}$	5934
OS3	control	13.3	$320 \pm 175$	$0.657 \pm 0.144$	$0.553 \pm 0.368$	$1.13 \cdot 10^{-05}$	7700
OS3	control	12.3	$258 \pm 148$	$0.646 \pm 0.149$	$0.538 \pm 0.379$	$9.11 \cdot 10^{-06}$	5860

OS3	tumor	38.3	$327 \pm 185$	$0.651 \pm 0.157$	$0.530 \pm 0.373$	$1.13 \cdot 10^{-05}$	22017
OS3	tumor	8.8	$215 \pm 131$	$0.630 \pm 0.150$	$0.476 \pm 0.378$	$6.30 \cdot 10^{-06}$	2811
OS3	tumor	3.0	$196 \pm 103$	$0.655 \pm 0.136$	$0.542 \pm 0.350$	$9.90 \cdot 10^{-06}$	1530
OS5	control	31.6	$226 \pm 122$	$0.689 \pm 0.142$	$0.641 \pm 0.346$	$7.04 \cdot 10^{-06}$	11269
OS5	control	48.7	$220 \pm 125$	$0.688 \pm 0.152$	$0.616 \pm 0.364$	$6.08 \cdot 10^{-06}$	15080
OS5	tumor	-	-	-	-	-	-

**Table 3.2** Characterization of osteocyte's lacunae in control and tumoral samples at  $0.9 \times 0.9 \times 0.9 \mu\text{m}^3$  voxel size. ID identifies the identification code associated to the subject, BV/TV indicates the percentage of bone present, Mean.Vol the mean volume of osteocytes' lacunae, Lc.St and Lc.Ob the stretching and oblateness of lacunae, Lc.density the density of lacunae derived from #Lc which represents the number of lacunae in the considered volume of interest.

ID	subject	BV/TV %	type	location	chemotherapy	age	sex
OS1	control	13.5	high grade OS	distal femur	yes	13	F
OS1	tumor	10.7	high grade OS	distal femur	yes	13	F
OS3	control	14.8	parosteal OS	distal femur	no	62	F
OS3	tumor	17.7	parosteal OS	distal femur	no	62	F
OS5	control	-	periosteal OS	tibia	no	15	M
OS5	tumor	-	periosteal OS	tibia	no	15	M

**Table 3.3** Characterization of bone architecture in control and tumoral samples at  $2 \times 2 \times 2 \mu\text{m}^3$  voxel size. ID identifies the code associated to the subject, BV/TV indicates the percentage of bone present. Other columns report the generalities of the subjects.

Sample OS1 was classified by histological analysis as a high-grade osteoblastic sarcoma. Fig. 3.4 and 3.5 provide morphological information on control and tumoral samples respectively. In A and B two tomographic slices ( $2 \mu\text{m}$  and  $0.9 \mu\text{m}$  thickness respectively) acquired at  $2 \times 2 \mu\text{m}^2$  and  $0.9 \times 0.9 \mu\text{m}^2$  pixel size at a distance of 20 cm and 15 cm respectively, are shown. In C and D, 3D reconstructions of the samples acquired at  $2 \mu\text{m}$



step and a zoom acquired at  $0.9 \mu\text{m}$  step can be observed. 2D tomographic images depicted bone microdamage in tumoral samples as indicated by the arrows in Fig. 3.6 (see Fig. 3.6 A and B for a comparison between control and tumoral tissues). Tumoral trabeculae appear less homogeneous and show borders disruption if compared to the control tissue. Osteocyte's lacunae analysis ( $0.9 \times 0.9 \times 0.9 \mu\text{m}^3$  voxel size) showed no significant differences in mean lacunar volumes and lacunar shape between control and tumoral samples. In tumoral bone, an increase in the lacunar density could be appreciated and was supported by the fact that in  $2 \times 2 \times 2 \mu\text{m}^3$  acquisitions a decrease in bone volume was present (see Table 3.2). The aforementioned observation is quantitatively supported by the comparison between Fig. 3.4 B and 3.5 B. 3D reconstructions reveal a reduction of trabecular thickness in the tumoral sample, suggestive of the potential stimulation of osteoclast's osteolytic activity by the high-grade OS.

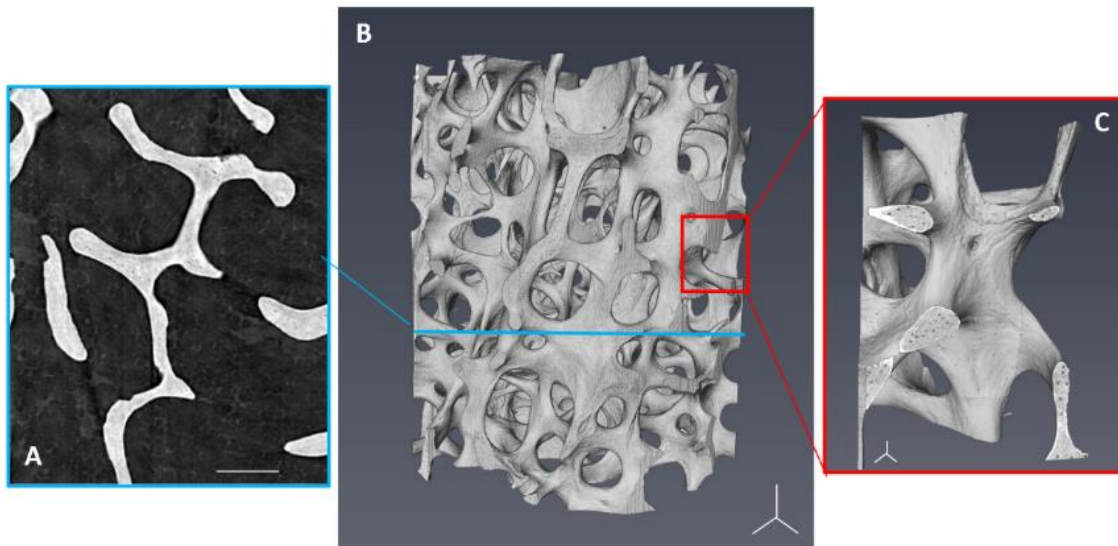


**Figure 3.4** OS1 control - A) tomographic slice acquired at  $2 \times 2 \mu\text{m}^2$  pixel size (scale bar  $500 \mu\text{m}$ ). In B) 3D reconstructions of the samples acquired at  $2 \times 2 \times 2 \mu\text{m}^3$  voxel size (scale bar  $0.5 \text{ mm}$ ) and in C) a zoom acquired at  $0.9 \times 0.9 \times 0.9 \mu\text{m}^3$  voxel size (scale bar  $0.25 \text{ mm}$ ).

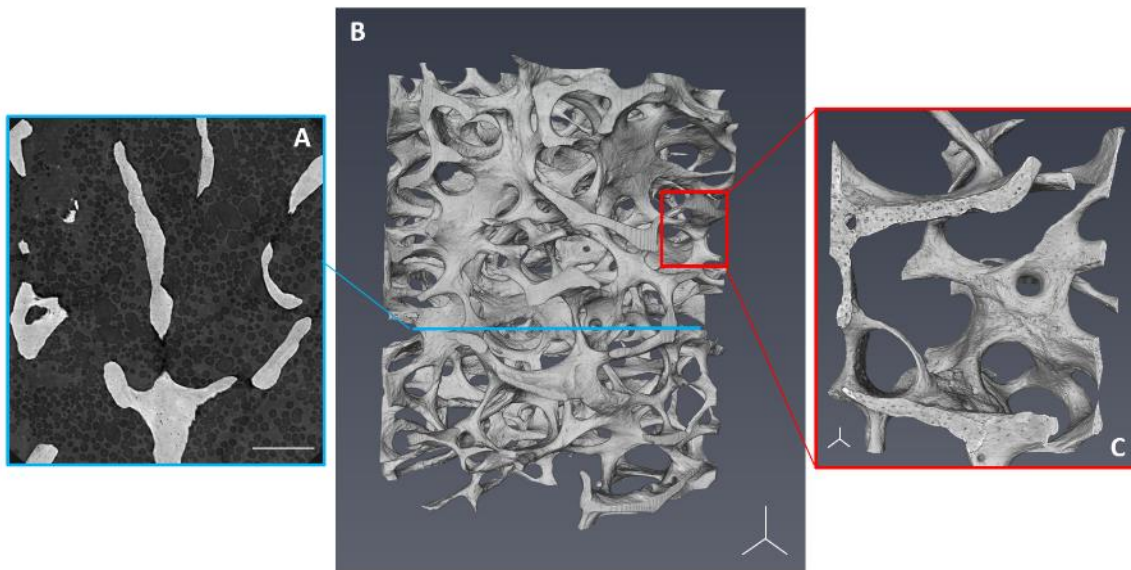


**Figure 3.5** OS1 tumor - A) tomographic slice acquired at  $2 \times 2 \mu\text{m}^2$  pixel size (scale bar  $500 \mu\text{m}$ ). In B) 3D reconstructions of the samples acquired at  $2 \times 2 \times 2 \mu\text{m}^3$  voxel size (scale bar  $0.5 \text{ mm}$ ) and in C) a zoom acquired at  $0.9 \times 0.9 \times 0.9 \mu\text{m}^3$  voxel size (scale bar  $0.25 \text{ mm}$ ).

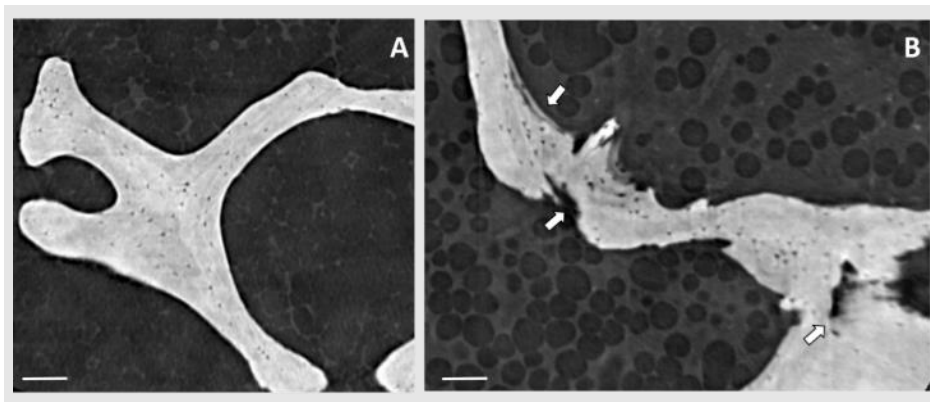


**Figure 3.6** 2D tomographic images acquired from OS1, control (A) and tumoral (B) respectively. Bone microdamage in tumoral samples is indicated by arrows. Scale bar is  $100 \mu\text{m}$ .

Sample OS3 was classified by histological analysis as a parosteal osteosarcoma. Fig. 3.7 and 3.8 provide morphological information on control and tumoral samples respectively. The tumoral sample appeared to be very inhomogeneous from a morphological point of

view (Fig. 3.8 C and D). Architecture analysis ( $2 \times 2 \times 2 \mu\text{m}^3$  voxel size) revealed that the parosteal tumor infiltrated the cortical bone and, in the medullary cavity of the tumoral tissue, osteoclasts' osteolytic action could be appreciated (Fig. 3.8 C).  $0.9 \times 0.9 \times 0.9 \mu\text{m}^3$  voxel size acquisitions were performed in different regions of the specimen to account for the morphological variability previously described (Fig. 3.8 D). Osteocyte's lacunae analysis showed no significant differences in mean lacunar volumes and lacunar shape between control and tumoral samples, but bone volume percentage and lacunar density strongly varied among the different areas of the tumor.

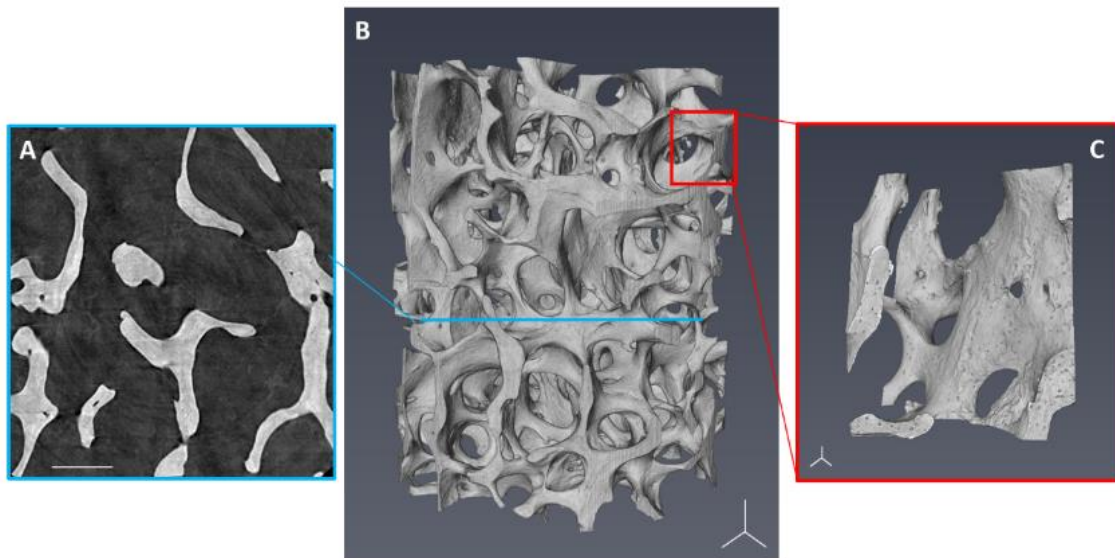


**Figure 3.7** OS3 control - A) tomographic slice acquired at  $2 \times 2 \mu\text{m}^2$  pixel size (scale bar  $500 \mu\text{m}$ ). In B) 3D reconstructions of the samples acquired at  $2 \times 2 \times 2 \mu\text{m}^3$  voxel size (scale bar  $0.5 \text{ mm}$ ) and in C) a zoom acquired at  $0.9 \times 0.9 \times 0.9 \mu\text{m}^3$  voxel size (scale bar  $0.25 \text{ mm}$ ).

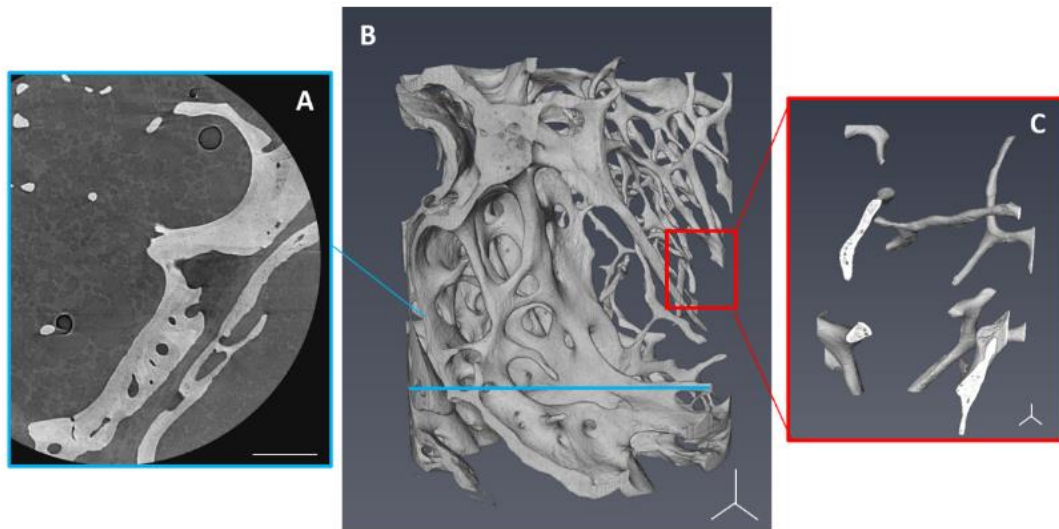


**Figure 3.8** OS3 tumor - A) tomographic slice acquired at  $2 \times 2 \mu\text{m}^2$  pixel size (scale bar  $500 \mu\text{m}$ ). In B) 3D reconstructions of the samples acquired at  $2 \times 2 \times 2 \mu\text{m}^3$  voxel size (scale bar  $0.5 \text{ mm}$ ) and in C) a zoom acquired at  $0.9 \times 0.9 \times 0.9 \mu\text{m}^3$  voxel size (scale bar  $0.25 \text{ mm}$ ).

Sample OS5 was classified by histological analysis as a periosteal osteosarcoma. Fig. 3.9 and 3.10 provide morphological information on control and tumoral samples respectively. The tumoral sample appeared to be very poor in its mineral component mainly constituted by hypo-mineralized spicules showing low phase-contrast signal with respect to control tissue (Figure 3.9 A and B). In these bone formations, osteocytes lacunae could not be appreciated and characterized due to the low contrast between lacunae and bony tissue. On the other side, control bone sample was extracted from the tibial cortical area and could not be compared with other subjects' control samples derived from trabecular femur bone.

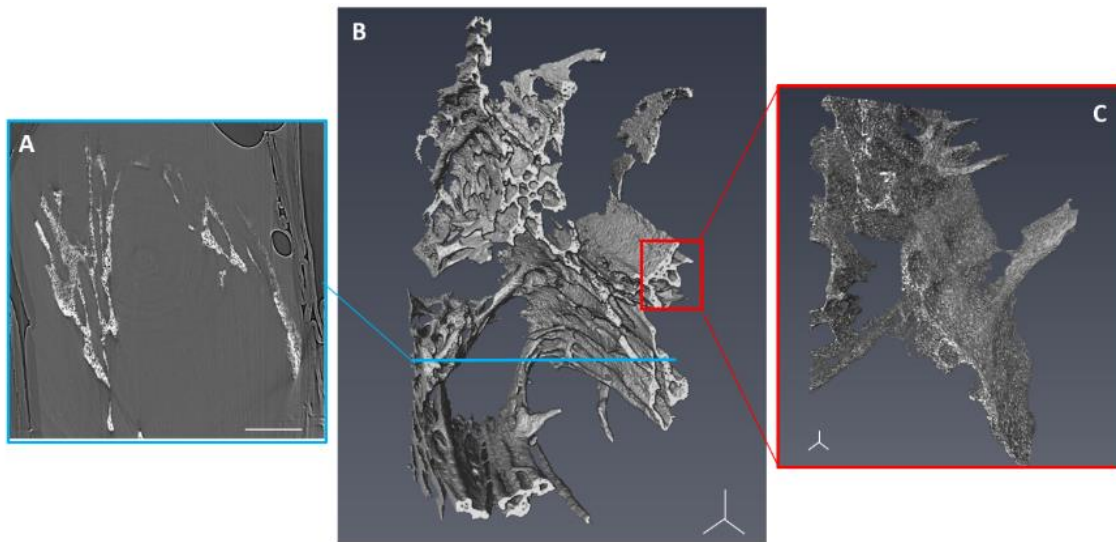


**Figure 3.9** OS5 tumor - A) tomographic slice acquired at  $2 \times 2 \mu\text{m}^2$  pixel size (scale bar  $500 \mu\text{m}$ ). In B) 3D reconstructions of the samples acquired at  $2 \times 2 \times 2 \mu\text{m}^3$  voxel size (scale bar  $0.5 \text{ mm}$ ) and in C) a zoom acquired at  $0.9 \times 0.9 \times 0.9 \mu\text{m}^3$  voxel size (scale bar  $0.25 \text{ mm}$ ).

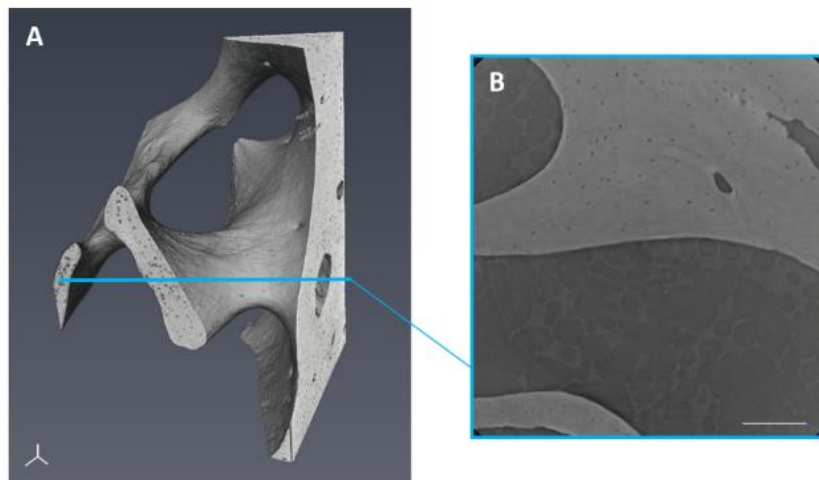


**Figure 3.10** OS5 control - A) a 3D reconstruction of the sample ( $0.9 \times 0.9 \times 0.9 \mu\text{m}^3$  voxel size) (scale bar  $0.25 \text{ mm}$ ) and in B) a tomographic slice acquired at  $0.9 \times 0.9 \mu\text{m}^2$  (scale bar  $200 \mu\text{m}$ ).

### **3.2.2 X-ray Diffraction and micro-X-ray Absorption Near Edge Spectroscopy (micro-XANES)**

The atomic-level organization of osteosarcoma has not been fully elucidated. Therefore, both XRD and micro-XANES could provide new insights into the structure and composition of bone mineral apatite. XRD is one of the most powerful techniques for the analysis of long-range order materials, offering information on the crystalline phase. However, bone and bone-like tissues consist of short- and long-range order minerals with some amorphous material. In this context, XANES technique could be beneficial to overcome these limitations and determine the mineral composition of bone tumoral tissue, particularly when dealing with the amorphous component and short-range order variations that could be undetected by XRD [161]. Thanks to XRD it was possible to detect the presence of HA minerals in the three different osteosarcoma sub-types analyzed. The integrated intensity maps of the 002 HA peak normalized by the intensity of the amorphous peak are reported in Fig. 3.11-3.12-3.13. Intensity values vary proportionally with the amount of HA minerals detected in the bone tissue section analyzed. In OS1 sample (intensity maps in Fig. 3.11 A and B), both control and tumoral tissues exhibit the typical bone trabecular structure, previously observed in the tomographic and histological acquisitions (Fig. 3.4 and 3.5, Table 3.1).



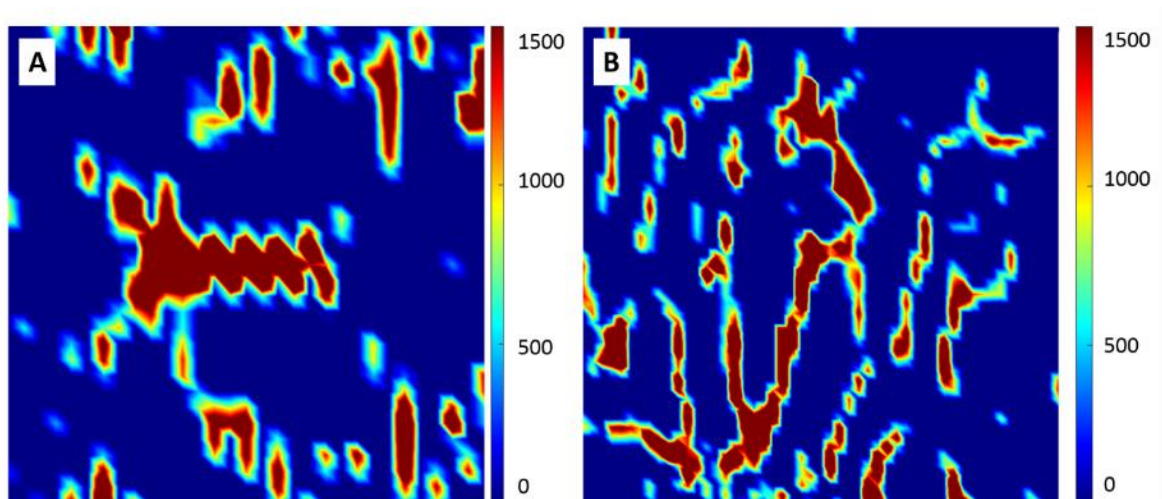


**Figure 3.11** Intensity maps representing 002 HA diffraction peak integrated intensity. A) shows OS1 control map (ROI 3mmx3mm) and B) OS1 tumoral sample (ROI 5mmx5mm). The color bar represents the integrated intensity of 002 HA diffraction peak.

Remarkably, both trabecular and cortical bone were analyzed in the OS3 control samples. In contrast, the OS3 tumoral sample exhibited a small portion of mineralized tissue, consistently with observations from the histological examination (Table 3.1, Fig. 3.12 A and B). The low mineralized tissue portion probably belongs to the medullary cavity of the tumoral tissue where osteoclasts' osteolytic action is most visible.

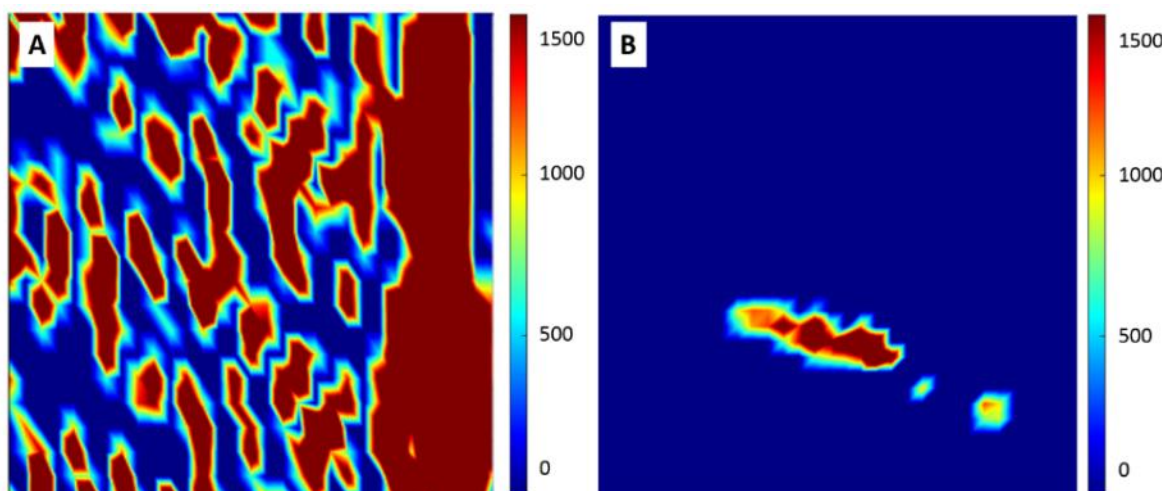


**Figure 3.12** Intensity maps representing 002 HA diffraction peak integrated intensity. A) shows OS3 control map (ROI 2mmx2mm) and B) OS3 tumoral sample (ROI 3mmx3mm). The color bar represents the integrated intensity of 002 HA diffraction peak.

OS5 control sample showed both trabecular and cortical tissue whereas OS5 tumoral sample exhibited small portions of low mineralized bone (Fig. 3.13 A and B), as previously highlighted in histological images and tomography (Table 3.1). The presence of bone spicules with low concentration of HA minerals can be attributed to an anomalous and defective orchestration of bone cells action (previously shown in Fig. 3.9 B and C).

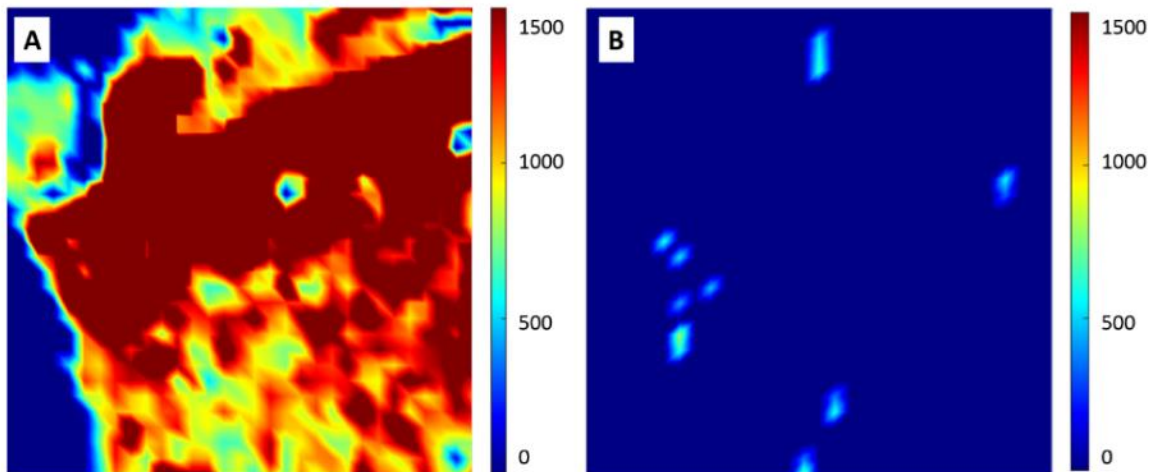


**Figure 3.13** Intensity maps representing 002 HA diffraction peak integrated intensity. A) shows OS5 control map (ROI 3mmx3mm) and B) OS5 tumoral sample (ROI 3mmx3mm). The color bar represents the integrated intensity of 002 HA diffraction peak.

To further characterize the samples, we defined an orderliness parameter ( $\rho$ ) determined by the ratio between intensity and FWHM of the 002 HA diffraction peak and we represented it as a function of the normalized intensity (Fig. 3.14-3.16-3.18). Two distributions can be clearly appreciated: a yellow-orange one and a blue-red one. For a fixed-low intensity value, corresponding to a low content of bone apatite minerals in the tissue,  $\rho$  shows low values belonging to the blue-red distribution and higher values in the



---

yellow-orange one. Respectively, high  $\rho$  values depend on small FWHM which is characteristic of ordered crystalline materials while low  $\rho$  values correspond to high FWHM indicating less ordered HA. As intensity increases,  $\rho$  values from the blue-red cluster correspond to higher intensities of 002 peak having almost constant FWHM values, indicating a higher concentration of bone mineral crystals. As diffractograms were acquired from multiple slices of different bone areas, we decided to characterize the distribution of each population in the  $\rho$ -intensity space to compare results derived from both control and tumoral samples in the same OS sub-type. In the blue-red distribution (Fig. 3.14-3.16-3.18), 50% of the  $\rho$  corresponding to increasing low intensities were highlighted in blue while the remaining 50% with higher intensity values in red. Tumoral samples are represented by asterisks and controls by squares. By observing Fig. 3.14 and 3.16, it is possible to notice that bone tumoral  $\rho$  is more shifted towards low intensity values in OS1 and OS3, indicating either higher FWHM amplitudes and therefore less ordered HA minerals with respect to controls or lower intensity values which are indicative of less abundant HA minerals. In OS5 (Fig. 3.18), it is possible to notice that bone tumoral  $\rho$  belongs mainly to the yellow-orange cluster which is representative of more ordered HA crystals despite being generally scarcely concentrated. A small distribution of  $\rho$  values can be appreciated in the low-ordered and low-mineral content region of the blue-red cluster. The  $\rho$  parameter was then represented as a function of bone apatite interplanar distance (Fig. 3.15-3.17-3.19) to appreciate the interplanar distance distribution in all the analyzed conditions. As interplanar distance has been derived from 002 HA peak analysis, it provides information on bone apatite c-axis length. In OS1, data from control and tumoral sample show comparable distributions and medians (respectively blue and red line in Fig. 3.15) underlining a similar interplanar distance length in bone apatite minerals ( $d_{CTRL} = 3.443 \pm 0.002 \text{ \AA}$ ,  $d_{TUM} = 3.443 \pm 0.048 \text{ \AA}$ ). In OS3 (Fig. 3.17), it is possible to

appreciate that data from control and tumoral sample have different distributions and medians (represented by the blue and red line respectively): the two samples show a different  $d$  which is representative of the bone apatite interplanar distance along the HA  $c$ -axis ( $d_{CTRL} = 3.445 \pm 0.024 \text{ \AA}$ ,  $d_{TUM} = 3.443 \pm 0.006 \text{ \AA}$ ), shrunk in the tumoral specimen. Interestingly, the tumoral distribution shows a bimodal shape suggesting the presence of two bone apatite minerals having different  $c$ -axis lengths. In sample OS5 (Fig. 3.19), tumoral bone apatite minerals exhibit a shrunk interplanar distance with respect to control ( $d_{CTRL} = 3.444 \pm 0.123 \text{ \AA}$ ,  $d_{TUM} = 3.438 \pm 0.030 \text{ \AA}$ ).

Preliminary integrated intensity maps indicating the orientation of HA  $c$ -axis were derived through an azimuthal analysis of the diffraction patterns. Nevertheless, to perform a comparison between control and tumoral sample, the analyzed bone tissues must be consistent.

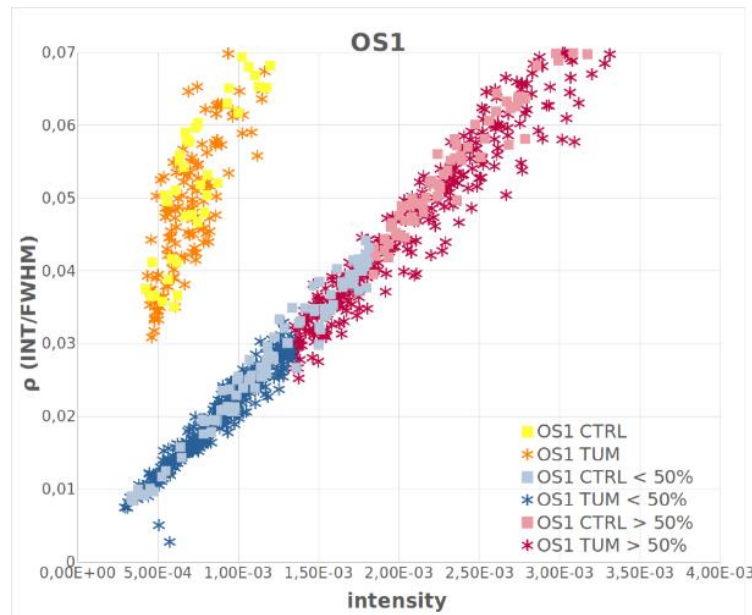


**Figure 3.14** Orderliness parameter as a function of 002 HA peak intensity for OS1 control (squares) and tumor (asterisks).

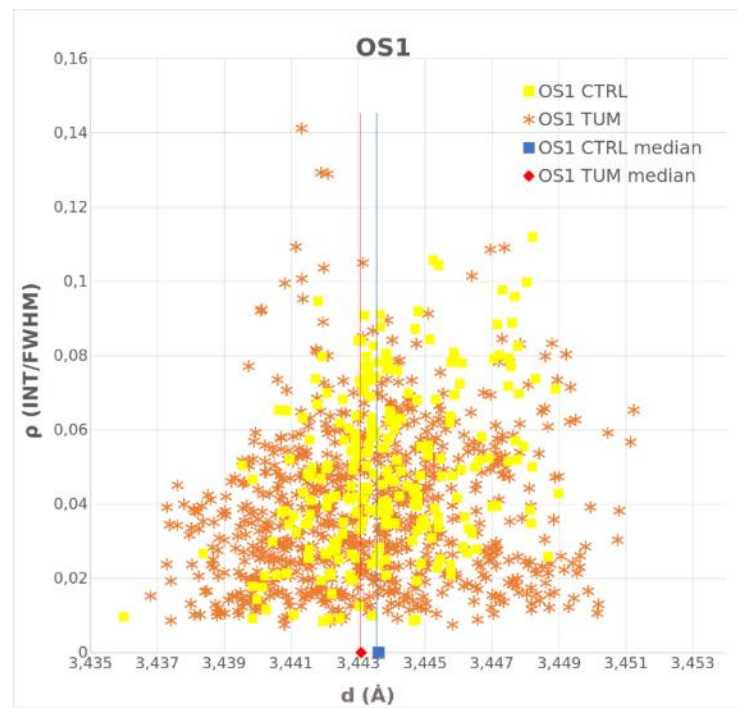


**Figure 3.15** Orderliness parameter as a function of 002 HA interplanar distance ( $d$ ) for OS1 control (yellow) and tumor (orange). Red and blue lines represent the medians calculated from the control and tumoral distributions of  $d$ .

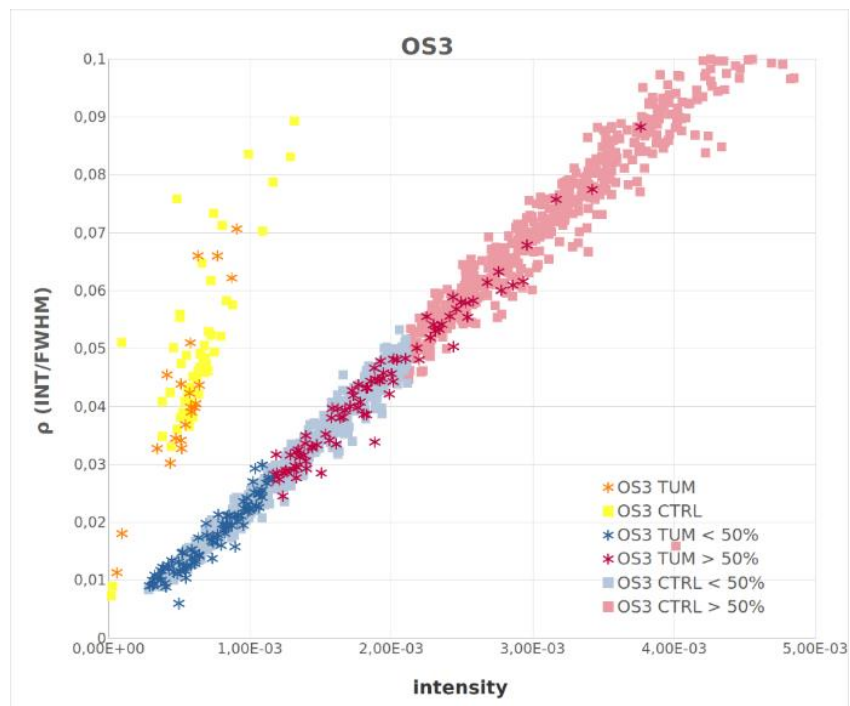


**Figure 3.16** Orderliness parameter as a function of 002 HA peak intensity for OS3 control (squares) and tumor (stars).

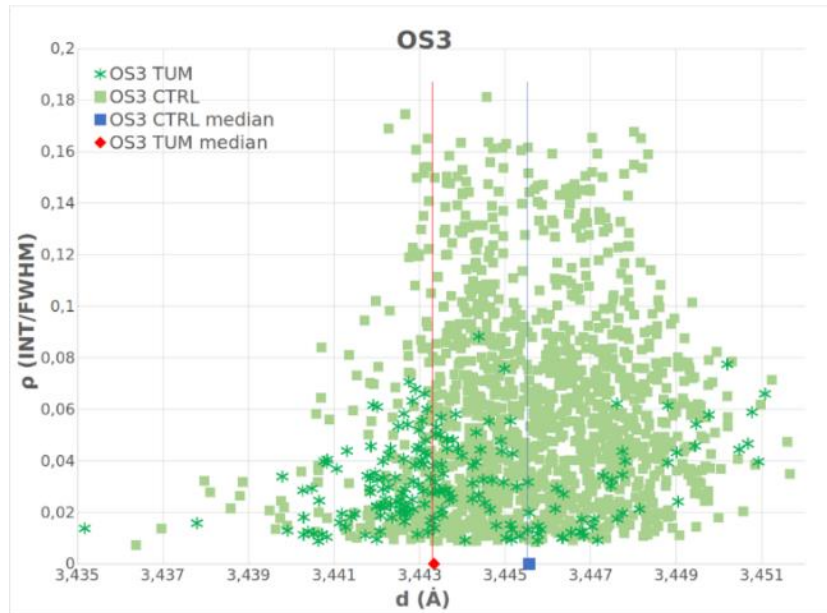


**Figure 3.17** Orderliness parameter as a function of 002 HA interplanar distance ( $d$ ) for OS3 control (light green) and tumor (green). Red and blue lines represent the medians calculated from the control and tumoral distributions of  $d$ .

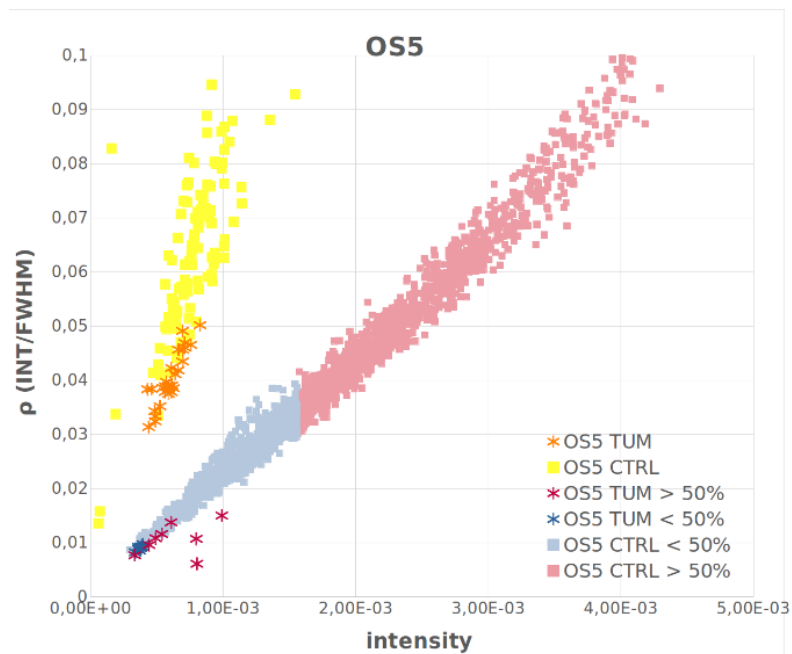


**Figure 3.18** Orderliness parameter as a function of 002 HA peak intensity for OS5 control (dots) and tumor (stars).

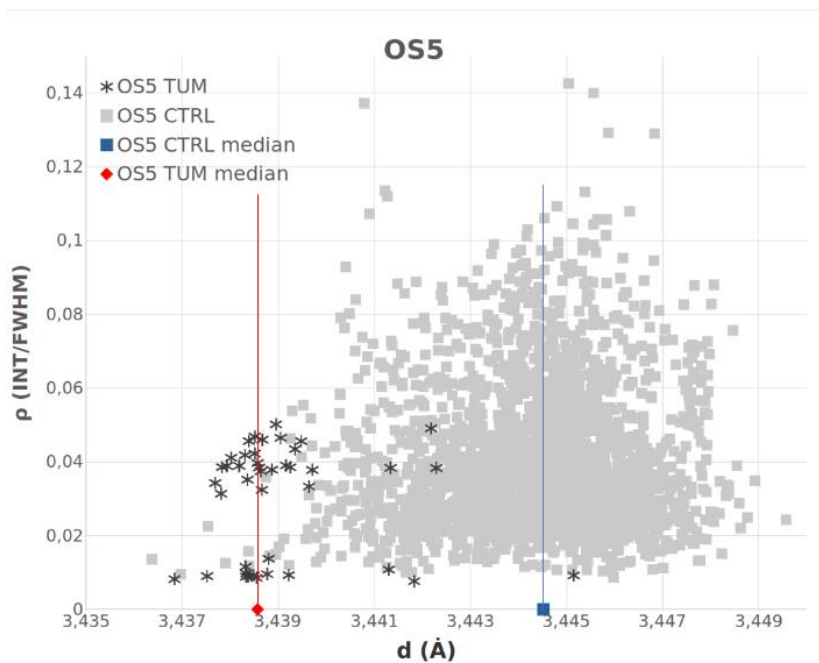


**Figure 3.19** Orderliness parameter as a function of 002 HA interplanar distance ( $d$ ) for OS5 control (grey) and tumor (black). Red and blue lines represent the medians calculated from the control and tumor distributions of  $d$ .

Thanks to micro-XRFM at 4.99 keV it was possible to individuate bone tissue in all samples and acquire micro-XANES Ca-K edge spectra in selected points of interest (POIs). Bone tissue showed in both OS1 control and tumor samples spectra exhibiting the same spectral features of HA reference spectrum (Fig. 3.20 and 3.21).

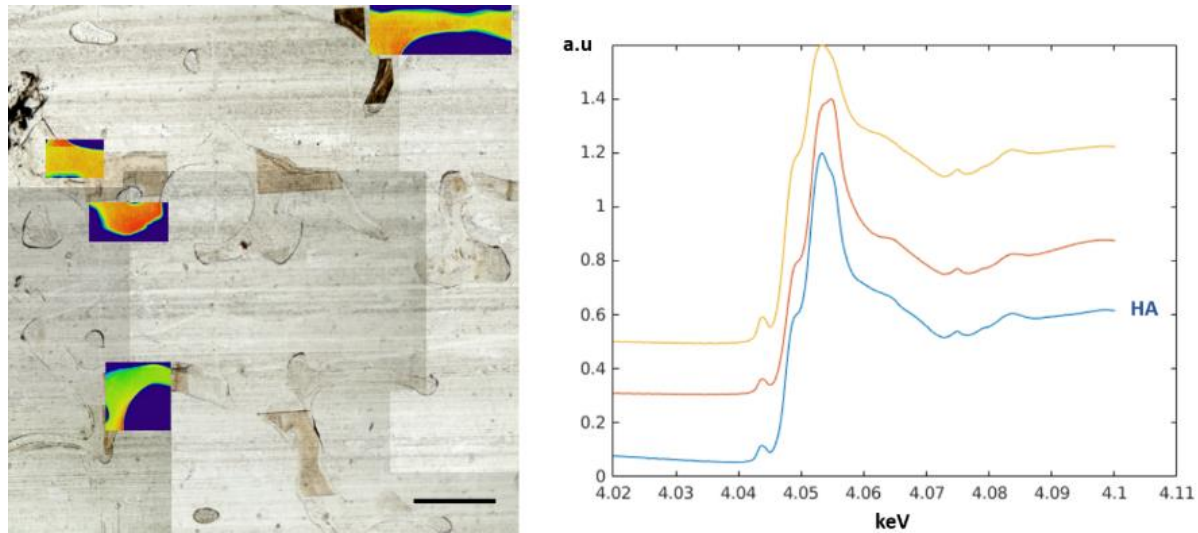


**Figure 3.20** OS1 control – Left: calcium XRFM acquired at 4.99 keV with 5  $\mu\text{m}$  step size. Right: XANES spectra at Ca K-edge from POIs of fluorescence maps, the bottom spectrum shows the HA reference. Scale bar is 1mm.

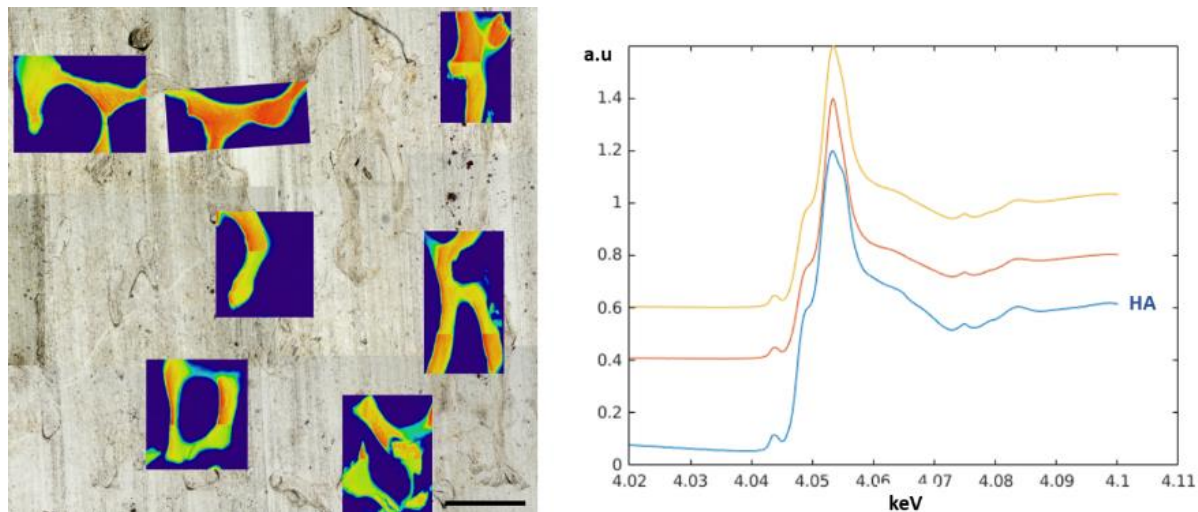


**Figure 3.21** OS1 tumor – Left: calcium XRFM acquired at 4.66 keV with 5  $\mu\text{m}$  step size. Right: XANES spectra at Ca K-edge from POIs of fluorescence maps, the bottom spectrum shows the HA reference. Scale bar is 1mm.

OS3 control sample showed spectra similar to HA reference spectrum (Fig. 3.22). On the other side, the tumoral specimen provided a different scenario with respect to the control: only an area of bone tissue could be spotted matching HA reference spectrum



(Fig. 3.23). By acquiring spectra from other regions of the sample, calcium compounds could be individuated (see RGB merged fluorescence maps in Fig. 3.23). In these regions, XANES spectra showed spectral features different from HA reference by exhibiting a shoulder after the white region and lacking the shoulder typical of HA at 4.049 keV before the white region (yellow spectrum in Fig. 3.23).

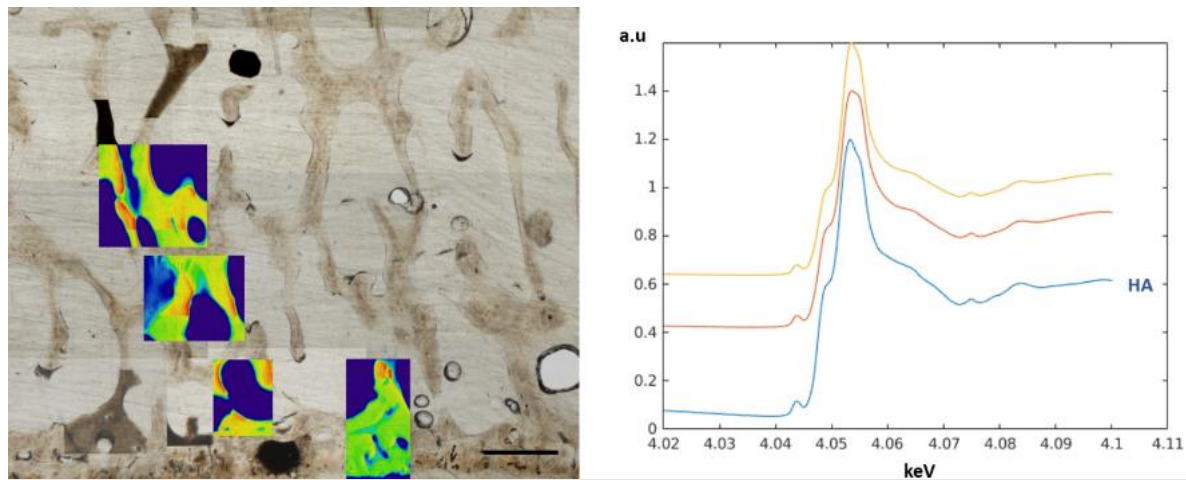


**Figure 3.22** OS3 control – Left: calcium XRFM acquired at 4.66 keV with 5  $\mu\text{m}$  step size. Right: XANES spectra at Ca K-edge from POIs of fluorescence maps, the bottom spectrum shows the HA reference. Scale bar is 1mm.

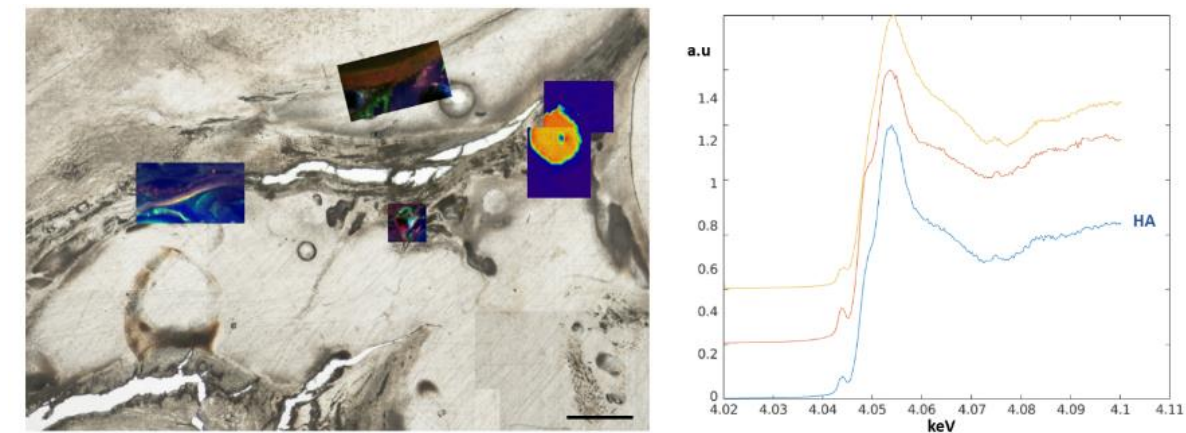


**Figure 3.23** OS3 tumor – Left: calcium XRFM acquired at 4.66 keV with 5  $\mu\text{m}$  step size. Right: XANES spectra at Ca K-edge from POIs of fluorescence maps, the bottom spectrum shows the HA reference. Scale bar is 1mm.

In OS5, control bone tissue showed spectra similar to HA reference spectrum (Fig. 3.24). The tumoral sample provided XANES spectra matching the spectrum of HA reference (Fig. 3.25) and a majority exhibiting a shoulder after the white region and lacking a shoulder at 4.049 keV before the white region as observed for OS3 tumoral sample (yellow spectrum in Fig.3.25).

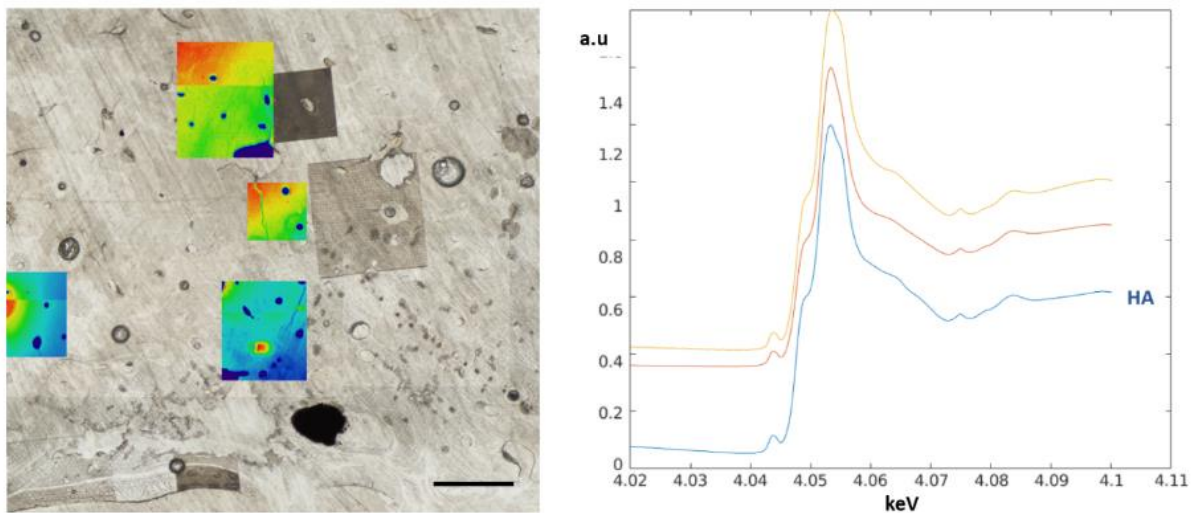


**Figure 3.24** OS5 control – Left: calcium XRFM acquired at 4.66 keV with 5  $\mu\text{m}$  step size. Right: XANES spectra at Ca K-edge from POIs of fluorescence maps, the bottom spectrum shows the HA reference. Scale bar is 1mm.



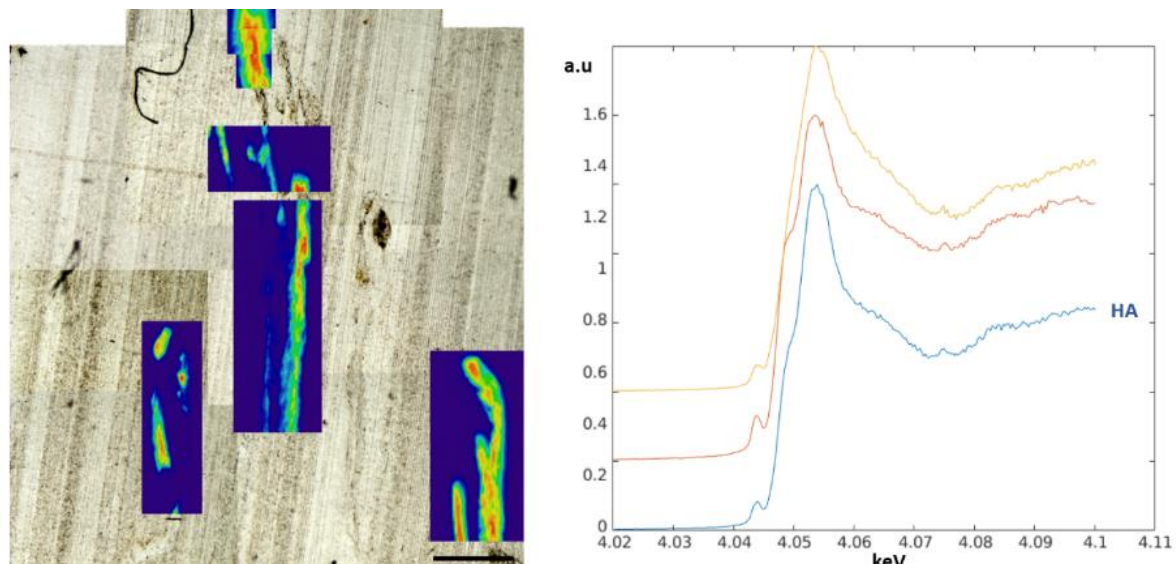


**Figure 3.25** OS5 tumor – Left: calcium XRFM acquired at 4.66 keV with 5  $\mu\text{m}$  step size. Right: XANES spectra at Ca K-edge from POIs of fluorescence maps, the bottom spectrum shows the HA reference. Scale bar is 1mm.

### 3.2.3 PCA analysis on micro-XANES Ca K-edge spectra s

To further characterize the spectroscopic data, we used PCA analysis to better distinguish the XANES spectra acquired for each experimental condition. Among the acquired spectra, reference spectra from HA and calcite were considered too. The score PC1 vs PC2 scatter plot can be appreciated in Fig. 3.26 A, and shows a clear division of the spectra in two clusters highlighting a good separation between control and tumoral samples (light-blue and red clusters respectively).

The diagonal dispersion visible in the two clusters is linked to the acquisition mode (fluorescence spectra more on the left, transmission ones more on the right) and to the height of the white line of the spectrum (Fig. 3.26 B). The latter can be distorted by saturation due to too low transmission signal or to self-absorption effects depending on sample's thickness. POIs in the top cloud display spectra looking close to HA (Fig. 3.26 light-blue cluster and average light-blue spectrum in Fig.3.26 B). POIs in the lower cluster

belong to tumoral bone. The spectra seem less structured, probably indicating a less crystallized phase that could represent intermediate stages of the biomineralization process (Fig. 3.26 red cluster and average red spectrum in Fig.3.26 B). The small group of POIs on the lower right (Fig. 3.26 A, green cluster) has a different spectrum (Fig. 3.26 B, green average spectrum) that could not be matched with the available references.

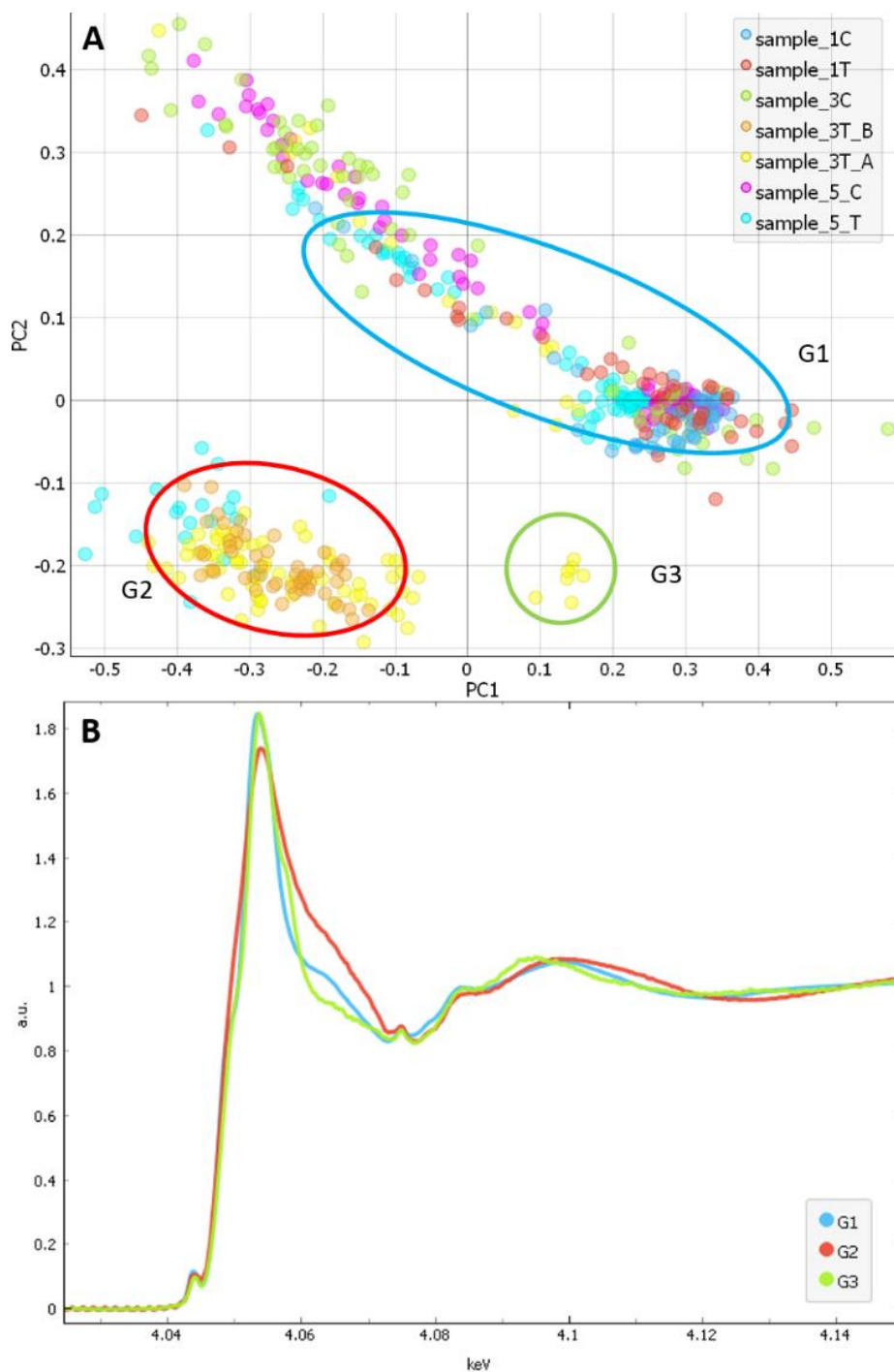


**Figure 3.26** A) PCA score PC1 vs PC2 scatter plot of the XANES spectra acquired from samples 1, 3 and 5 control (light-blue cluster) and tumoral (red cluster). B) Average XANES spectra from the clusters in A).

### 3.3 Discussion and Future Perspectives

At present, OS literature concerning the characterization of OS TME in different tumor subtypes is relatively scarce. Indeed, this scarcity can be partly attributed to the fact that OS is a rare disease affecting a low percentage of subjects and partly to the challenges associated to the availability of bone tissue biopsies for research purposes. When obtained, samples may be insufficiently large for a multimodal characterization requiring different samples preparations. Additionally, collecting different OS subtypes specimens that can be compared considering factors such as age, sex, tumor type and extraction site is non-trivial. In this context, an intra-subject characterization of different OS subtypes was performed using a multimodal and multiscale approach. A more comprehensive understanding of OS subtype characteristics was obtained by comparing tumoral material with control tissue extracted from the same subject. The application of a multiscale approach with combined synchrotron x-ray techniques has revealed that the mineralized tissue formed by various osteosarcoma subtypes can be distinguished from normal bone, not only in morphology but also in mineral and chemical composition [1].

In recent years, there has been growing interest in depicting the spatial characteristics of osteocytes to elucidate their relationship with physiological and pathological changes in bone tissue. While osteocytes can change the morphology of lacunae over time [155], the spatial density of lacunae is likely more stable. Therefore, both shape and density may reflect conditions from differing temporal scales and bone pathologies, and a morphological characterization of bone trabecular structure and volume could give information on bone tissue remodeling and homeostasis.

The *ex vivo* analysis of human osteosarcomas samples through PhC micro-T allowed to characterize tumor morphology and provided detailed information about the 3D bone structure [149], [162] and osteocytes lacunae. In clinical practice, dual-energy X-ray absorptiometry (DXA) is used to characterize bone tissue, but it does not fully depict the

---

3D complex hierarchical structure of bone with the high spatial resolution offered by synchrotron-radiation (SR) techniques. However, despite the increased spatial resolution provided by SR acquisitions, the field of view is generally reduced. Therefore, while more detailed spatial information is obtained, it is unclear how representative this information is of the isolated tumoral bone [162]. An example of this limitation is evident in OS3 tumoral sample (Fig. 3.8), which shows a strong morphological inhomogeneity. The tumor infiltrates the cortical tissue until the trabecular region, where tissue osteolysis occurs. Consequently, depending on the specimen's area studied, there is a substantial variation of the morphological parameters while those characterizing osteocytes lacunae remain mainly unchanged. On the other hand, conducting a comprehensive study of lacunar density and morphology necessitates a large volume of interest to obtain representative information. Further explorations of the variation in lacunae shape and density by extracting multiple samples from different regions of the tumor could enhance the understanding of the relationship between osteocytes population and bone sarcomas. In addition, a more accurate morphological characterization of the tumoral tissue could be achieved, considering that osteosarcoma shows a rich variety of tissues, including edema, inflammation, necrotic tissue (especially after chemotherapy), and proliferating bone tissue [109].

Utilizing PCA analysis, it was observed that spectra from control and tumoral samples formed two distinct clusters. All control samples and the tumoral sample OS1 exhibited spectra aligning with the HA reference spectrum, indicating the presence of a healthy and physiological bone tissue condition. Micro-XANES spectra from sample OS1 tumoral, likely represent the positive effects of the pre-surgical neoadjuvant chemotherapy administered to the patient. Conversely, tumoral samples displayed a few spectra belonging to the control cluster, but the majority exhibited different spectral features

---

compared to the HA reference (Fig. 3.26 A). These spectra appeared less structured, suggesting the presence of a less crystallized mineral phase indicative of intermediate biomineralization stages. Zanghellini et al. [1] have shown, thanks to SR micro-diffraction, that HA c-axis undergoes shrinkage in OS bone tissues. Considering a prevalence of B-type substitution in healthy bone, this shrinkage might be attributed to a lower carbonate substitution in HA. The lower carbonate levels could be explained by the higher tissue turnover rate in tumors, leading to the presence of less mature bone. This supports the earlier speculation that tumoral XANES spectra are related to a less crystallized mineral phase of HA. Interestingly, in literature, the presence of carbonate has been identified as an indicator of the malignancy of calcifications in breast tissue. Specifically, benign HA lesions were found to have higher carbonate levels than malignant ones [19], suggesting their potential diagnostic utility. In the context of OS, the presence of less mature bone could serve as biomarker of tumoral activity and could be fundamental to study the efficacy of neoadjuvant chemotherapies before surgical intervention.

X-ray diffraction investigations provided a fingerprint of bone mineral phase. Bone is a dynamic living tissue subject to a constant remodeling throughout life and OS can compromise this process. Through the characterization of 002 HA diffraction peaks and the derivation of their intensity and FWHM, we observed that tumoral HA is both less abundant and less ordered, compared to minerals constituting control samples. Peak intensity is directly proportional to the amount of minerals while peak width (FWHM) broadening is associated to defects in crystals structure and inhomogeneous composition. By studying bone apatite minerals interplanar distance, we observed a shrinkage of the parameter in tumoral samples that didn't undergo neoadjuvant chemotherapy. As previously described, a shrinkage of HA c-axis might be linked to high tissue turnover typical of tumoral conditions.

To better investigate the nature of osteosarcoma bone tissue, we plan to conduct SAXS/WAXS (Small-Angle X-ray Scattering and Wide-Angle X-ray Scattering) investigations at the ESRF. These advanced techniques will allow us to characterize HA c-axis and its mineral crystalline structure in the three different subtypes of OS. Consequently, we will also be able to evaluate the impact of chemotherapy on osteosarcoma bone tissue.

While synchrotron-sourced techniques are not currently applicable in vivo due to the associated high radiation dose, the data they yield can provide invaluable insights for clinicians and scientists seeking to comprehend the growth and progression of osteosarcoma. This comprehensive multi-scale and hierarchical characterization of different subtypes of osteosarcoma tumor microenvironments holds significant potential for the development of more effective and precise therapies, ultimately aiming to cure osteosarcoma with reduced acute and long-term side effects.





# Chapter 4: Multiparametric evaluation of bone sarcomas

Bone sarcomas exhibit diverse imaging features which reflect the heterogeneous nature of these diseases. Osteosarcoma, the most common type, typically presents as aggressive bone-forming lesions. Chondrosarcoma, characterized by hyaline-like cartilaginous matrix, predominantly occurs in the proximal femur [163]. Undifferentiated pleomorphic sarcoma (UPS) manifests as a high-grade tumor with fibroblastic differentiation and it is commonly found in the metaphysis of long bones [164]. Each subtype has distinct histological features and anatomical locations which strongly influence tumor clinical presentations and treatment approaches.

NMR plays a pivotal role in evaluating bone and soft tissue sarcomas, providing imaging biomarkers indicative of tumor activity and disease status. While routine sequences delineate the anatomical features of tumoral and adjacent tissues, advanced NMR permits a multiparametric exploration of the biological aspects of sarcomas, both in the de-novo and post-treatment settings. Notably, diffusion-weighted MRI (DWI) and proton magnetic resonance spectroscopy ( $^1\text{H}$ -MRS) stand out as techniques of paramount interest [113]. DWI allows for correlation with tumor cellularity, facilitating the prediction of tumor malignancy and the characterization of tissue necrosis following neo-adjuvant chemotherapies. Meanwhile,  $^1\text{H}$ -MRS noninvasively reveals the tumor's metabolic profile, with the choline peak demonstrating a correlation with tissue malignancy [163]. From a clinical point of view, the presentation, prognosis, and therapeutic options may vary among

bone sarcomas. Therefore, in this study, we exploited UHF NMR at 7T to raise the knowledge on the imaging features of different bone sarcomas and pave the way for exploring the relationship between the tumor's pathological basis and its cellularity and metabolism.

## 4.1 Patients and Methods

### 4.1.1 Patients

Experiments were approved by the institutional ethics committee on clinical investigations (CRMBM, Marseille) and informed consent was obtained from all individual participants included in the study. Four patients with bone and soft tissue sarcoma underwent MRI examinations between March 2023 and November 2023. MRI acquisitions at 7T took place at CEMEREM (Centre d'Exploration Métabolique par Résonance Magnétique) in Marseille, France. Subjects' generalities are reported in Table 4.1.

ID	AGE	SEX	LOCATION	BONE SARCOMA
Subject 0	27	F	left knee joint	-
Subject 1	77	F	right proximal tibia	2nd grade chondrosarcoma
Subject 2	20	M	left distal femur	parosteal OS
Subject 3	69	M	right knee joint	3rd grade undifferentiated sarcoma
Subject 4	20	F	left distal femur	conventional OS

**Table 4.1** Generalities of the subjects involved in the bone sarcoma project.

### 4.1.2 Protocol

Participants were positioned feet first in a supine position within a 7-T system (MAGNETOM Step 2, Siemens Healthcare, Erlangen, Germany) equipped with a 70-

---

mT/m SC-72 gradient system. Acquisitions were carried out with a knee receiver coil positioned around the lesion area. Participants were instructed to keep a relaxed position during the measurements.

*Proton Density Imaging.* In-plane resolution:  $0.4 \times 0.4 \text{ mm}^2$  (matrix size =  $320 \times 320$ ), slice thickness: 0.4 mm (no slice gap),  $T_R/T_E = 1400/22$  ms, bandwidth: 679 Hz/pixel, CAIPIRINHA acceleration factor: 3 ( $T_{acq} = 5'40''$ ).

*Proton Density Fat-Saturated Imaging.* In-plane resolution:  $0.2 \times 0.2 \text{ mm}^2$  (matrix size =  $800 \times 800$ ), slice thickness: 2.0 mm (no slice gap),  $T_R/T_E = 6000/31$  ms, bandwidth: 434 Hz/pixel, GRAPPA acceleration factor: 2 ( $T_{acq} = 4'14''$ ).

*Diffusion-Weighted Imaging.* The constructor 2D multi-slice diffusion-weighted spin-echo echo-planar imaging (SE-EPI) sequence was used with the following parameters. In-plane resolution:  $1.0 \times 1.0 \text{ mm}^2$  (matrix size =  $120 \times 120$ ), slice thickness: 2.5 mm (no slice gap),  $T_R/T_E = 7700/68$  ms, bandwidth: 1446 Hz/pixel, single-shell 60 directions with  $b=750 \text{ s/mm}^2$  and a single  $b=0 \text{ s/mm}^2$  ( $b_0$ ) image, SPAIR fat saturation preparation, GRAPPA acceleration factor: 2 and partial Fourier: 6/8 ( $T_{acq} = 4'08''$ ). Four phase-encoding directions (left to right) were acquired. For compensation of  $B_0$ -related EPI distortions (see post-processing part below), an additional  $B_0$  field map was acquired with the same  $B_0$ -shim field of view and settings.

*$^1\text{H}$ -Magnetic Resonance Spectroscopy.* The constructor point-resolved spectroscopy (single-voxel) sequence was used with the following parameters.  $T_R/T_E = 2000/135$  ms, number of signals acquired = 128, voxel size varies according to the tumoral region ( $T_{acq} = 5'$ ).

### 4.1.3 Diffusion-Weighted Imaging (DWI)

*Processing.* Images were first converted to the NIfTI format using the dcm2niix package (available at: <https://github.com/rordenlab/dcm2niix>).

Diffusion-weighted and  $B_0$  images were first corrected for Gibbs-ringing artefacts [165] and denoised using the MP-PCA routine as implemented in the MRtrix3 package [166]. Eddy current distortions compensation of the diffusion-weighted images was performed using the “eddy” tool from the FMRIB Software Library (FSL, version 3.2.0, FMRIB Software Library, Oxford, UK). Remaining  $B_0$ -related EPI distortions were then corrected on all images from the  $B_0$  field map using the *fugue* functionality implemented in FSL. Finally, voxel-wise diffusion tensors were estimated for the mapping of the ADC.

*Quantitative data extraction.* The mean ADC values were measured for each lesion. A ROI with an average area between 100-200  $mm^2$  was manually placed on ADC maps in the solid and homogeneous part of the tumor avoiding necrotic, fibrotic, hemorrhagic and bone areas. Four mean ADC values were measured for each lesion and averaged.

### 4.1.4 $^1H$ -Magnetic Resonance Spectroscopy ( $^1H$ -MRS)

The single-voxel spectroscopy sequence was performed in multiple regions of interest inside the lesion by carefully placing the voxel to avoid cystic, necrotic and fatty regions. Normal muscle’s  $^1H$ -MRS is chosen as control reference due to the difficulty in obtaining spectra from normal skeleton because of the signal disturbance caused by fat and water. Automatic shim is chosen as golden standard but manual shim will be evaluated as adequate shimming is influenced by location and composition of the tumor.

*Data processing and extraction.* MRS data were processed using custom-written routines in Python integrating the AMARES Fortran code from jMRUI (<http://www.jmrui.eu/>). Centroids and FWHM of water, choline (Cho), creatine (Cr) and lipids peaks were obtained from  $^1H$ -MR spectra using the AMARES-MRUI-based time

domain fitting routine including appropriate previous knowledge for musculoskeletal metabolites [167].

## 4.2 Results

### 4.2.1 Subject 0

Subject 0 was taken as control reference to highlight the MRI features of the Proton Density (PD) and Proton Density Fat Saturation (PDFS) images in fat, bone, muscle, cartilage, bone marrow and musculoskeletal fluids. In PD-weighted images, the tissues with a higher concentration or density of protons generate the strongest signals and appear bright in the image. Fat appears bright, bone marrow has an intermediate to bright appearance, muscle is intermediate, and bone appears dark with respect to muscle (Fig. 4.1).

PDFS sequence is a specialized imaging sequence designed to improve contrast and visualization of non-fatty soft tissue structures. Fat appears intermediate to dark, bone marrow has an intermediate to dark appearance, muscle is intermediate to bright, and bone appears dark with respect to muscle (Fig. 4.2).

In the following, an  $^1\text{H}$ -MRS spectrum acquired from a voxel in the vastus medialis of a healthy female volunteer is reported. It exhibits the following metabolites: water, choline (Cho), creatine (Cr), intramyocellular (IMCL) and extramyocellular (EMCL) lipids (Fig. 4.3). The resonance frequencies (expressed in ppm) of the listed metabolites are reported in Table 4.2. Being a non-pathological muscular tissue, it shows low Cho and Cr peaks, and high lipids peak, whereas in case of malignant lesions Cho peak has been observed to be higher with respect to Cr [122].

METABOLITE	Frequency [ppm]
------------	-----------------

---

Water	4.69
Choline	3.21
Creatine	3.03
IMCL	1.5
EMCL	1.14

**Table 4.2** Normal muscle metabolites observed in Subject 0 quadriceps. For each metabolite, frequency, amplitude and FWHM of the resonance peaks were derived.

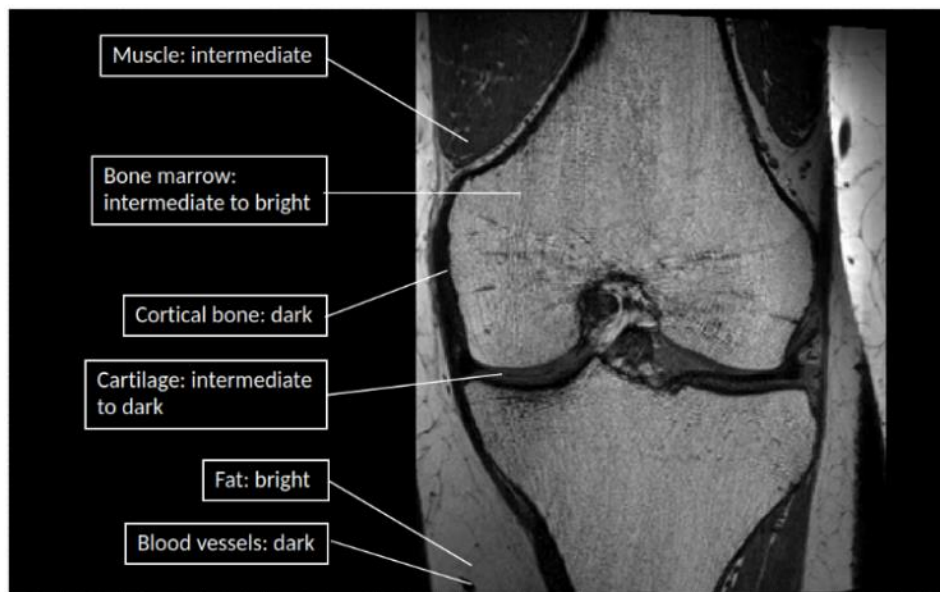


**Figure 4.1** Coronal PD image of the left knee from Subject 0. The main imaging features of muscle, bone marrow, bone, cartilage, fat and blood vessels are reported.

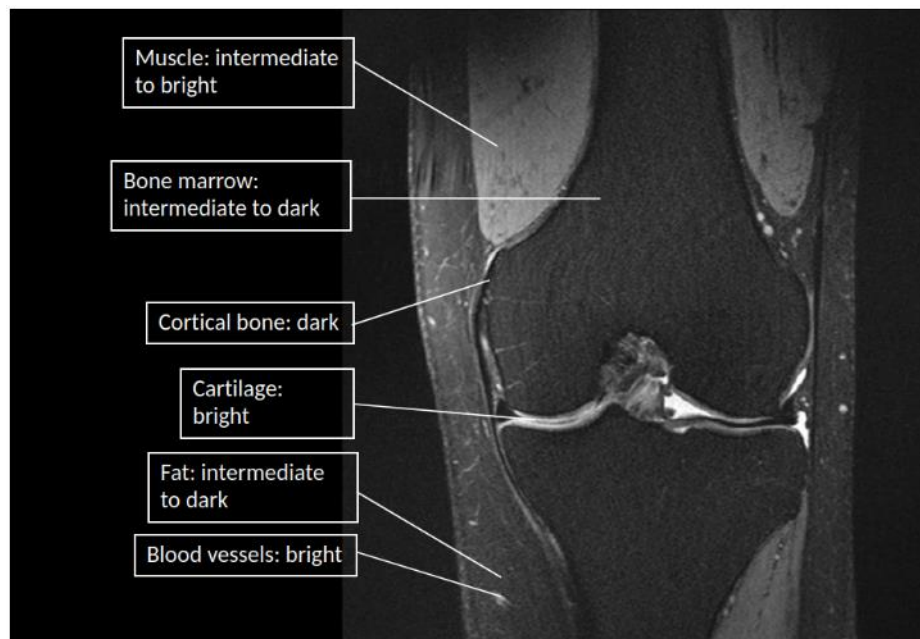


**Figure 4.2** Coronal PDFS image of the left knee from Subject 0. The main imaging features of muscle, bone marrow, bone, cartilage, fat and blood vessels are reported.

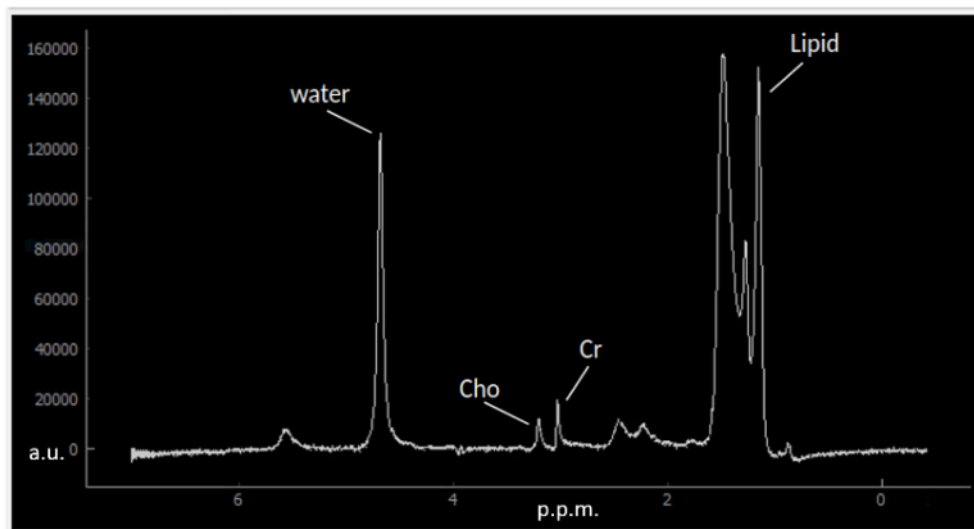


**Figure 4.3** H-MRS spectrum acquired through single-voxel spectroscopy from Subject 0 quadriceps muscle. The main metabolites detected are indicated.

### 4.2.2 Subject 1

Subject 1 was diagnosed with 2<sup>nd</sup> grade chondrosarcoma through histological analysis. Radiological examinations show a cortical based lesion with exophytic soft tissue component invading focally the bone medulla in the diaphysis of the left tibia. On PD images (Fig. 4.4 A and B), the lesion is isointense with respect to muscle. Low signal can be appreciated in the medullary canal, being indicative of bone marrow alteration. In the medullary cavity and in the exophytic mass, central ossified foci (asterisk in Fig. 4.4 A, B, C, D and F) of hypo intense signal are also noted. PDFS examination displays heterogeneous signal in the intramedullary infiltration (Fig. 4.4 C and D), hyper-intensities indicated by arrowheads in Fig. 4.4 D suggests the presence of muscular tissue inflammation and perilesional edema. The lesion presents diffusion restriction on DWI and ADC maps (Fig. 4.4 E and F). On ADC maps, the tumoral mass shows to be iso to hyper intense to muscular tissue with mean ADC values of the most restricted ROIs about  $2.08 \pm 0.17 \cdot 10^{-3} \frac{mm^2}{s}$ .



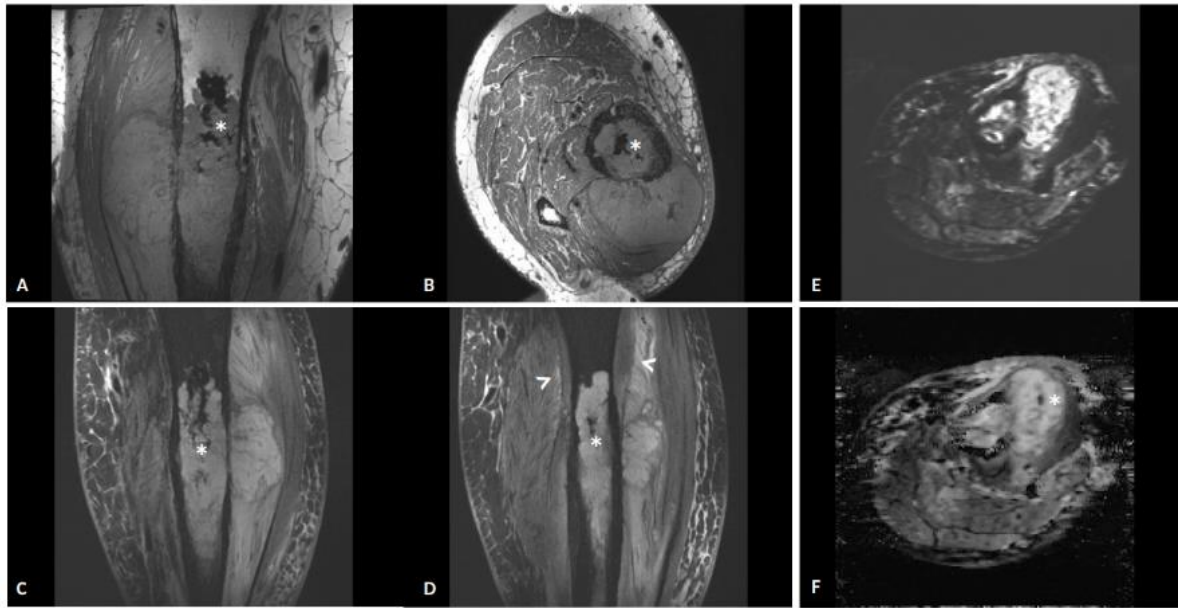


**Figure 4.4** Subject 1: 2<sup>nd</sup> grade chondrosarcoma. PD images (A and B), PDFS in C and D, DWI in E and ADC map in F. Asterisk highlights central ossified bone foci. Arrowheads indicate muscular inflammation.

### 4.2.3 Subject 2

Histological analysis assessed the presence of a parosteal OS. Radiological examinations show a tumoral mass surrounding the distal femur epiphysis area. Signs of a precedent surgical intervention can be appreciated in Fig. 9C (asterisk). Fig. 4.5 A and B provide a heterogeneous signal ipo to isointense to muscle in the tumor. Periosteum infiltration is well depicted in PDFS images (Fig. 4.5 C arrowhead) and heterogeneous signal in the tumoral mass can be appreciated as well (Fig. 4.5 D). The diffusion restriction of the sarcoma is seen on DWI, showing marked tumoral margins (Fig. 4.5 E). ADC map (Fig. 4.5 F) displays mean ADC value equal to  $1.95 \pm 0.47 \cdot 10^{-3} \frac{mm^2}{s}$ .

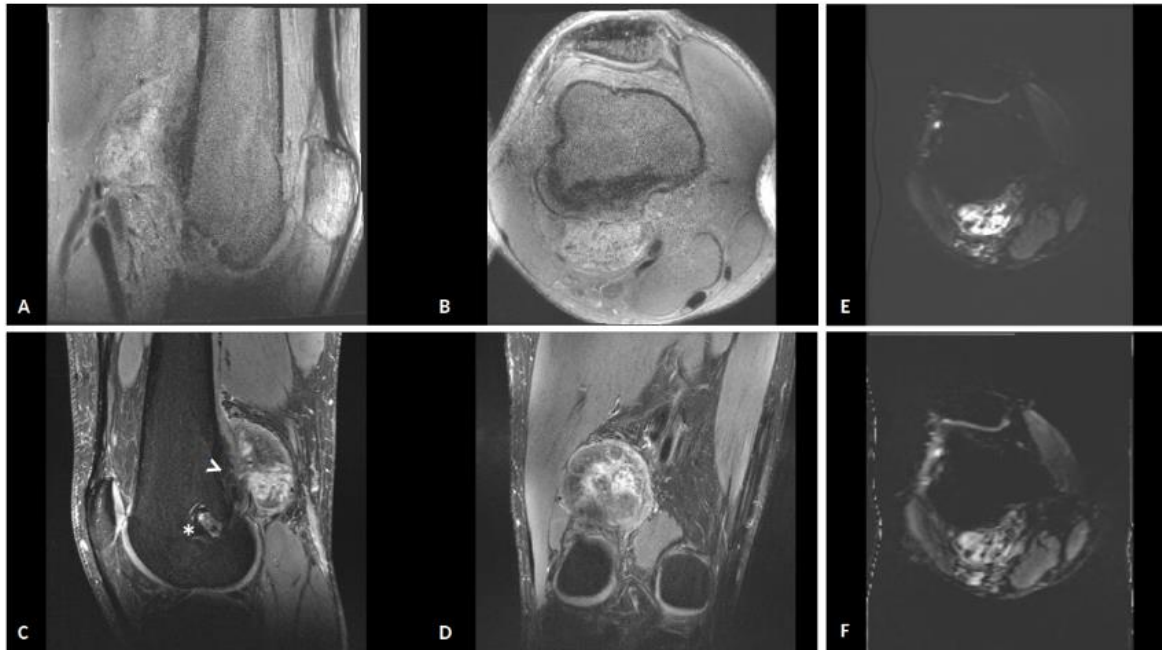


**Figure 4.5** Subject 2: parosteal OS. PD images (A and B), PDFS in C and D, DWI in E and ADC map in F. In C, asterisk highlights sign of previous surgical intervention in the area. Arrowheads indicate periosteum infiltration.

#### 4.2.4 Subject 3

Subject 3 was diagnosed with a 3<sup>rd</sup> grade undifferentiated sarcoma having pleomorphic and fusiform cells through histology. Radiological examinations highlight the presence of a large tumoral mass in the distal diaphyseal region of the right femur. On PD images (Fig. 4.6 A and B) the lesion shows an isointense signal with respect to muscle. Heterogeneous signal can be appreciated on coronal PDFS images denoting hemorrhage degradation products (Fig. 4.6 C). No DWI images could be derived because of subject motion and fat tissue artifacts that couldn't be removed during data processing.

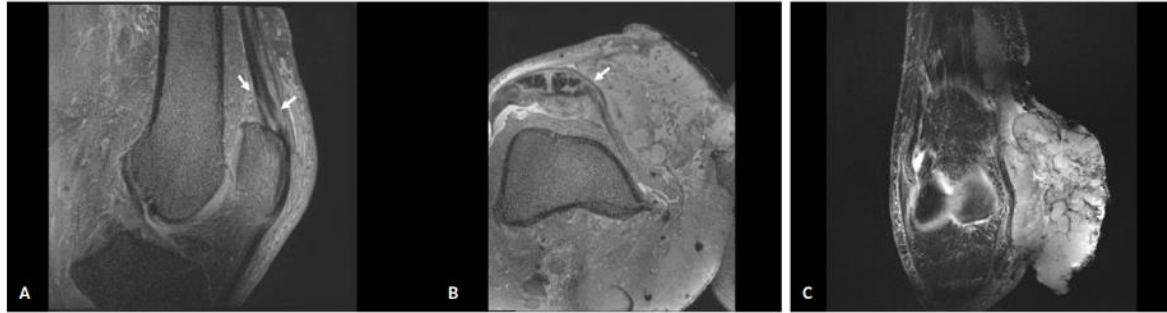


**Figure 4.6** Subject 3: 3<sup>rd</sup> grade undifferentiated sarcoma with pleomorphic and fusiform cells. Sagittal and coronal PD images (A and B), axial PDFS in C. Arrows in A) and B) indicate multilayered reaction.

#### 4.2.5 Subject 4

Histological examinations characterized the tumoral mass as a conventional OS. PD and PDFS acquisitions show a cortically based diaphyseal mass semi-circumferentially involving the anterolateral surface of the femur with thickening of the cortex (\* in Fig. 4.7 B and C). The lesion infiltrates the medullary cavity involving the entire diaphyseal region of the femur. It elicits heterogeneous signal in PDFS images and iso- to hyper-intense signal on PD acquisitions with respect to muscle (Fig. 4.7 A and C). The infiltrative intramedullary lesion can be easily distinguished in both PD and PDFS images being hypo-intense and hyper-intense to bone marrow respectively. The ADC map showed diffusion restriction in both the lesion and in the intramedullary infiltration (arrow in Fig. 4.7 D) with mean ADC values about  $2.09 \pm 0.39 \cdot 10^{-3} \frac{mm^2}{s}$ . <sup>1</sup>H-MRS was tested on multiple volumes of interest within the lesion, but the case was excluded because of an examination failure due to inaccurate manual shimming of the local magnetic field.

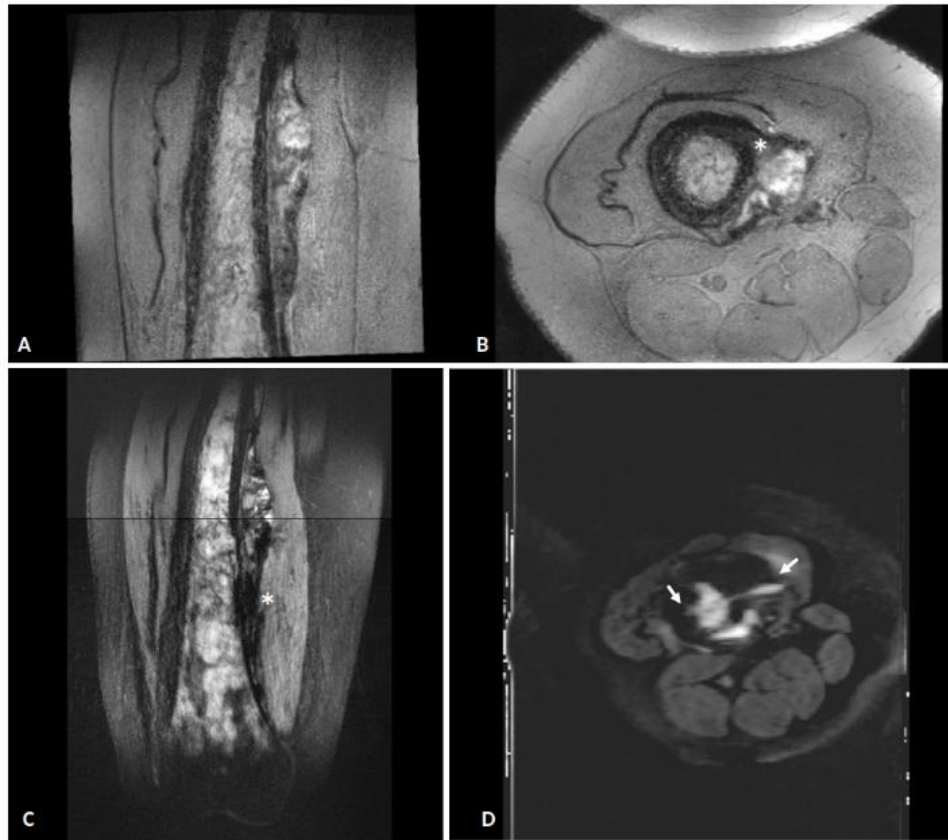


**Figure 4.7** Subject 4: conventional OS. Coronal and axial PD images (A and B), coronal PDFS in C and axial ADC map in D. Asterisk in B highlights cortex thickening. Arrows in D indicate intramedullary infiltration.

### 4.3 Discussion and Future Perspectives

Imaging plays an essential role in the diagnosis and staging of musculoskeletal sarcomas. A deep knowledge of the imaging criteria, as well as a quantification of tumor cellularity and metabolism, might give new insights in sarcoma diagnosis and therapeutic options. Special attention needs to be raised to the existence of less common MSK sarcoma subtypes that haven't been exhaustively characterized yet [163]. In this thesis, MRI was tested as a tool for the multiparametric evaluation of bone sarcoma. Conventional MR imaging sequences and advanced NMR techniques were preliminarily tested on a cohort

---

of four patients and a healthy volunteer. The studied lesions, mostly originating from long bones, included conventional sarcoma, parosteal sarcoma, undifferentiated sarcoma and chondrosarcoma. Conventional MRI allowed to depict morphological features of different OS subtypes. Intramedullary infiltration with signal alteration was appreciated in both chondrosarcoma and conventional OS. Specifically, chondrosarcoma exhibited ossified foci and perilesional edema around the lesion. In both parosteal OS and UPS, high signal was depicted in PDFS imaging.

The potential additional value of diffusion imaging is providing in vivo functional information, which, when added to conventional MR criteria, improves the specificity of lesions characterization [163]. All lesions showed restricted diffusion and, in the case of Subject 1 and 3, tumoral infiltration in the medullary cavity of bone was appreciated (Fig. 4.4 and 4.6). DWI allowed for univocal delineation of tumoral boundaries, thanks to the high resolution provided by UHF MRI at 7T [114]. The  $ADC_{mean}$  values were derived to represent mean tissue composition and ranged between  $1.95 \pm 0.43 \cdot 10^{-3} \frac{mm^2}{s}$  and  $2.09 \pm 0.39 \cdot 10^{-3} \frac{mm^2}{s}$ . It is well known that ADC values strongly depend on the MR system, the magnetic field strength and sequence parameters, and usually cannot be translated and compared consistently to other scanners' results. In future, the study will be extended to more patients to determine characteristic ADC values for different pathologic types of sarcomas. The potentiality of DWI will be also applied to the evaluation of early treatment response within the same subject, as the technique can distinguish viable and necrotic tumor areas and then noninvasively detect curative effect of chemotherapy in malignant tissues [168].

MRS holds significant promise in characterizing bone sarcomas by providing detailed biochemical information [122]. This study investigated the feasibility of applying  $^1H$ -MRS spectroscopy to bone sarcomas exploiting MRS non-invasiveness. The MRS sequence was

set up and an acquisition test was conducted on a healthy volunteer. The resulting MRS spectra exhibited typical features of muscular tissue spectra, including a low Cho peak, low Cr peak, and high lipid peaks. The acquisition protocol includes both water-suppressed and non-water-suppressed sequences, aiming to improve future quantification of Cho concentration following Fayad's approach [117]. Despite its great potential,  $^1\text{H}$ -MRS strongly depends on various factors that could lead to examination failure or inaccurate metabolites detection. Among them, shimming the local magnetic field is a critical step due to musculoskeletal tissues heterogeneity and it should be manually performed and customized based on the tumor type [101]. Furthermore, voxel selection strongly influences spectra quality, with excessive fat inclusion potentially obscuring metabolic peaks of interest, and water or cortical bone causing signal dropout. In future, the sequence will be applied to sarcoma patients and choline peak presence will be evaluated as a marker of lesions malignancy based on the fact that most malignant tumors have shown a very high Cho peak with respect to Cr [122]. The quantification of Cho concentration will also be tested and applied to investigate treatment response, post-surgical evaluation of tumoral margins, and non-invasive characterization of sarcoma subtypes. Clinically, the single-voxel spectroscopy sequence will be performed, after manual shim of the local magnetic field, in multiple regions of interest inside the lesion. Careful voxel placement will be ensured to avoid cystic, necrotic, and fatty regions. Normal muscle's  $^1\text{H}$ -MRS will be chosen as a control reference due to the difficulty in obtaining spectra from the normal skeleton caused by signal disturbance from fat and water.

To conclude, there are many kinds of bone and soft tissue tumors which differ in appearance and metabolic pattern, and at present, invasive biopsy is the gold standard to identify sarcomas subtypes and follow their pathological changes [122], [163]. In this research, conventional MRI was exploited to depict the imaging features of bone sarcoma and the potentiality of advanced MR techniques was investigated in the context of tumoral

---

lesions' multiparametric characterization at UHF. Among all advanced MR techniques, DWI and  $^1\text{H}$ -MRS were considered due to their versatility in depicting tumor cellularity and metabolism. DWI was applied to a cohort of three patients, showing well-distinguishable tumoral margins and allowing to individuate sites of medullary cavity invasion. Spectroscopy was tested on a muscle portion of a healthy volunteer, showing good separation between metabolites and low SNR thanks to the high field provided by the 7T clinical scanner used [169]. MR investigations will be extended in the future to the pre- and post- treatment evaluation of bone sarcoma, opening the way to non-invasive early characterization of tumoral morphology and cellularity.





## Chapter 5: Conclusions

This thesis tackled the challenge of bridging the gap between cellular and clinical aspects of osteosarcoma (OS), exploiting a multimodal and multiscale approach based on SR and NMR techniques. Specifically, the work focused on the study of biomineralization in OS, characterization of human tissue resected by OS and in vivo multiparametric evaluation of bone sarcomas.

The early stages of bone biomineralization were explored to depict the defective differentiation process occurring in OS cells. In particular, osteoblast-like SaOS-2 cells were induced to differentiate towards osteoblasts and analysed under cryogenic conditions at 4 and 10 days after induction. The formation of bone mineral matrix was monitored using synchrotron-based techniques. Nano-XANES microscopy combined with cryo-SXT allowed to characterize the chemical composition of intracellular minerals and the 3D distribution of deposits and organelles. In addition, nano-XRFM provided information on the elemental distribution of Ca, P and Zn at both intra and extracellular level. Interestingly, HA was identified as the final product of tumoral cells differentiation towards osteoblasts. In particular, in this work we suggest that the process of Ca deposition formation starts with a calcium carbonate compound, which incorporates Zn and then nucleates calcium phosphate integrating phosphates to build the lattice structure of HA. Spectroscopic and tomographic techniques provided complementary information suggesting a mechanism for calcium transport within the cell based on the interaction between mitochondria and vesicles. In the early stages of osteogenic induction (4 days), calcium granules were

---

observed inside mitochondria and some of them were linked to vesicles containing calcium phosphate, suggesting mineral exchange. Later, along differentiation (10 days), no calcium granules could be appreciated in mitochondria, supporting the hypothesized transfer. Furthermore, the mitochondria changed morphology during the differentiation process, suggesting a reprogramming of OS cells. In fact, in the early stages of differentiation, mitochondria appeared non-fused and spherical, implying the presence of a glycolytic metabolism typical of proliferating stem cells. Vitamin D in the differentiating cocktail may act by reprogramming OS cells making them more similar to their osteoprogenitors. Thus, as cells differentiated, they became more committed switching to a mature osteoblasts metabolism characterized by fused and interconnected mitochondria. The cellular characterization of OS reinforces the theory that the pathology may originate from defective osteoblastic differentiation, supporting therapeutic approaches based on differentiating agents that might restore the physiological mineralization in tumor cells.

A multiscale analysis was performed on three different OS resected human tissues by exploiting X-ray synchrotron-based techniques. Among them, PhC micro-T allowed to depict bone specimen architecture and morphology at high resolution. Despite the increased definition provided by synchrotron X-rays, the volume investigated in the specimen has generally shown not to be representative of the entire sample volume. Consequently, depending on the investigated area, tumors exhibited a substantial variation of the morphological parameters, which explains the necessity to study multiple regions of the tissue. Micro-XANES at the Ca K-edge and XRD revealed that the mineralized tissue formed by various subtypes of OS can be distinguished from normal bone not only in morphology, but also in chemical structure and composition. Specifically, the micro-XANES spectra were compared through PCA analysis, and two distinct clusters were observed. One constituted by the spectra acquired from tumor tissue and the other containing the spectra from control samples and the bone tissue that underwent

---

chemotherapy. This interesting finding underlines the presence of a less crystallized mineral phase in tumor tissue, and suggests that presurgical neoadjuvant chemotherapy may have positive effects on pathologic bone. XRD investigations showed that tumor bone mineral apatite is less abundant and ordered than in control tissue, supporting the presence of a less mature mineral component in tumoral samples. This comprehensive characterization of OS tumor environment provides novel insights for clinicians and scientists seeking to understand tumor development and progression.

In the context of a complex pathology like bone sarcoma, NMR plays an essential role in diagnosis, staging and treatment response evaluation in tumoral areas. Conventional and advanced NMR techniques were setup and tested to perform a multiparametric evaluation of bone sarcoma in vivo. Tests were conducted on a cohort of four subjects exploiting PD and PDFS magnetic resonance imaging, DWI and MRS. PD and PDFS allowed to depict tumor intramedullary infiltrations, asses the presence of ossified foci as well as perilesional edema. DWI precisely delineated tumoral boundaries providing a quantitative evaluation of tissue cellularity. In addition, MRS was tested on a healthy volunteer and showed good separation between all metabolites (Cho, Cr, Lip and water). Examination failure occurred during MRS tests conducted on sarcoma patients underlying the necessity to perform a manual shimming of the local magnetic field. In the future, the established protocol will be extended to a larger cohort of patients. Specifically, DWI and MRS will be applied to the pre and post-treatment evaluation of tumoral cellularity and metabolism, opening the way to a non-invasive (if compared to biopsy) early characterization of tumoral tissue.

The multiscale characterization of OS provided in this work gives new insights into tumor genesis and growth, tumor environment and, potentially metabolism. Despite the interesting results obtained, further investigations can be performed to draw a

comprehensive picture of OS from different framings. Conventional laboratory techniques, such as oxygen consumption monitoring, gene expression and analysis of enzyme activity, can provide information to support the defective osteoblastic differentiation process hypothesized for the etiology of OS. Synchrotron-radiation techniques can provide invaluable insights not only on the mineral but also on the organic component of bone tissue. For example, collagen fibres could be characterized by synchrotron-radiation scattering techniques. As the OS lines become sharper and more defined, the way for the development of improved therapeutic strategies and more accurate diagnostic tools gets cleared and outlined.

# References

- [1] B. Zanghellini *et al.*, “High-resolution large-area imaging of nanoscale structure and mineralization of a sclerosing osteosarcoma in human bone,” *J. Struct. Biol.*, vol. 207, no. 1, pp. 56–66, Jul. 2019, doi: 10.1016/j.jsb.2019.04.012.
- [2] A. G. Abdelaziz *et al.*, “A Review of 3D Polymeric Scaffolds for Bone Tissue Engineering: Principles, Fabrication Techniques, Immunomodulatory Roles, and Challenges,” *Bioeng. 2023, Vol. 10, Page 204*, vol. 10, no. 2, p. 204, Feb. 2023, doi: 10.3390/BIOENGINEERING10020204.
- [3] J. Dvorakova *et al.*, “Human cells with osteogenic potential in bone tissue research,” *Biomed. Eng. Online*, vol. 22, no. 1, Dec. 2023, doi: 10.1186/S12938-023-01096-W.
- [4] S. Lees and K. Probst, “The locus of mineral crystallites in bone,” *Connect. Tissue Res.*, vol. 18, no. 1, pp. 41–54, 1988, doi: 10.3109/03008208809019071.
- [5] K. S. Probst and S. Lees, “Visualization of crystal-matrix structure. In situ demineralization of mineralized turkey leg tendon and bone,” *Calcif. Tissue Int.*, vol. 59, no. 6, pp. 474–479, 1996, doi: 10.1007/BF00369213/METRICS.
- [6] G. Zhu *et al.*, “Bone physiological microenvironment and healing mechanism: Basis for future bone-tissue engineering scaffolds,” *Bioact. Mater.*, vol. 6, no. 11, pp. 4110–4140, Nov. 2021, doi: 10.1016/J.BIOACTMAT.2021.03.043.
- [7] R. Florencio-Silva, G. R. D. S. Sasso, E. Sasso-Cerri, M. J. Simões, and P. S. Cerri, “Biology of Bone Tissue: Structure, Function, and Factors That Influence Bone Cells,” *Biomed Res. Int.*, vol. 2015, 2015, doi: 10.1155/2015/421746.
- [8] P. A. Downey and M. I. Siegel, “Bone biology and the clinical implications for osteoporosis,” *Phys. Ther.*, vol. 86, no. 1, pp. 77–91, 2006, doi: 10.1093/PTJ/86.1.77.
- [9] J. A. Buckwalter, M. J. Glimcher, R. R. Cooper, and R. Recker, “Bone biology. I: Structure, blood supply, cells, matrix, and mineralization.,” *Instr. Course Lect.*, vol. 45, pp. 371–386, 1996, Accessed: Jan. 28, 2024. [Online]. Available: <https://researchworks.creighton.edu/esploro/outputs/journalArticle/Bone-biology-I-Structure-blood-supply/991005930970202656>.
- [10] N. A. Sims and J. H. Gooi, “Bone remodeling: Multiple cellular interactions required for coupling of bone formation and resorption,” *Semin. Cell Dev. Biol.*, vol. 19, no.

- 5, pp. 444–451, Oct. 2008, doi: 10.1016/J.SEMCDB.2008.07.016.
- [11] K. Matsuo and N. Irie, “Osteoclast–osteoblast communication,” *Arch. Biochem. Biophys.*, vol. 473, no. 2, pp. 201–209, May 2008, doi: 10.1016/J.ABB.2008.03.027.
- [12] F. W. Wehrli, “Magnetic resonance of calcified tissues,” *J. Magn. Reson.*, vol. 229, pp. 35–48, Apr. 2013, doi: 10.1016/J.JMR.2012.12.011.
- [13] B. Wang, Z. Zhang, and H. Pan, “Bone Apatite Nanocrystal: Crystalline Structure, Chemical Composition, and Architecture,” *Biomimetics*, vol. 8, no. 1, p. 90, Mar. 2023, doi: 10.3390/BIOMIMETICS8010090/S1.
- [14] A. Ressler, A. Žužić, I. Ivanišević, N. Kamboj, and H. Ivanković, “Ionic substituted hydroxyapatite for bone regeneration applications: A review,” *Open Ceram.*, vol. 6, p. 100122, Jun. 2021, doi: 10.1016/J.OCERAM.2021.100122.
- [15] T. Theophanides and T. Theophanides, *Infrared Spectroscopy - Life and Biomedical Sciences*. InTechOpen, 2012.
- [16] E. S. Kovaleva, M. P. Shabanov, V. I. Putlayev, Y. Y. Filippov, Y. D. Tretyakov, and V. K. Ivanov, “Carbonated hydroxyapatite nanopowders for preparation of bioresorbable materials,” *Materwiss. Werksttech.*, vol. 39, no. 11, pp. 822–829, Nov. 2008, doi: 10.1002/MAWE.200800383.
- [17] C. Rey, B. Collins, T. Goehl, I. R. Dickson, and M. J. Glimcher, “The carbonate environment in bone mineral: A resolution-enhanced fourier transform infrared spectroscopy study,” *Calcif. Tissue Int.*, vol. 45, no. 3, pp. 157–164, May 1989, doi: 10.1007/BF02556059/METRICS.
- [18] R. Sathyavathi *et al.*, “Raman spectroscopic sensing of carbonate intercalation in breast microcalcifications at stereotactic biopsy OPEN,” *Sci. Rep.*, 2015, doi: 10.1038/srep09907.
- [19] M. M. Kerssens, P. Matousek, K. Rogers, and N. Stone, “Towards a safe non-invasive method for evaluating the carbonate substitution levels of hydroxyapatite (HAP) in micro-calcifications found in breast tissue,” *Analyst*, vol. 135, no. 12, pp. 3156–3161, Nov. 2010, doi: 10.1039/C0AN00565G.
- [20] B. Wang, Z. Zhang, and H. Pan, “Bone Apatite Nanocrystal: Crystalline Structure, Chemical Composition, and Architecture,” *Biomimetics*, vol. 8, no. 1, p. 90, Mar. 2023, doi: 10.3390/BIOMIMETICS8010090/S1.
- [21] C. Combes, S. Cazalbou, C. Rey, K. Benzerara, J. Miot, and T. Coradin, “Apatite Biominerals,” *Miner. 2016, Vol. 6, Page 34*, vol. 6, no. 2, p. 34, Apr. 2016, doi:

- 10.3390/MIN6020034.
- [22] D. Farlay, G. Panczer, C. Rey, P. D. Delmas, and G. Boivin, “Mineral maturity and crystallinity index are distinct characteristics of bone mineral,” *J. Bone Miner. Metab.*, vol. 28, no. 4, p. 433, 2010, doi: 10.1007/S00774-009-0146-7.
- [23] M. Bruderer, R. G. Richards, M. Alini, and M. J. Stoddart, “Role and regulation of RUNX2 in osteogenesis,” *Eur. Cell. Mater.*, vol. 28, pp. 269–286, Oct. 2014, doi: 10.22203/ECM.V028A19.
- [24] T. Komori, “Regulation of osteoblast differentiation by transcription factors,” *J. Cell. Biochem.*, vol. 99, no. 5, pp. 1233–1239, Dec. 2006, doi: 10.1002/JCB.20958.
- [25] Y. P. Chen, Y. L. Chu, Y. H. Tsuang, Y. Wu, C. Y. Kuo, and Y. J. Kuo, “Anti-Inflammatory Effects of Adenine Enhance Osteogenesis in the Osteoblast-Like MG-63 Cells,” *Life 2020, Vol. 10, Page 116*, vol. 10, no. 7, p. 116, Jul. 2020, doi: 10.3390/LIFE10070116.
- [26] S. Vimalraj, “Alkaline phosphatase: Structure, expression and its function in bone mineralization,” *Gene*, vol. 754, p. 144855, Sep. 2020, doi: 10.1016/J.GENE.2020.144855.
- [27] I. Mortada and R. Mortada, “Dental pulp stem cells and osteogenesis: an update,” *Cytotechnology*, vol. 70, no. 5, pp. 1479–1486, Oct. 2018, doi: 10.1007/S10616-018-0225-5/METRICS.
- [28] B. Xia, J. Wang, L. Guo, and Z. Jiang, “Effect of bone sialoprotein on proliferation and osteodifferentiation of human bone marrow-derived mesenchymal stem cells in vitro,” *Biologicals*, vol. 39, no. 4, pp. 217–223, Jul. 2011, doi: 10.1016/J.BIOLOGICALS.2011.04.004.
- [29] M. Mazzali, T. Kipari, V. Ophascharoensuk, J. A. Wesson, R. Johnson, and J. Hughes, “Osteopontin—a molecule for all seasons,” *QJM An Int. J. Med.*, vol. 95, no. 1, pp. 3–13, Jan. 2002, doi: 10.1093/QJMED/95.1.3.
- [30] T. C. Brennan-Speranza and A. D. Conigrave, “Osteocalcin: an osteoblast-derived polypeptide hormone that modulates whole body energy metabolism,” *Calcif. Tissue Int.*, vol. 96, no. 1, pp. 1–10, Jan. 2015, doi: 10.1007/S00223-014-9931-Y/FIGURES/2.
- [31] J. P. Gorski, “Biom mineralization of bone: A fresh view of the roles of non-collagenous proteins,” *Front. Biosci.*, vol. 16, no. 7, pp. 2598–2621, Jun. 2011, doi: 10.2741/3875/PDF.

- 
- [32] F. S. Sayegh, G. C. Solomon, and R. W. Davis, "Ultrastructure of intracellular mineralization in the deer's antler," *Clin. Orthop. Relat. Res.*, vol. No. 99, no. 99, pp. 267–284, 1974, doi: 10.1097/00003086-197403000-00030.
- [33] S. Omelon, M. Ariganello, E. Bonucci, M. Grynepas, and A. Nanci, "A Review of Phosphate Mineral Nucleation in Biology and Geobiology," *Calcif. Tissue Int.* 2013 934, vol. 93, no. 4, pp. 382–396, Sep. 2013, doi: 10.1007/S00223-013-9784-9.
- [34] X. Zhou, Y. Cui, X. Zhou, and J. Han, "Phosphate/Pyrophosphate and MV-related Proteins in Mineralisation: Discoveries from Mouse Models," *Int. J. Biol. Sci.*, vol. 8, no. 6, pp. 778–790, Jun. 2012, doi: 10.7150/IJBS.4538.
- [35] S. R. Stock, "The Mineral–Collagen Interface in Bone," *Calcif. Tissue Int.*, vol. 97, no. 3, pp. 262–280, Sep. 2015, doi: 10.1007/S00223-015-9984-6/FIGURES/6.
- [36] S. Boonrungsiman *et al.*, "The role of intracellular calcium phosphate in osteoblast-mediated bone apatite formation," *Proc. Natl. Acad. Sci. U. S. A.*, vol. 109, no. 35, pp. 14170–14175, Aug. 2012, doi: 10.1073/PNAS.1208916109/SUPPL\_FILE/SM01.MOV.
- [37] J. Mahamid, A. Sharir, D. Gur, E. Zelzer, L. Addadi, and S. Weiner, "Bone mineralization proceeds through intracellular calcium phosphate loaded vesicles: A cryo-electron microscopy study," *J. Struct. Biol.*, vol. 174, no. 3, pp. 527–535, Jun. 2011, doi: 10.1016/J.JSB.2011.03.014.
- [38] C. Tang *et al.*, "Biomaterial Precursor Formation Is Initiated by Transporting Calcium and Phosphorus Clusters from the Endoplasmic Reticulum to Mitochondria," *Adv. Sci. (Weinheim, Baden-Wuerttemberg, Ger.)*, vol. 7, no. 8, Apr. 2020, doi: 10.1002/ADVS.201902536.
- [39] H. K. Brown, K. Schiavone, F. Gouin, M. F. Heymann, and D. Heymann, "Biology of Bone Sarcomas and New Therapeutic Developments," *Calcif. Tissue Int.*, vol. 102, no. 2, pp. 174–195, 2018, doi: 10.1007/s00223-017-0372-2.
- [40] F. Rossi *et al.*, "Shedding Light on Osteosarcoma Cell Differentiation: Impact on Biomaterialization and Mitochondria Morphology," *Int. J. Mol. Sci.*, vol. 24, no. 10, May 2023, doi: 10.3390/IJMS24108559.
- [41] A. Biazzo and M. De Paolis, "Multidisciplinary approach to osteosarcoma.," *Acta Orthop. Belg.*, 2016.
- [42] G. Yarmish, M. J. Klein, J. Landa, R. A. Lefkowitz, and S. Hwang, "Imaging Characteristics of Primary Osteosarcoma: Nonconventional Subtypes1," <https://doi.org/10.1148/rg.306105524>, vol. 30, no. 6, pp. 1653–1672, Oct. 2010, doi:



- 10.1148/RG.306105524.
- [43] J. Lamplot *et al.*, “The Current and Future Therapies for Human Osteosarcoma,” *Curr. Cancer Ther. Rev.*, vol. 9, no. 1, pp. 55–77, 2013, doi: 10.2174/1573394711309010006.
- [44] E. R. Wagner *et al.*, “Therapeutic implications of PPAR $\gamma$  in human osteosarcoma,” *PPAR Res.*, vol. 2010, no. Figure 2, pp. 11–13, 2010, doi: 10.1155/2010/956427.
- [45] M. S. Isakoff, S. S. Bielack, P. Meltzer, and R. Gorlick, “Osteosarcoma: Current treatment and a collaborative pathway to success,” *J. Clin. Oncol.*, vol. 33, no. 27, pp. 3029–3035, 2015, doi: 10.1200/JCO.2014.59.4895.
- [46] J. Wang *et al.*, “The Role of miRNA in the Diagnosis, Prognosis, and Treatment of Osteosarcoma,” <https://home.liebertpub.com/cbr>, vol. 34, no. 10, pp. 605–613, Dec. 2019, doi: 10.1089/GBR.2019.2939.
- [47] H. C. Beird *et al.*, “Osteosarcoma,” *Nat. Rev. Dis. Prim.* 2022 81, vol. 8, no. 1, pp. 1–19, Dec. 2022, doi: 10.1038/s41572-022-00409-y.
- [48] Y. Chen *et al.*, “Advances in differentiation therapy for osteosarcoma,” *Drug Discov. Today*, vol. 25, no. 3, pp. 497–504, 2020, doi: 10.1016/j.drudis.2019.08.010.
- [49] U. Jawad *et al.*, “Clinical Medicine Chondrosarcoma: A Clinical Review,” *J. Clin. Med.* 2023, vol. 12, p. 2506, 2023, doi: 10.3390/jcm12072506.
- [50] R. K. Kalil, “Undifferentiated Pleomorphic Sarcoma of Bone,” *Tumors Tumor-Like Lesions Bone*, pp. 473–480, 2020, doi: 10.1007/978-3-030-28315-5\_34.
- [51] N. Marina, M. Gebhardt, L. Teot, and R. Gorlick, “Biology and therapeutic advances for pediatric osteosarcoma,” *Oncologist*, vol. 9, no. 4, pp. 422–441, Jul. 2004, doi: 10.1634/THEONCOLOGIST.9-4-422.
- [52] A. Strzelecka-Kiliszek, L. Bozycki, S. Mebarek, R. Buchet, and S. Pikula, “Characteristics of minerals in vesicles produced by human osteoblasts hFOB 1.19 and osteosarcoma Saos-2 cells stimulated for mineralization,” *J. Inorg. Biochem.*, vol. 171, pp. 100–107, Jun. 2017, doi: 10.1016/J.JINORGBIO.2017.03.006.
- [53] E. M. Czekanska, M. J. Stoddart, R. G. Richards, and J. S. Hayes, “In search of an osteoblast cell model for in vitro research,” *Eur. Cell. Mater.*, vol. 24, pp. 1–17, 2012, doi: 10.22203/ECM.V024A01.
- [54] J. Fogh, W. C. Wright, and J. D. Loveless, “Absence of HeLa Cell Contamination in 169 Cell Lines Derived From Human Tumors,” *JNCI J. Natl. Cancer Inst.*, vol.

- 58, no. 2, pp. 209–214, Feb. 1977, doi: 10.1093/JNCI/58.2.209.
- [55] E. Murray, D. Provvedini, D. Curran, B. Catherwood, H. Sussman, and S. Manolagas, “Characterization of a human osteoblastic osteosarcoma cell line (SAOS-2) with high bone alkaline phosphatase activity,” *J. Bone Miner. Res.*, vol. 2, no. 3, pp. 231–238, 1987, doi: 10.1002/JBMR.5650020310.
- [56] L. G. Rao, M. K. Sutherland, G. S. Reddy, M. L. Siu-Caldera, M. R. Uskokovic, and T. M. Murray, “Effects of  $1\alpha,25$ -dihydroxy-16ene, 23yne-vitamin D3 on osteoblastic function in human osteosarcoma SaOS-2 cells: differentiation-stage dependence and modulation by  $17\text{-}\beta$  estradiol,” *Bone*, vol. 19, no. 6, pp. 621–627, Dec. 1996, doi: 10.1016/S8756-3282(96)00281-5.
- [57] G. Bilbe, E. Roberts, M. Birch, and D. B. Evans, “PCR phenotyping of cytokines, growth factors and their receptors and bone matrix proteins in human osteoblast-like cell lines,” *Bone*, vol. 19, no. 5, pp. 437–445, Nov. 1996, doi: 10.1016/S8756-3282(96)00254-2.
- [58] W. E. G. Müller, H. C. Schröder, U. Schlossmacher, V. A. Grebenjuk, H. Ushijima, and X. Wang, “Induction of carbonic anhydrase in SaOS-2 cells, exposed to bicarbonate and consequences for calcium phosphate crystal formation,” *Biomaterials*, vol. 34, no. 34, pp. 8671–8680, Nov. 2013, doi: 10.1016/J.BIOMATERIALS.2013.07.096.
- [59] W. E. G. Müller *et al.*, “Nonenzymatic Transformation of Amorphous  $\text{CaCO}_3$  into Calcium Phosphate Mineral after Exposure to Sodium Phosphate in Vitro: Implications for in Vivo Hydroxyapatite Bone Formation,” *ChemBioChem*, vol. 16, no. 9, pp. 1323–1332, Jun. 2015, doi: 10.1002/CBIC.201500057.
- [60] C. T. Supuran, “Carbonic anhydrases: novel therapeutic applications for inhibitors and activators,” *Nat. Rev. Drug Discov. 2008 72*, vol. 7, no. 2, pp. 168–181, Feb. 2008, doi: 10.1038/nrd2467.
- [61] R. Ramanan *et al.*, “Bio-sequestration of carbon dioxide using carbonic anhydrase enzyme purified from *Citrobacter freundii*,” *World J. Microbiol. Biotechnol.*, vol. 25, no. 6, pp. 981–987, Jun. 2009, doi: 10.1007/S11274-009-9975-8.
- [62] X. Chang *et al.*, “Carbonic anhydrase I (CA1) is involved in the process of bone formation and is susceptible to ankylosing spondylitis,” *Arthritis Res. Ther.*, vol. 14, no. 4, pp. 1–14, Jul. 2012, doi: 10.1186/AR3929/TABLES/4.
- [63] A. Sorrentino *et al.*, “Calcite as a precursor of hydroxyapatite in the early biomineralization of differentiating human bone-marrow mesenchymal stem cells,”

- Int. J. Mol. Sci.*, vol. 22, no. 9, 2021, doi: 10.3390/ijms22094939.
- [64] W. E. G. Müller *et al.*, “Inorganic polymeric phosphate/polyphosphate as an inducer of alkaline phosphatase and a modulator of intracellular Ca<sup>2+</sup> level in osteoblasts (SaOS-2 cells) in vitro,” *Acta Biomater.*, vol. 7, no. 6, pp. 2661–2671, Jun. 2011, doi: 10.1016/J.ACTBIO.2011.03.007.
- [65] X. Wang, H. C. Schröder, and W. E. G. Müller, “Enzyme-based biosilica and biocalcite: biomaterials for the future in regenerative medicine,” *Trends Biotechnol.*, vol. 32, no. 9, pp. 441–447, Sep. 2014, doi: 10.1016/J.TIBTECH.2014.05.004.
- [66] P. Willmott, “An introduction to synchrotron radiation: Techniques and applications,” *An Introd. to Synchrotron Radiat. Tech. Appl.*, pp. 1–352, Jun. 2011, doi: 10.1002/9781119970958.
- [67] A. Iglesias-Juez, G. L. Chiarello, G. S. Patience, and M. O. Guerrero-Pérez, “Experimental methods in chemical engineering: X-ray absorption spectroscopy—XAS, XANES, EXAFS,” *Can. J. Chem. Eng.*, vol. 100, no. 1, pp. 3–22, Jan. 2022, doi: 10.1002/CJCE.24291.
- [68] M. Newville, “Fundamentals of XAFS,” *Rev. Mineral. Geochemistry*, vol. 78, pp. 33–74, 2014, doi: 10.2138/RMG.2014.78.2.
- [69] B. K. (Bipin K. Agarwal, “X-ray spectroscopy : an introduction,” p. 419, 1991.
- [70] V. V Lider, “X-ray fluorescence imaging,” *Physics-Uspekhi*, vol. 61, no. 10, pp. 980–999, Oct. 2018, doi: 10.3367/UFNE.2017.07.038174.
- [71] M. J. Pushie, N. J. Sylvain, H. Hou, M. J. Hackett, M. E. Kelly, and S. M. Webb, “X-ray fluorescence microscopy methods for biological tissues,” *Metallomics*, vol. 14, no. 6, p. 32, Jun. 2022, doi: 10.1093/MTOMCS/MFAC032.
- [72] I. M. Zougrou *et al.*, “Ca L<sub>2,3</sub>-edge XANES and Sr K-edge EXAFS study of hydroxyapatite and fossil bone apatite,” *Naturwissenschaften*, vol. 103, no. 7–8, 2016, doi: 10.1007/S00114-016-1383-Y.
- [73] L. Monico *et al.*, “Synchrotron radiation Ca K-edge 2D-XANES spectroscopy for studying the stratigraphic distribution of calcium-based consolidants applied in limestones,” *Sci. Reports 2020 101*, vol. 10, no. 1, pp. 1–14, Aug. 2020, doi: 10.1038/s41598-020-71105-8.
- [74] J. M. Xto, C. N. Borca, J. A. Van Bokhoven, and T. Huthwelker, “Aerosol-based synthesis of pure and stable amorphous calcium carbonate,” *Chem. Commun.*, vol.

- 55, no. 72, pp. 10725–10728, Sep. 2019, doi: 10.1039/C9CC03749G.
- [75] D. Eichert, M. Salomé, M. Banu, J. Susini, and C. Rey, “Preliminary characterization of calcium chemical environment in apatitic and non-apatitic calcium phosphates of biological interest by X-ray absorption spectroscopy,” *Spectrochim. Acta Part B At. Spectrosc.*, vol. 60, no. 6, pp. 850–858, Jul. 2005, doi: 10.1016/J.SAB.2005.05.012.
- [76] F. M. F. De Groot, J. C. Fuggle, B. T. Thole, and G. A. Sawatzky, “L<sub>2,3</sub> x-ray-absorption edges of d<sub>0</sub> compounds: K<sup>+</sup>, Ca<sup>2+</sup>, Sc<sup>3+</sup>, and Ti<sup>4+</sup> in Oh (octahedral) symmetry,” *Phys. Rev. B. Condens. Matter*, vol. 41, no. 2, pp. 928–937, 1990, doi: 10.1103/PHYSREVB.41.928.
- [77] J. Rajendran, S. Gialanella, and P. B. Aswath, “XANES analysis of dried and calcined bones,” *Mater. Sci. Eng. C*, vol. 33, no. 7, pp. 3968–3979, Oct. 2013, doi: 10.1016/J.MSEC.2013.05.038.
- [78] S. J. Naftel, T. K. Sham, Y. M. Yiu, and B. W. Yates, “Calcium L-edge XANES study of some calcium compounds,” *J. Synchrotron Rad.*, vol. 8, pp. 255–257, 2001.
- [79] Y. Yamamoto and K. Shinohara, “Application of X-ray microscopy in analysis of living hydrated cells,” *Anat. Rec.*, vol. 269, no. 5, pp. 217–223, Oct. 2002, doi: 10.1002/AR.10166.
- [80] C. Jacobsen, “Soft x-ray microscopy,” *Trends Cell Biol.*, vol. 9, no. 2, pp. 44–47, Feb. 1999, doi: 10.1016/S0962-8924(98)01424-X.
- [81] A. Sorrentino *et al.*, “MISTRAL: A transmission soft X-ray microscopy beamline for cryo nano-tomography of biological samples and magnetic domains imaging,” *J. Synchrotron Radiat.*, vol. 22, pp. 1112–1117, 2015, doi: 10.1107/S1600577515008632.
- [82] Y. Wang, C. Jacobsen, J. Maser, and A. Osanna, “Soft X-ray microscopy with a cryo scanning transmission X-ray microscope: II. Tomography,” *J. Microsc.*, vol. 197, no. 1, pp. 80–93, 2000, doi: 10.1046/J.1365-2818.2000.00629.X.
- [83] G. McDermott, M. A. Le Gros, C. G. Knoechel, M. Uchida, and C. A. Larabell, “Soft X-ray Tomography and Cryogenic Light Microscopy: The Cool Combination in Cellular Imaging,” *Trends Cell Biol.*, vol. 19, no. 11, p. 587, Nov. 2009, doi: 10.1016/J.TCB.2009.08.005.
- [84] A. Sorrentino *et al.*, “MISTRAL: a transmission soft X-ray microscopy beamline for cryo nano-tomography of biological samples and magnetic domains imaging,” vol. 22, pp. 1112–1117, 2015, doi: 10.1107/S1600577515008632.

- 
- [85] R. Y. Tsien, "Imagining imaging's future.," *Nat. Rev. Mol. Cell Biol.*, vol. Suppl, no. SUPPL., pp. SS16-21, Sep. 2003, Accessed: Jan. 29, 2024. [Online]. Available: <https://europepmc.org/article/med/14587522>.
- [86] P. KIRKPATRICK and A. V. BAEZ, "Formation of Optical Images by X-Rays," *JOSA*, Vol. 38, Issue 9, pp. 766-774, vol. 38, no. 9, pp. 766-774, Sep. 1948, doi: 10.1364/JOSA.38.000766.
- [87] A. Sorrentino *et al.*, "Soft X-ray Transmission Microscopy on Lithium-Rich Layered-Oxide Cathode Materials," *Appl. Sci.* 2021, Vol. 11, Page 2791, vol. 11, no. 6, p. 2791, Mar. 2021, doi: 10.3390/APP11062791.
- [88] L. Brombal, "X-ray Phase-Contrast Tomography: Underlying Physics and Developments for Breast Imaging," Mar. 2020, Accessed: Jan. 04, 2024. [Online]. Available: <https://arts.units.it/handle/11368/2960312>.
- [89] L. Quenot, S. Bohic, and E. Brun, "X-ray Phase Contrast Imaging from Synchrotron to Conventional Sources: A Review of the Existing Techniques for Biological Applications," *Appl. Sci.* 2022, Vol. 12, Page 9539, vol. 12, no. 19, p. 9539, Sep. 2022, doi: 10.3390/APP12199539.
- [90] D. M. Paganin, K. S. Morgan, and K. K. W. Siu, "The projection approximation and edge contrast for x-ray propagation-based phase contrast imaging of a cylindrical edge," *Opt. Express*, Vol. 18, Issue 10, pp. 9865-9878, vol. 18, no. 10, pp. 9865-9878, May 2010, doi: 10.1364/OE.18.009865.
- [91] D. Paganin, S. C. Mayo, T. E. Gureyev, P. R. Miller, and S. W. Wilkins, "Simultaneous phase and amplitude extraction from a single defocused image of a homogeneous object," *J. Microsc.*, vol. 206, no. 1, pp. 33-40, Apr. 2002, doi: 10.1046/J.1365-2818.2002.01010.X.
- [92] C. Zuo *et al.*, "Transport of intensity equation: a tutorial," *Opt. Lasers Eng.*, vol. 135, p. 106187, Dec. 2020, doi: 10.1016/J.OPTLASENG.2020.106187.
- [93] C. Dullin *et al.*, "Multiscale biomedical imaging at the SYRMEP beamline of Elettra - Closing the gap between preclinical research and patient applications," *Phys. Open*, vol. 6, p. 100050, Feb. 2021, doi: 10.1016/J.PHYSO.2020.100050.
- [94] E. S. Ameh, "A review of basic crystallography and x-ray diffraction applications," doi: 10.1007/s00170-019-04508-1.
- [95] V. K. Pecharsky and P. Y. Zavalij, "Fundamentals of powder diffraction and structural characterization of materials [electronic resource] / by Vitalij K.

- Pecharsky, Peter Y. Zavalij,” 2005, Accessed: Jan. 04, 2024. [Online]. Available: [https://books.google.com/books/about/Fundamentals\\_of\\_Powder\\_Diffraction\\_and\\_S.html?hl=it&id=PXdCAAAAQBAJ](https://books.google.com/books/about/Fundamentals_of_Powder_Diffraction_and_S.html?hl=it&id=PXdCAAAAQBAJ).
- [96] S. Mastrogiacomo, W. Dou, J. A. Jansen, and X. F. Walboomers, “Magnetic Resonance Imaging of Hard Tissues and Hard Tissue Engineered Bio-substitutes,” *Mol. Imaging Biol.* 2019 216, vol. 21, no. 6, pp. 1003–1019, Nov. 2019, doi: 10.1007/S11307-019-01345-2.
- [97] D. B. Plewes and W. Kucharczyk, “Physics of MRI: A primer,” *J. Magn. Reson. Imaging*, vol. 35, no. 5, pp. 1038–1054, May 2012, doi: 10.1002/JMRI.23642.
- [98] S. Currie, N. Hoggard, I. J. Craven, M. Hadjivassiliou, and I. D. Wilkinson, “Understanding MRI: basic MR physics for physicians,” *Postgrad. Med. J.*, vol. 89, no. 1050, pp. 209–223, Apr. 2013, doi: 10.1136/POSTGRADMEDJ-2012-131342.
- [99] J. Keeler, *Understanding NMR Spectroscopy, 2nd Edition on About The Author Permissions Table Of Contents New To This Edition Features Selected type: Hardcover Quantity: 1 \$174.95 Understanding NMR Spectroscopy, 2nd Edition*, no. May. 2011.
- [100] S. Mastrogiacomo, W. Dou, J. A. Jansen, and X. F. Walboomers, “Magnetic Resonance Imaging of Hard Tissues and Hard Tissue Engineered Bio-substitutes,” *Mol. imaging Biol.*, vol. 21, no. 6, pp. 1003–1019, Dec. 2019, doi: 10.1007/S11307-019-01345-2.
- [101] T. K. Subhawong *et al.*, “Proton MR Spectroscopy in Metabolic Assessment of Musculoskeletal Lesions,” <http://dx.doi.org/10.2214/AJR.11.6505>, vol. 198, no. 1, pp. 162–172, Nov. 2012, doi: 10.2214/AJR.11.6505.
- [102] L. M. Fayad *et al.*, “A feasibility study of quantitative molecular characterization of musculoskeletal lesions by proton MR spectroscopy at 3 T,” *AJR. Am. J. Roentgenol.*, vol. 195, no. 1, Jul. 2010, doi: 10.2214/AJR.09.3718.
- [103] R. G. Menon, G. Chang, and R. R. Regatte, “Musculoskeletal MRI applications at ultra-high (7T) field strength,” *Magn. Reson. Imaging Clin. N. Am.*, vol. 29, no. 1, p. 117, Feb. 2021, doi: 10.1016/J.MRIC.2020.09.008.
- [104] H. Alizai, G. Chang, and R. R. Regatte, “MRI of the Musculoskeletal System: Advanced Applications using High and Ultrahigh Field MRI,” *Semin. Musculoskelet. Radiol.*, vol. 19, no. 4, pp. 363–374, Sep. 2015, doi: 10.1055/S-0035-1563735/ID/JR00854-29/BIB.
- [105] O. Kraff and H. H. Quick, “7T: Physics, safety, and potential clinical applications,”

- 
- J. Magn. Reson. Imaging*, vol. 46, no. 6, pp. 1573–1589, Dec. 2017, doi: 10.1002/JMRI.25723.
- [106] V. Juras *et al.*, “The comparison of the performance of 3 T and 7 T T2 mapping for untreated low-grade cartilage lesions,” *Magn. Reson. Imaging*, vol. 55, pp. 86–92, Jan. 2019, doi: 10.1016/J.MRI.2018.09.021.
- [107] J. Igréc and M. H. Fuchsjäger, “Imaging of Bone Sarcomas and Soft-Tissue Sarcomas Bildgebung von Knochen-und Weichteilsarkomen,” *Fortschr Röntgenstr*, vol. 193, pp. 1171–1182, 2021, doi: 10.1055/a-1401-0215.
- [108] V. Zampa, G. Roselli, and G. Beltrami, “MRI of bone tumors: advances in diagnosis and treatment assessment,” *Imaging Med.*, vol. 2, no. 3, pp. 325–340, Jun. 2010, doi: 10.2217/IIM.10.28.
- [109] E. J. I. Clemente *et al.*, “Multiparametric MRI evaluation of bone sarcomas in children,” *Insights Imaging*, vol. 13, no. 1, Mar. 2022, doi: 10.1186/S13244-022-01177-9.
- [110] T. K. Subhawong, M. A. Jacobs, and L. M. Fayad, “Diffusion-weighted MR Imaging for Characterizing Musculoskeletal Lesions,” <https://doi.org/10.1148/rg.345140190>, vol. 34, no. 5, pp. 1163–1177, Sep. 2014, doi: 10.1148/RG.345140190.
- [111] T. Kubo, T. Furuta, M. P. Johan, M. Ochi, and N. Adachi, “Value of diffusion-weighted imaging for evaluating chemotherapy response in osteosarcoma: A meta-analysis,” *Mol. Clin. Oncol.*, vol. 7, no. 1, pp. 88–92, Jul. 2017, doi: 10.3892/MCO.2017.1273.
- [112] S. Ahlawat, J. Fritz, C. D. Morris, and L. M. Fayad, “Magnetic resonance imaging biomarkers in musculoskeletal soft tissue tumors: Review of conventional features and focus on nonmorphologic imaging,” *J. Magn. Reson. Imaging*, vol. 50, no. 1, pp. 11–27, Jul. 2019, doi: 10.1002/JMRI.26659.
- [113] T. K. Subhawong and B. A. Wilky, “Value added: functional MR imaging in management of bone and soft tissue sarcomas,” *Curr. Opin. Oncol.*, vol. 27, no. 4, pp. 323–331, Jul. 2015, doi: 10.1097/CCO.000000000000199.
- [114] J.-C. Mattei *et al.*, “Are We Heading to the Future of Musculoskeletal Tumor Imaging with Ultra-High Field 7T MRI?,” *Clin. Oncol. Res.*, pp. 1–8, Jan. 2019, doi: 10.31487/J.COR.2019.6.02.
- [115] J. Oudeman, A. J. Nederveen, G. J. Strijkers, M. Maas, P. R. Luijten, and M. Froeling, “Techniques and applications of skeletal muscle diffusion tensor imaging:

- A review,” *J. Magn. Reson. Imaging*, vol. 43, no. 4, pp. 773–788, Apr. 2016, doi: 10.1002/JMRI.25016.
- [116] Y. Hayashida *et al.*, “Monitoring therapeutic responses of primary bone tumors by diffusion-weighted image: Initial results,” *Eur. Radiol.*, vol. 16, no. 12, pp. 2637–2643, Dec. 2006, doi: 10.1007/S00330-006-0342-Y/FIGURES/5.
- [117] L. M. Fayad *et al.*, “Quantification of muscle choline concentrations by proton MR spectroscopy at 3 T: technical feasibility,” *AJR. Am. J. Roentgenol.*, vol. 194, no. 1, Jan. 2010, doi: 10.2214/AJR.09.3125.
- [118] M. Amar, R. G. Ghazi, L. G. Krishna, and G. Khanna, “Proton MR spectroscopy in characterization of focal bone lesions of peripheral skeleton,” *Egypt. J. Radiol. Nucl. Med.*, vol. 50, no. 1, pp. 1–12, Dec. 2019, doi: 10.1186/S43055-019-0109-5/TABLES/4.
- [119] L. M. Fayad, D. A. Bluemke, E. F. McCarthy, K. L. Weber, P. B. Barker, and M. A. Jacobs, “Musculoskeletal tumors: Use of proton MR spectroscopic imaging for characterization,” *J. Magn. Reson. Imaging*, vol. 23, no. 1, pp. 23–28, Jan. 2006, doi: 10.1002/JMRI.20448.
- [120] L. M. Fayad *et al.*, “Characterization of musculoskeletal lesions on 3-T proton MR spectroscopy,” *Am. J. Roentgenol.*, vol. 188, no. 6, pp. 1513–1520, Jun. 2007, doi: 10.2214/AJR.06.0935/ASSET/IMAGES/06\_0935\_04.JPEG.
- [121] T. J. Hsieh, C. W. Li, H. Y. Chuang, G. C. Liu, and C. K. Wang, “Longitudinally monitoring chemotherapy effect of malignant musculoskeletal tumors with in vivo proton magnetic resonance spectroscopy: An initial experience,” *J. Comput. Assist. Tomogr.*, vol. 32, no. 6, pp. 987–994, 2008, doi: 10.1097/RCT.0B013E31815B9CE9.
- [122] Z. H. Qi, C. F. Li, Z. F. Li, K. Zhang, Q. Wang, and D. X. Yu, “Preliminary study of 3T 1H MR spectroscopy in bone and soft tissue tumors,” *Chin. Med. J. (Engl.)*, vol. 122, no. 1, pp. 39–43, Jan. 2009, doi: 10.3760/CMA.J.ISSN.0366-6999.2009.01.008.
- [123] C. K. Wang, C. W. Li, T. J. Hsieh, S. H. Chien, G. C. Liu, and K. B. Tsai, “Characterization of Bone and Soft-Tissue Tumors with in Vivo 1H MR Spectroscopy: Initial Results1,” <https://doi.org/10.1148/radiol.2322031441>, vol. 232, no. 2, pp. 599–605, Aug. 2004, doi: 10.1148/RADIOL.2322031441.
- [124] H. Zhu and P. B. Barker, “MR Spectroscopy and Spectroscopic Imaging of the Brain,” *Methods Mol. Biol.*, vol. 711, pp. 203–226, 2011, doi: 10.1007/978-1-61737-992-5\_9/COVER.



- 
- [125] M. A. Jacobs, P. B. Barker, P. A. Bottomley, Z. Bhujwalla, and D. A. Bluemke, "Proton magnetic resonance spectroscopic imaging of human breast cancer: A preliminary study," *J. Magn. Reson. Imaging*, vol. 19, no. 1, pp. 68–75, Jan. 2004, doi: 10.1002/JMRI.10427.
- [126] F. Fischbach and H. Bruhn, "Assessment of in vivo  $^1\text{H}$  magnetic resonance spectroscopy in the liver: a review," *Liver Int.*, vol. 28, no. 3, pp. 297–307, Mar. 2008, doi: 10.1111/J.1478-3231.2007.01647.X.
- [127] M. A. Bredella, R. H. Ghomi, B. J. Thomas, K. K. Miller, and M. Torriani, "Comparison of 3.0 T proton magnetic resonance spectroscopy short and long echo-time measures of intramyocellular lipids in obese and normal-weight women," *J. Magn. Reson. Imaging*, vol. 32, no. 2, pp. 388–393, Aug. 2010, doi: 10.1002/JMRI.22226.
- [128] E. O. Aboagye and Z. M. Bhujwalla, "Malignant transformation alters membrane choline phospholipid metabolism of human mammary epithelial cells.," *Cancer Res.*, vol. 59, no. 1, pp. 80–84, Jan. 1999, Accessed: Jan. 29, 2024. [Online]. Available: <http://cancerres.aacrjournals.org/cgi/content/full/59/1/80>.
- [129] K. Glunde, C. Jie, and Z. M. Bhujwalla, "Molecular Causes of the Aberrant Choline Phospholipid Metabolism in Breast Cancer," *Cancer Res.*, vol. 64, no. 12, pp. 4270–4276, Jun. 2004, doi: 10.1158/0008-5472.CAN-03-3829.
- [130] P. E. Sijens, M. J. Van Den Bent, P. J. C. M. Nowak, P. Van Dijk, and M. Oudkerk, " $^1\text{H}$  chemical shift imaging reveals loss of brain tumor choline signal after administration of Gd-contrast," *Magn. Reson. Med.*, vol. 37, no. 2, pp. 222–225, Feb. 1997, doi: 10.1002/MRM.1910370214.
- [131] Y. Cui, H. Li, Y. Li, and L. Mao, "Novel insights into nanomaterials for immunomodulatory bone regeneration," *Nanoscale Adv.*, vol. 4, no. 2, pp. 334–352, Jan. 2022, doi: 10.1039/D1NA00741F.
- [132] J. E. Penner-Hahn, "X-ray Absorption Spectroscopy."
- [133] F. Bourdelle *et al.*, "Quantification of the ferric/ferrous iron ratio in silicates by scanning transmission X-ray microscopy at the Fe L<sub>2,3</sub> edges," *Contrib. to Mineral. Petrol.*, vol. 166, no. 2, pp. 423–434, 2013, doi: 10.1007/S00410-013-0883-4.
- [134] F. Marchegiani, E. Cibej, P. Vergni, G. Tosi, S. Fermani, and G. Falini, "Hydroxyapatite synthesis from biogenic calcite single crystals into phosphate solutions at ambient conditions," *J. Cryst. Growth*, vol. 311, no. 17, pp. 4219–4225,

- 2009, doi: 10.1016/j.jcrysgro.2009.07.010.
- [135] C. Messaoudi, T. Boudier, C. O. S. Sorzano, and S. Marco, “TomoJ: Tomography software for three-dimensional reconstruction in transmission electron microscopy,” *BMC Bioinformatics*, vol. 8, no. 1, pp. 1–9, Aug. 2007, doi: 10.1186/1471-2105-8-288/FIGURES/2.
- [136] G. Sciutto, P. Oliveri, S. Prati, M. Quaranta, S. Bersani, and R. Mazzeo, “An advanced multivariate approach for processing X-ray fluorescence spectral and hyperspectral data from non-invasive in situ analyses on painted surfaces,” *Anal. Chim. Acta*, vol. 752, pp. 30–38, Nov. 2012, doi: 10.1016/J.ACA.2012.09.035.
- [137] V. A. Solé, E. Papillon, M. Cotte, P. Walter, and J. Susini, “A multiplatform code for the analysis of energy-dispersive X-ray fluorescence spectra,” *Spectrochim. Acta Part B At. Spectrosc.*, vol. 62, no. 1, pp. 63–68, Jan. 2007, doi: 10.1016/J.SAB.2006.12.002.
- [138] J. Demšar *et al.*, “Orange: Data Mining Toolbox in Python,” *J. Mach. Learn. Res.*, vol. 14, no. 71, pp. 2349–2353, 2013, Accessed: Jan. 29, 2024. [Online]. Available: <http://jmlr.org/papers/v14/demsar13a.html>.
- [139] A. Procopio *et al.*, “Chemical Fingerprint of Zn-Hydroxyapatite in the Early Stages of Osteogenic Differentiation,” *ACS Cent. Sci.*, vol. 5, no. 8, pp. 1449–1460, Aug. 2019, doi: 10.1021/ACSCENTSCI.9B00509.
- [140] R. Lappalainen, M. Knuutila, S. Lammi, E. M. Alhava, and H. Olkkonen, “Zn and Cu Content in Human Cancellous Bone,” *Acta Orthop. Scand.*, vol. 53, no. 1, pp. 51–55, 1982, doi: 10.3109/17453678208992178.
- [141] X. Guo *et al.*, “Tracking the transformations of mesoporous microspheres of calcium silicate hydrate at the nanoscale upon ibuprofen release: a XANES and STXM study,” *CrystEngComm*, vol. 17, no. 22, pp. 4117–4124, May 2015, doi: 10.1039/C5CE00500K.
- [142] R. S. K. Lam, J. M. Charnock, A. Lennie, and F. C. Meldrum, “Synthesis-dependant structural variations in amorphous calcium carbonate,” *CrystEngComm*, vol. 9, no. 12, pp. 1226–1236, Nov. 2007, doi: 10.1039/B710895H.
- [143] G. N. Yan, Y. F. Lv, and Q. N. Guo, “Advances in osteosarcoma stem cell research and opportunities for novel therapeutic targets,” *Cancer Lett.*, vol. 370, no. 2, pp. 268–274, 2016, doi: 10.1016/j.canlet.2015.11.003.
- [144] H. H. Luu *et al.*, “Defective osteogenic differentiation in the development of osteosarcoma,” *Sarcoma*, vol. 2011, pp. 5–7, 2011, doi: 10.1155/2011/325238.

- 
- [145] B. J. Seo, S. H. Yoon, and J. T. Do, “Mitochondrial dynamics in stem cells and differentiation,” *Int. J. Mol. Sci.*, vol. 19, no. 12, 2018, doi: 10.3390/ijms19123893.
- [146] Q. Li, Z. Gao, Y. Chen, and M. X. Guan, “The role of mitochondria in osteogenic, adipogenic and chondrogenic differentiation of mesenchymal stem cells,” *Protein Cell*, vol. 8, no. 6, pp. 439–445, 2017, doi: 10.1007/s13238-017-0385-7.
- [147] M. F. Forni, J. Peggia, K. Trudeau, O. Shirihai, and A. J. Kowaltowski, “Murine mesenchymal stem cell commitment to differentiation is regulated by mitochondrial dynamics,” *Stem Cells*, vol. 34, no. 3, pp. 743–755, 2016, doi: 10.1002/stem.2248.
- [148] A. Fernández-Barral, P. Bustamante-Madrid, G. Ferrer-Mayorga, A. Barbáchano, M. J. Larriba, and A. Muñoz, “Vitamin D effects on cell differentiation and stemness in cancer,” *Cancers (Basel)*, vol. 12, no. 9, pp. 1–19, 2020, doi: 10.3390/cancers12092413.
- [149] S. Ma *et al.*, “Synchrotron Imaging Assessment of Bone Quality,” *Clin. Rev. Bone Miner. Metab.*, vol. 14, no. 3, p. 150, Sep. 2016, doi: 10.1007/S12018-016-9223-3.
- [150] A. Mittone *et al.*, “Multiscale pink-beam microCT imaging at the ESRF-ID17 biomedical beamline,” *urn:issn:1600-5775*, vol. 27, no. 5, pp. 1347–1357, Aug. 2020, doi: 10.1107/S160057752000911X.
- [151] F. Brun *et al.*, “SYRMEP Tomo Project: a graphical user interface for customizing CT reconstruction workflows,” *Adv. Struct. Chem. imaging*, vol. 3, no. 1, Dec. 2017, doi: 10.1186/S40679-016-0036-8.
- [152] A. K. Louis and A. K. Louis, “Diffusion reconstruction from very noisy tomographic data,” *Inverse Probl. Imaging*, vol. 4, no. 4, pp. 675–683, Nov. 2010, doi: 10.3934/IPI.2010.4.675.
- [153] J. Schindelin *et al.*, “Fiji: an open-source platform for biological-image analysis,” *Nat. Methods 2012 97*, vol. 9, no. 7, pp. 676–682, Jun. 2012, doi: 10.1038/nmeth.2019.
- [154] R. Domander, A. A. Felder, and M. Doube, “BoneJ2 - refactoring established research software,” *Wellcome Open Res.*, vol. 6, pp. 1–21, 2021, doi: 10.12688/WELLCOMEOPENRES.16619.2.
- [155] Y. Carter, C. D. L. Thomas, J. G. Clement, A. G. Peele, K. Hannah, and D. M. L. Cooper, “Variation in osteocyte lacunar morphology and density in the human femur — a synchrotron radiation micro-CT study,” *Bone*, vol. 52, no. 1, pp. 126–132, Jan. 2013, doi: 10.1016/J.BONE.2012.09.010.

- 
- [156] K. S. Mader, P. Schneider, R. Müller, and M. Stampanoni, “A quantitative framework for the 3D characterization of the osteocyte lacunar system,” *Bone*, vol. 57, no. 1, pp. 142–154, Nov. 2013, doi: 10.1016/J.BONE.2013.06.026.
- [157] A. P. Hammersley, “FIT2D: a multi-purpose data reduction, analysis and visualization program,” *urn:issn:1600-5767*, vol. 49, no. 2, pp. 646–652, Mar. 2016, doi: 10.1107/S1600576716000455.
- [158] T. Roisnel and J. Rodríguez-Carvajal, “WinPLOTR: A Windows Tool for Powder Diffraction Pattern Analysis,” *Mater. Sci. Forum*, vol. 378–381, no. I, pp. 118–123, 2001, doi: 10.4028/WWW.SCIENTIFIC.NET/MSF.378-381.118.
- [159] S. W. Donahue, N. A. Sharkey, K. A. Modanlou, L. N. Sequeira, and R. B. Martin, “Bone strain and microcracks at stress fracture sites in human metatarsals,” *Bone*, vol. 27, no. 6, pp. 827–833, Dec. 2000, doi: 10.1016/S8756-3282(00)00402-6.
- [160] Z. Seref-Ferlengez, O. D. Kennedy, and M. B. Schaffler, “Bone microdamage, remodeling and bone fragility: how much damage is too much damage?,” *Bonekey Rep.*, vol. 4, Mar. 2015, doi: 10.1038/BONEKEY.2015.11.
- [161] M. Toso, W. Singhatanadgit, S. Boonrungsiman, S. Youngjan, and P. Khemthong, “Investigating mineralization species in cultured bone from human mesenchymal stem cells using synchrotron-based XANES,” *Radiat. Phys. Chem.*, vol. 177, p. 109074, Dec. 2020, doi: 10.1016/J.RADPHYSHEM.2020.109074.
- [162] A. C. Langheinrich, C. Stolle, M. Kampschulte, D. Lommel, W. S. Rau, and B. Bassaly, “Diagnostic value of ex-vivo three-dimensional micro-computed tomography imaging of primary nonhematopoietic human bone tumors: osteosarcoma versus chondrosarcoma,” <http://dx.doi.org/10.1080/02841850802247673>, vol. 49, no. 8, pp. 940–948, Oct. 2008, doi: 10.1080/02841850802247673.
- [163] R. Zeitoun, A. M. Shokry, S. Ahmed Khaleel, and S. M. Mogahed, “Osteosarcoma subtypes: Magnetic resonance and quantitative diffusion weighted imaging criteria,” *J. Egypt. Natl. Canc. Inst.*, vol. 30, no. 1, pp. 39–44, Mar. 2018, doi: 10.1016/J.JNCL.2018.01.006.
- [164] I. Brčić and A. E. Rosenberg, “Pathology of pleomorphic/undifferentiated and dedifferentiated bone neoplasms,” *Semin. Diagn. Pathol.*, vol. 38, no. 6, pp. 163–169, Nov. 2021, doi: 10.1053/J.SEMDP.2021.04.005.
- [165] E. Kellner, B. Dhital, V. G. Kiselev, and M. Reisert, “Gibbs-ringing artifact removal based on local subvoxel-shifts,” *Magn. Reson. Med.*, vol. 76, no. 5, pp. 1574–1581,

- Nov. 2016, doi: 10.1002/MRM.26054.
- [166] J. D. Tournier *et al.*, “MRtrix3: A fast, flexible and open software framework for medical image processing and visualisation,” *Neuroimage*, vol. 202, p. 116137, Nov. 2019, doi: 10.1016/J.NEUROIMAGE.2019.116137.
- [167] C. P. Michel, D. Bendahan, B. Giannesini, C. Vilmen, Y. Le Fur, and L. A. Messonnier, “Effects of hydroxyurea on skeletal muscle energetics and force production in a sickle cell disease murine model,” *J. Appl. Physiol.*, vol. 134, no. 2, pp. 415–425, Feb. 2023, doi: 10.1152/JAPPLPHYSIOL.00333.2022/ASSET/IMAGES/LARGE/JAPPLPHYSIOL.00333.2022\_F003.JPEG.
- [168] T. A. Raafat, R. O. Kaddah, L. M. Bokhary, H. A. Sayed, and A. S. Awad, “The role of diffusion-weighted MRI in assessment of response to chemotherapy in osteosarcoma,” *Egypt. J. Radiol. Nucl. Med.*, vol. 52, no. 1, pp. 1–10, Dec. 2021, doi: 10.1186/S43055-020-00392-Y/TABLES/3.
- [169] R. R. Regatte and M. E. Schweitzer, “Ultra-high-field MRI of the musculoskeletal system at 7.0T,” *J. Magn. Reson. Imaging*, vol. 25, no. 2, pp. 262–269, 2007, doi: 10.1002/jmri.20814.



# Acknowledgements

I would like to express my deepest gratitude to my supervisors, Prof. Emil Malucelli and Prof. David Bendahan, their invaluable guidance, expertise, patience, and commitment have been fundamental in shaping this thesis. To Emil, for his support and encouragement, for valuing my opinion and making me face problems from a different point of view. To David, for helping me mature and grow independently, yet always being there when needed.

To Prof. Stefano Iotti who has enriched my academic experience and provided a stimulating environment for discussions.

I would like to express my heartfelt gratitude to Dott. Concettina Cappadone and Dott. Giovanna Farruggia. Your unwavering support and kindness have made working together not only productive but also extremely enjoyable.

To Dott. Jean-Camille Mattei, Dott. Lucas Soustelle, Lauriane Pini and Yann Le-Fur, I deeply thank you for your help and supervision in the “Sarcoma project”. Your guidance has been fundamental for the success of this preliminary study.

To Djamila, Yoko, Martine, Frank, Stanislas, Angèle, Danielle et Magatte. Thank you for welcoming me into the CRMBM/CEMEREM family.

During my PhD I've had the privilege to meet enthusiastic and passionate people, who showed me how incredible and challenging scientific research can be. To Andrea, Dmitry and Luisa, thank you for guiding and supporting me during these years. A special thanks to Michela, for her precious feedback, for her patience, and for holding my hand while leading me in the meanders of synchrotron techniques.

À ma famille marseillaise, for making me feel at home. À mes frères, Arthur and Luca, for your friendship, love, and most of all for your patience and tolerance in listening to my Italo-French accent. To Constance, Any, Alexis, Marc, Dmitrii, Max, Alicia, you will always have a special place in my heart, full of pasta and tiramisù. Constance, thank you for your support, care, love, and for pushing me (also literally) when I really needed it.

To my friends and colleagues from Bologna, to Martina, Martyna, Cristina, Lorenzo, Simone, Lucrezia and Giovanna, for creating a stimulating and homely environment in the lab. To Martina, my breakfast-tea fellow. Your passion and determination still inspire me, thank you. To Martyna, the best beamtime partner I could have ever asked for. Thank you for your support, trust, and for pretending to follow my late-night mathematical delusions.

To Paolo, Salvatore, Marco, Samuele, Elia, Mirco, Chiara, Gregorio and Giulia. Thank you for the happy memories, for always being there to encourage and share laughs during both the highs and lows of university life. Your friendship has been a source of strength and joy. Elia, thank you for your humor, for the daily train adventures, and for making me smile even when I was tired, stressed and demotivated.

To my dearest friends, Irene, Eugenia, Laura, Silvia and Debora. For cheering me on since forever. Despite the distance, the busy schedules, and adulthood approaching, I've always known I had (and will have) an incredible team ready to challenge and support me. Dear Debora, thank you for believing in my "artistic" skills.

I am deeply thankful to my family. To my mum and dad, for providing me with the fundamentals to develop my own opinions, thoughts, and passions. Thank you for trusting me and trying your best to put aside your doubts and apprehensions. To my brother, Paolo, who has always been an example to follow (I know that brother-sister etiquette really discourages this kind of admission, but just for once I'll make an exception).



To Nicola. For never interrupting your tutoring activity, I really hope I'll never have to pay you overtime.

